

ISTANBUL TECHNICAL UNIVERSITY ★ GRADUATE SCHOOL OF SCIENCE
ENGINEERING AND TECHNOLOGY

**PREDICTION OF MECHANICAL BEHAVIOR OF CARBON- BASED
NANO STRUCTURES**

Ph.D. THESIS

Cengiz BAYKASOĞLU

Department of Mechanical Engineering

Mechanical Engineering Programme

OCTOBER 2012

ISTANBUL TECHNICAL UNIVERSITY ★ GRADUATE SCHOOL OF SCIENCE
ENGINEERING AND TECHNOLOGY

**PREDICTION OF MECHANICAL BEHAVIOR OF CARBON- BASED
NANO STRUCTURES**

Ph.D. THESIS

Cengiz BAYKASOĞLU
(53062021)

Department of Mechanical Engineering

Mechanical Engineering Programme

Thesis Advisor: Prof. Dr. Ata MUĞAN

OCTOBER 2012

İSTANBUL TEKNİK ÜNİVERSİTESİ ★ FEN BİLİMLERİ ENSTİTÜSÜ

**KARBON ESASLI NANO YAPILARIN MEKANİK DAVRANIŞLARININ
BELİRLENMESİ**

DOKTORA TEZİ

**Cengiz BAYKASOĞLU
(503062021)**

Makine Mühendisliği Anabilim Dalı

Makine Mühendisliği Programı

Tez Danışmanı: Prof. Dr. Ata MUĞAN

EKİM 2012

Cengiz Baykasoglu, a **Ph.D.** student of **ITU Graduate School of Science Engineering And Technology** student ID **503062021**, successfully defended the thesis entitled “**PREDICTION OF MECHANICAL BEHAVIOR OF CARBON-BASED NANO STRUCTURES**” which he prepared after fulfilling the requirements specified in the associated legislations, before the jury whose signatures are below.

Thesis Advisor : **Prof. Dr. Ata MUĞAN**
Istanbul Technical University

Jury Members : **Prof. Dr. Cevat Erdem İMRAK**
Istanbul Technical University

Assist. Prof. Dr. Hakan ERSOY
Akdeniz University

Prof. Dr. Mehmet Alaeddin ARPACI
Istanbul Technical University

Prof. Dr. Uğur GÜVEN
Yildiz Technical University

Date of Submission : 01 August 2012
Date of Defense : 16 October 2012

To the memory of my father, İsmet Baykasoglu,

FOREWORD

This thesis is dedicated, in loving memory, to my father İsmet Baykasoğlu, who passed away while I was preparing this thesis. Thank you for giving me the opportunities to accomplish all that I have, and the drive to strive higher.

This thesis is also dedicated to my mother, Hüsnüye Baykasoğlu, who has always been there when I needed her and encouraged me to be independent and strong. Thank you for your guidance, encouragement, support and love over the years.

I wish to sincerely thank my supervisor Prof. Dr. Ata Muğan for your suggestions, encouragements and guidance in writing and approaching the different challenges during the thesis.

Thank you to both of my performance monitoring committee members, Prof. Dr. Cevat Erdem İmrak and Assist. Prof. Dr. Hakan Ersoy, for your guidance and direction.

I want to thank Dr. Emin Sünbuloğlu, Dr. Ergun Bozdağ, Prof. Dr. Adil Baykasoğlu, Prof. Dr. Halil Aykul, Assist. Prof. Dr. Oğuz ALTAY, Prof. Dr. Ali Kılıçarslan, Prof. Dr. Alaeddin Arpacı and Prof. Dr. Tuncer Toprak for their practical support, vision, and help.

Last but not the least, I would like to thank Yaşar Paça, Mesut Kirca, Fatih Aruk, Mesut Acar, Alper Tunga Çelebi and Esra İçer for their support and advice.

October 2012

Cengiz BAYKASOĞLU
(Mechanical Engineer)

TABLE OF CONTENTS

	<u>Page</u>
FOREWORD	ix
TABLE OF CONTENTS	xi
ABBREVIATIONS	xiii
LIST OF TABLES	xv
LIST OF FIGURES	xvii
SUMMARY	xxi
ÖZET	xxiii
1. INTRODUCTION	1
2. STRUCTURES OF CARBON-BASED NANOSTRUCTURES	11
3. FINITE ELEMENT (FE) MODELS OF CARBON-BASED NANOSTRUCTURES	17
3.1 FE Formulation	17
3.2 Solution Procedure for Small Deformation Static Problems	26
3.3 Application Of Atomistic Modelling Approach.....	27
4. CHARACTERIZATION, DYNAMIC AND FRACTURE ANALYSES OF GRAPHENE SHEETS (GSs)	37
4.1 Equivalent FE Models, Characterization And Vibration Analyses Of SLGSs	37
4.2 Dynamic Analyses Of SLGSs	44
4.3 Fracture Analyses Of SLGSs	51
4.3.1 FE formulation of the C-C bonds.....	51
4.3.2 FE models of defect-free and defected SLGSs	53
4.3.3 Computational results	56
5. COUPLED MOLECULAR/CONTINUUM MECHANICAL MODELING OF THE FRACTURE OF DEFECTED GSs	67
5.1 Computational Framework.....	67
5.1.1 Atomistic and continuum domain formulations.....	68
5.1.2 Coupling strategy	70
5.2 Numerical Examples	75
5.2.1 Static loading.....	76
5.2.2 Fracture analyses of defected SLGSs.....	80
6. VIBRATION AND ELASTIC BUCKLING ANALYSES OF CARBON NANOCONES (CNCs)	89
6.1 Structures Of SWCNCs.....	89
6.2 Vibrational And Elastic Buckling Analyses Of SWCNCs.....	90
7. CHARACTERIZATION AND FRACTURE ANALYSIS OF CARBON NANOTUBES (CNTs)	101
7.1 Axial Young's Modulus Of SWCNTs	101
7.2 Shear Modulus Of SWCNTs.....	103
7.3 Vibration Analysis Of SWCNTs.....	105

7.4 Elastic Buckling Analysis Of SWCNTs.....	112
7.5 Prediction Of Failure Behavior Of CNTs.....	115
7.5.1 Fracture model of SWCNTs.....	115
7.5.2 Computational results.....	117
8. CONCLUSION.....	125
REFERENCES	129
APPENDICES	139
APPENDIX A.1	140
APPENDIX A.2	141
CURRICULUM VITAE	143

ABBREVIATIONS

AFM	: Atomic Force Microscope
CNC	: Carbon nanocone
CNT	: Carbon Nanotube
CM	: Continuum Mechanics
DOF	: Degrees-of-freedom
EB	: Euler-Bernoulli
FE	: Finite Element
GS	: Graphene Sheet
MD	: Molecular Dynamics
MLGS	: Multi Layer Graphene Sheet
MM	: Molecular Mechanics
MWCNT	: Multi Wall Carbon Nanotube
SWCNC	: Single Wall Carbon Nanocone
SLGS	: Single Layer Graphene Sheet
STM	: Scanning Tunneling Microscope
SW	: Stone-Wales
SWCNT	: Single Wall Carbon Nanotube
QM	: Quantum Mechanic
QCM	: Quasi Continuum Mechanics
TEM	: Transmission Electron Micrographs

LIST OF TABLES

	<u>Page</u>
Table 2.1 : Types of CNTs based on chiral indices.	14
Table 3.1 : Geometric and material properties of the beam elements.....	31
Table 3.2 : Modified Morse potential parameters [72].	33
Table 3.3 : Tersoff- Brenner potential constants.....	36
Table 4.1 : Graphene data from literature and present work.....	39
Table 4.2 : Values of equivalent beam density ρ of Euler-Bernoulli beam elements.....	40
Table 4.3 : First six fundamental frequencies of 2-D SLGS (in GHz).....	40
Table 4.4 : First six fundamental frequencies of 3-D SLGS (in GHz).....	41
Table 4.5 : Properties of Well-known Members of the Newmark Family [130].....	45
Table 4.6 : Geometric properties of the EB beam element [29]	51
Table 4.7 : Predicted failure strain (ϵ_f) and stress (σ_f) values of SLGSs.....	60
Table 5.1 : Values of tensile rigidity Y , shear modulus G and thickness t of SLGSs.....	76
Table 5.2 : Maximum displacement errors in the second numerical example on static loading.	79
Table 5.3 : Results of the analysis of defected SLGSs.....	83
Table 6.1 : Properties of the beam elements... ..	92
Table 7.1 : The first six free-free natural frequency values of the SWCNTs (8, 8) with different heights (in GHz).	106
Table 7.2 : The first six free-clamped natural frequency values of SWCNTs (8, 8) with different heights (in GHz).....	107
Table 7.3 : The first six clamped-clamped natural frequency values of SWCNTs (8, 8) with different heights (in GHz).	107
Table 7.4 : The first six free-free natural frequency values of the lumped mass MM models with different heights (in GHz).. ..	108
Table 7.5 : The first six free-clamped natural frequency values of the lumped mass MM models with different heights (in GHz).. ..	108
Table 7.6 : The first six clamped-clamped natural frequency values of the lumped mass MM models with different heights (in GHz).. ..	109
Table 7.7 : The geometrics properties and total number of atoms of SWCNTs.	115
Table 7.8 : Predicted values of critical strain (ϵ_{cr}) and stress (σ_{cr}) for pristine SWCNTs. (M)TB, PM3 and DFT represent the (Modified) Tersoff- Brenner potential, semi-empirical quantum and density functional theory calculation, respectively.....	118
Table 7.9 : Relative critical strain (ϵ/ϵ_{cr}) and stress (σ/σ_{cr}) for defected SWCNTs where the defects are reconstructed (R) and symmetrically (sym) oriented. MTB is the modified Tersoff-Brenner potential and PM3 is semiempirical quantum calculations. The defect key indicates the number of vacant atoms.	121

Table 7.10 : Effect of geometric nonlinearity on fracture behavior of reconstructed one- atom vacancy defected SWCNTs.....	123
--	-----

LIST OF FIGURES

	<u>Page</u>
Figure 2.1 : Graphite, graphene, CNT and fullerene [115].....	11
Figure 2.2 : (a) Multi-layer carbon nanotube (MLCNTs) [1,116], (b) graphene membrane [117].....	12
Figure 2.3 : TEM images of carbon nanocones (a)-(d) shows cones with nominal apex angle $\alpha = 19.2^\circ, 38.9^\circ, 60^\circ$ and 83.6° , respectively [118].....	12
Figure 2.4 : Roll-up vector defining the structures of CNTs (a) GS and (b) SWCNTs [119].	13
Figure 2.5 : CNTs (a) armchair (6,6), (b) zig-zag (8,0), (c) chiral (8,5), (d) MLCNT (7,7) (10,10).....	14
Figure 2.6 : A map showing which (m,n) gives semiconducting and metallic tubes can be drawn. Only armchair CNTs (m=n) are strictly metallic [120]..	15
Figure 2.7 :The cone sheet with the dislocation angle of 240° corresponding to the cone with apex angle of 38.9° SWCNC.	16
Figure 3.1 : Molecular and equivalent FE models of the graphene layer.	17
Figure 3.2 : Molecular and equivalent FE models of the SWCNT.....	18
Figure 3.3 : Molecular and equivalent FE models of the SWCNC.	18
Figure 3.4 : Local and global DOF of the 2-D EB element [124]..	22
Figure 3.5 : Local DOF of the 3-D EB element [124].	24
Figure 3.6 : Potential energies in MMs [38]..	28
Figure 3.7 : Bond stretching energy in MMs.	29
Figure 3.8 : Angle bending energy in MMs.....	29
Figure 3.9 : Potential energies in structural mechanics [38].....	30
Figure 3.10 : Tensile energy-strain curve of the modified Morse potential... ..	34
Figure 3.11 : van der Waals force with the distance between two interacting atoms.	35
Figure 4.1 : (a) Molecular and (b) equivalent plane stress FE models on which boundary conditions are shown..	38
Figure 4.2 : The first three in-plane mode shapes of the lumped mass MM model (a)-(c), plane stress CM model (d)-(f) and consistent mass MM model (g)-(i) where the boundary conditions are free-fixed.....	42
Figure 4.3 : The first three 3-D mode shapes of the lumped mass MM model (a)-(c), shell CM model (d)-(f) and consistent mass MM model (g)-(i) where the boundary conditions are free-fixed.....	43
Figure 4.4 : Spectral radii for Newmark methods for varying β [130]....	45
Figure 4.5 : Boundary conditions and loadings of the MM models of the SLGSs in transient analyses (a) 2-D model loaded in y-direction, (b) 2-D model loaded in x-direction and (c) 3-D model loaded in z-direction... ..	47
Figure 4.6 : Variation of mid-span displacement in y-direction for 2-D MM model shown in figure 4.5 (a).....	48

Figure 4.7 : Variation of mid-span displacement in x-direction for 2-D MM model shown in figure 4.5 (b).....	48
Figure 4.8 : Power spectrum density plot of the 2-D MM model subjected to free-fixed boundary conditions.	49
Figure 4.9 : Variation of mid-span displacement in z-direction for 3-D MM model shown in figure 4.5 (c).	50
Figure 4.10 : Power spectrum density plot of the 3-D MM model.	50
Figure 4.11 : The Brenner and modified Morse potentials and tensile force fields, (a) potential field for Brenner and modified Morse potential (b) force fields in segment [AB] in part (a) [73].	53
Figure 4.12 : Equivalent FE model of the defect-free and defected SLGS model; (a) one atom vacancy, (b) SW defects	54
Figure 4.13 : SW defect generated by rotating the C–C bond (a) defect- free lattice and (b) SW- defected lattice..	55
Figure 4.14 : Force-displacement curve.	57
Figure 4.15 : Force-strain curve.....	57
Figure 4.16 : Stress- strain curve.....	58
Figure 4.17 : Secant moduli- strain curve.	58
Figure 4.18 : Stress- strain curves for defect-free armchair and zigzag type SLGSs with and without geometric nonlinearity effects... ..	61
Figure 4.19 : Stress- strain curves of armchair type SLGSs.	62
Figure 4.20 : Stress- strain curves of zigzag type SLGSs.	62
Figure 4.21 : (a) Fracture initiation and (b) propagation directions of the SW-defected armchair SLGS.....	63
Figure 4.22 : (a) Fracture initiation and (b) propagation directions of one atom vacancy defected zigzag SLGS.....	64
Figure 5.1 : Quadrilateral element and the coordinate systems. (a) Quadrilateral element in physical system, (b) square element in natural coordinate system [135].....	68
Figure 5.2 : Composition of Ω_A and Ω_C domains, (a) atomistic domain overlaps with several CM elements, (b) atomistic domain coincides with one CM element.....	71
Figure 5.3 : The displacement contours of the plane stress CM and MM models; (a) u_x component and (b) u_y component... ..	77
Figure 5.4 : Coupled CM/MM models where the MM models are identical while the CM model changes as follows: (a) model #1, (b) model #2 and (c) model #3.	78
Figure 5.5 : Displacement components u_y of the full atomistic and CM/MM coupled models at boundary nodes in the MM domain.	79
Figure 5.6 : Displacement components u_y of the full atomistic and CM/MM coupled models in mid horizontal nodes in the MM domain.	79
Figure 5.7 : Displacement components u_y of the full atomistic and CM/MM coupled models in mid vertical nodes in the MM domain.	80
Figure 5.8 : (a) The CM/MM coupled SLGS model, (b) one-atom vacancy defect, and (c) two-atoms vacancy defect.....	81
Figure 5.9 : Stress-strain curve of the C-C bond.....	81
Figure 5.10 : (a)Fracture initiation and (b) propagation directions of one atom vacancy defected fully atomistic and couple models.....	83
Figure 5.11 : The atomistic sheet containing a crack in the center..	84

Figure 5.12 : The deformed and undeformed configurations of atoms around the crack tip.....	85
Figure 5.13 : The strain results obtained by the elasticity solution and the CM/MM coupled model.	86
Figure 5.14 : The results of the MM/CM fracture strengths versus the Griffith's formula for a graphene sheet..	87
Figure 6.1 : Cone sheets with cone heights of 15 Å with a) disclination angles of 120°, b) disclination angles of 180°, c) disclination angles of 240°.....	90
Figure 6.2 : SWCNCs with cone heights of 15 Å with a) apex angle of 83.6°, b) apex angle of 60° c) apex angle of 38.9°.	90
Figure 6.3 : Free-clamped and clamped-clamped boundary conditions in vibrational analysis (upper) and axial compression and bending loading conditions in buckling analysis (below).	91
Figure 6.4 : Variation of the first natural frequency of SWCNCs having the disclination angles of 120°, 180° and 240° as the cone height changes for the free-clamped boundary condition.....	93
Figure 6.5 : Variation of the first natural frequency of SWCNCs having the disclination angles of 120°, 180° and 240° as the cone height changes for the free-clamped boundary condition.....	93
Figure 6.6 : Variation of the first natural frequency of SWCNCs having the disclination angles of 120°, 180° and 240° as the cone height changes for the clamped-clamped boundary condition	94
Figure 6.7 : First ten natural frequencies of SWCNCs having the height of 50 Å and disclination angles of 120°, 180° and 240° for free-free boundary condition.	95
Figure 6.8 : First ten natural frequencies of SWCNCs having the height of 50 Å and disclination angles of 120°, 180° and 240° for clamped-clamped boundary condition..	95
Figure 6.9 : Vibrational modes of SWCNC having the disclination angle of 120°, height of 30 Å for free-free boundary condition.	96
Figure 6.10 : Vibrational modes of SWCNC SWCNC having the disclination angle of 120°, height of 30 Å for free-clamped boundary condition.	96
Figure 6.11 : Variation of the first critical buckling load for the SWCNCs having the disclination angles of 120°, 180° and 240° as the cone height changes under axial compression loading condition..	97
Figure 6.12 : Variation of the first critical buckling load for the SWCNCs having the disclination angles of 120°, 180° and 240° as the cone height changes under bending loading condition.	98
Figure 6.13 : First ten buckling mode of SWCNCs having the disclination angles of 120°, 180° and 240°, and height of 50 Å for the axial loading	98
Figure 6.14 : First ten buckling mode of SWCNCs having the disclination angles of 120°, 180° and 240, and height of 50 Å for the bending loading...	99
Figure 6.15 : The first six buckling modes of the SWCNC having the disclination angle of 240° under the axial compression loading.	99
Figure 6.16 : The first six buckling modes of the SWCNC having the disclination angle of 240° under the bending loading.....	100
Figure 7.1 : SWCNTs (8,8) along with applied boundary conditions..	101
Figure 7.2 : Variation of Young's modulus of armchair and zigzag SWCNTs with tube diameter. The nominal thicknesses of both SWCNTs are 3.4Å..	102

Figure 7.3 : Variation of the Young's modulus of armchair and zigzag SWCNTs with tube diameter and nominal thickness.orce-strain curve.....	103
Figure 7.4 : SWCNTs (8,8) along with the applied boundary conditions.....	104
Figure 7.5 : Variation of shear modulus of armchair and zigzag SWCNTs with tube diameter and nominal thickness... ..	104
Figure 7.6 : Boundary conditions in vibrational analysis of SWCNTs a) Free-clamped and b) clamped-clamped.. ..	105
Figure 7.7 : Lumped mass MM model of the SWCNT... ..	108
Figure 7.8 : The first six free-free mode shapes of consistent MM model of SWCNTs (8, 8) with height of 60.3 Å.....	110
Figure 7.9 : The first six free-clamped mode shapes of consistent MM model of SWCNTs (8, 8) with height of 60.3 Å.....	110
Figure 7.10 : The first six clamped-clamped mode shapes of consistent MM model of SWCNTs (8, 8) with height of 60.3 Å... ..	111
Figure 7.11 : The numerical and analytical solutions of the fundamental mode frequencies of free-free, free-clamped and clamped- clamped SWCNTs (8,8) versus aspect ratio L/D.	112
Figure 7.12 : SWCNTs (8,8) along with the applied boundary conditions... ..	112
Figure 7.13 : The numerical and analytical solutions of the critical buckling loads of SWCNTs (8,8) versus aspect ratio L/D.....	113
Figure 7.14 : Critical buckling loads of SWCNTs as a function of nanotube diameter.. ..	114
Figure 7.15 : The first six buckling mode shapes of SWCNTs (8,8) with the height of 60.3 Å.	114
Figure 7.16 : Zigzag (10,0) nanotube models; (a) pristine, (b) non-reconstructed one-atom vacancy defect (c) non-reconstructed two-atom vacancy defect, (d) reconstructed one-atom vacancy defect (e) reconstructed two-atom vacancy defect.	116
Figure 7.17 : Stress-strain curves for pristine nanotube armchair (12,12) under uniaxial load.	119
Figure 7.18 : Stress-strain curves for pristine nanotube zigzag (20,0) under uniaxial load.... ..	120
Figure 7.19 : Stress-strain curves of pristine nanotubes (10,0) and (5,5) and one-atom vacancy defected nanotubes (10,0) and (5,5) under uniaxial load..... ..	122
Figure 7.20 : Stress-strain curves of one-atom vacancy defected nanotubes with non-linear geometric effect.... ..	123

PREDICTION OF MECHANICAL BEHAVIOR OF CARBON- BASED NANO STRUCTURES

SUMMARY

In this thesis, mechanical behavior of carbon-based nanostructures such as graphene sheets, carbon nanotubes and carbon nanocones are investigated by using a molecular mechanic based finite element and coupled molecular/continuum mechanic modeling approaches.

The proposed molecular mechanic based finite element approach links the molecular mechanics and structural mechanics, and is based on simulating the covalent bonds between carbon-carbon atoms with Euler-Bernoulli beam elements. The harmonic and modified Morse molecular mechanic potential functions are used for small and large deformation problems. Elastic, vibrational, buckling and nonlinear fracture behavior of carbon nanotubes, vibrational and elastic buckling characteristics of carbon nanocones and elastic, vibrational and nonlinear fracture behavior of graphene sheets are investigated by using molecular mechanic based finite element approach. In addition, an equivalent dynamic model is developed for carbon based nanostructures and transient behavior of graphene sheets are investigated by using proposed approach. It is shown that the proposed approach can reflect elastic, vibrational, buckling, transient and fracture characteristics of carbon based nanostructures.

In this thesis, a coupling method for molecular mechanic and continuum mechanic models is also derived based on an augmented formulation of atomistic and continuum displacement fields in a least square sense, which yields an optimization problem solved by using the Lagrange multiplier method. It allows coupled analyses of multiple numbers of molecular mechanic domains in a continuum mechanic domain. For the proposed approach, there is no need for a constraint on the meshes of the molecular mechanic and continuum mechanics domains and no overlapping domain is employed. Efficiency of the proposed approach is illustrated by solving fracture problems of graphene layers. Comparisons are made with the results given in literature. In sum, the proposed approach can compute the deformations of graphene layers in high accuracy, is very flexible to compute local solutions and can easily be applied to other materials.

KARBON ESASLI NANO YAPILARIN MEKANİK DAVRANIŞLARININ BELİRLENMESİ

ÖZET

Temel olarak kovalent bağ ile bağlı karbon atomlarının hegzagonal kafes yapısı içinde değişik formlarda sıkıca paketlenmesi ile oluşan grafen tabakalarının, karbon nanotüplerin ve nanokonilerin mükemmel mekanik, termal ve elektriksel özellikleri, onları nano elektro-mekanik, nano sensör ve nano kompozit sistem uygulamaları için potansiyel adaylar yapmıştır. Karbon esaslı bu malzemelerin mekanik özelliklerinin belirlenmesi, bu yapıların tasarımı ve kontrolü için oldukça önemli ve yararlıdır. Bu malzemelerin mekanik özelliklerinin belirlenmesi için deneysel ölçümler ve hesaplamalı yöntemler kullanılmaktadır. Deneysel olarak bu yapıların mekanik özelliklerinin elde edilmesi oldukça yüksek maliyetli ve zordur. Bundan dolayı, günümüzde hesaplamalı yöntemler karbon esaslı malzemelerin mekanik özelliklerinin tespitinde oldukça sık kullanılmaktadır. Kuantum mekanik, moleküler dinamik, moleküler mekanik yöntemleri, nano malzemelerin mekanik özelliklerinin tespiti için sıkça kullanılan hesaplamalı yöntemlerdir. Kuantum mekanik ve moleküler dinamik modelleme yöntemlerini kullanılarak oldukça doğru sonuçlar elde edilebilmesine rağmen, bu yöntemlerin hesaplama yükü çok fazladır ve pratikte sadece belirli sayıda atom içeren sistemler için kullanılabilirler. Atomsal dünyadan alınan bilgiler kullanılarak, moleküler mekanik temelli, hesaplama yükü çok daha az ve dolayısıyla çok daha fazla atom içeren modelleme yaklaşımları kurulabilir. Bu tezde grafen tabakalarının, karbon nanotüplerin, karbon nanokonilerin temel mekanik özellikleri, geliştirilen moleküler mekanik temelli sonlu elemanlar yaklaşımları ve çok ölçekli bir moleküler mekanik / sürekli ortamlar mekaniği yaklaşımı kullanılarak elde edilmiştir.

Kabul edilen moleküler mekanik temelli sonlu elemanlar modelleri, karbon esaslı malzemelerin dış kuvvetlerin etkisi altında, uzay kafes yapısı gibi davrandığı varsayımına dayanmaktadır. Karbon atomları sonlu elemanlar düğüm noktaları karbon atomları arasındaki kovalent bağlar ise Euler-Bernoulli kiriş elemanları kullanılarak modellenmiştir.

Karbon esaslı bu nanoyapıların küçük ve büyük yerdeğiştirme problemleri incelenirken sırasıyla harmonik ve geliştirilmiş Morse moleküler mekanik potansiyelleri kullanılmıştır. Küçük şekil değiştirme problemleri için bilinmeyen Euler-Bernoulli kiriş eleman parametreleri moleküler mekanik harmonik enerji terimleriyle ve benzer yapısal mekanik enerji terimlerinin eşitlenmesi yoluyla elde edilmiştir. Elde edilen bu değerler kullanılarak tek katmanlı karbon nano tüplerin, elastiklik modülleri, kayma modülleri, Poisson oranları, burkulma yükleri ve doğal frekans değerleri; grafen tabakalarının benzer şekilde elastiklik modülleri, kayma modülleri, Poisson oranları ve doğal frekans değerleri ve karbon nanokonilerin yatay ve dikey burkulma yükleri ve doğal frekanslar değerleri elde edilmiştir. Yapılan analizlerin sonucunda, karbon nanotüplerin ve grafen tabakalarının 1 TPa civarında

elastiklik modülüne, 0.5 TPa civarında kayma modülüne ve 1.5 THz varan doğal frekans değerlerine sahip olduğu ve ayrıca karbon nanokonilerin kritik burkulma yüklerinin ve doğal frekans değerlerinin, karbon nanotüplerin ve grafen tabakalarının kritik burkulma yükleri ve/veya doğal frekans değerlerinden birçok analizde yüksek olduğu bulunmuştur. Yapılan analizler sonucunda elde edilen bu sonuçların mevcut literatürdeki deneysel ve sayısal çalışma sonuçları ile uyumlu olduğu görülmüştür.

Bu tezde ayrıca bir grafen tabakasının dinamik davranışı geliştirilen moleküler mekanik temelli bir sonlu elemanlar yöntemi kullanılarak incelenmiştir. Literatürde bu yöntem kullanılarak grafen karbon esaslı nano yapıların titreşim özellikleri incelenirken global kütle matrisi genellikle karbon çekirdeklerinin kütleleri kafes yapıların düğüm noktalarına yapısal kütle olarak tatbik edilmesi ile elde edilir. Bu yaklaşım karbon esaslı nano yapıların titreşim özelliklerinin incelenmesi için yeterlidir. Fakat dinamik özellikleri incelenirken yakınsamama problemi doğurur. Bu yakınsama problemini ortadan kaldırmak için elemanların uyumlu kütle matrisleri kullanılmıştır. Uyumlu kütle matrislerini hesaplamak için gerekli eşdeğer eleman yoğunlukları, oluşturulan düzlem gerilme modeli doğal frekansları ile moleküler mekanik modellerin doğal frekanslarının eşitlenmesi ile elde edilmiştir. Sonuçta uyumlu kütle matrisi kullanılarak elde edilen doğal frekanslar ile toplanmış kütle matrisi ve düzlem gerilme modelleri kullanılarak elde edilen doğal frekans değerlerinin tutarlı olduğu görülmüştür. Grafen tabakalarının dinamik analizlerinde Newmark metodu kullanılmış ve grafen tabakalarının iki ve üç boyutlu dinamik davranışları incelenmiştir. Analizler sonucunda zamana karşı elde edilen yer değiştirme değerlerinin spektral analizlerinden, dinamik modellerin yapının davranışını çok iyi yansıttığı görülmüştür.

Tez kapsamında hatasız ve değişik hatalar barındıran grafen tabakalarının ve karbon nanotüplerin doğrusal olmayan kırılma davranışları incelenmiştir. Grafen tabakalarının ve karbon nanotüplerin doğrusal olmayan kırılma davranışları incelenirken küçük şekil değiştirme kabulü artık geçerli olmadığından, geliştirilmiş Morse potansiyel fonksiyonu kullanılarak Euler-Bernoulli kiriş elemanlarının doğrusal olmayan davranışları belirlenmiştir. Geliştirilen yöntem hem doğrusal olmayan malzeme davranışlarını hemde doğrusal olmayan geometrik etkileri dikkate almaktadır. Analizlerde hatasız, Stone-Wales ve tek atom boşluk hatası içeren grafen tabakaları ve hatasız, yeniden yapılandırılmış tek ve iki atom boşluk hatası içeren karbon nanotüplerin kırılma davranışları incelenmiştir. Hesaplamalar sonucunda hatasız ve hatalı grafen tabakalarına ve karbon nanotüplere ait kırılma gerilmesi, kırılma birim şekil değiştirme değerleri ve hasarların nasıl bir tarzda olduğu belirlenmiştir. Analizler sonucunda, doğrusal olmayan geometrik etkilerin grafen tabakalarının ve karbon nanotüplerin kırılma davranışlarında etkili olduğu, Stone-Wales ve atom boşluk hatalarının bu malzemelerin kırılma değerlerini oldukça düşürdüğü, her iki malzemede de kırılmanın gevrek tarzlarda olduğu görülmüştür. Ayrıca grafen tabakalarının ve karbon nanotüplerin kırılma davranışlarının yöne bağımlı olduğu; belirli yönlerde bu malzemelerin kırılmaya karşı daha dayanıklı oldukları görülmüştür. Elde edilen sonuçlar incelendiğinde, bulunan kırılma gerilmesi ve birim şekil değiştirme değerleri ile kırılma tarzının literatürdeki sonuçlar ile oldukça uyumlu olduğu görülmüştür.

Büyük boyutlarda veya fazla sayıda atom içeren nano yapıların tümü atomsal modeller kullanılarak yapılan analizlerin hesaplama yükleri oldukça fazladır. Bu hesaplama yüklerini kabul edilebilir seviyelere düşürmek, bunun yanında hesaplama hatalarını kabul edilebilir sınırlar içinde tutmak için bu çalışmada, grafen

tabakalarının statik ve kırılma davranışlarının belirlenmesi için çok ölçekli bir modelleme yaklaşımı geliştirilmiştir. Moleküler mekanik ve düzlem gerilme modellerinin birleşik formülasyonunu elde etmek için geliştirilen bu çok ölçekli bağlama yaklaşım; moleküler mekanik ve düzlem gerilme yer değiştirme alanlarının en küçük kareler yöntemi mantığıyla birleştirilip, oluşan kısıtsız optimizasyon probleminin çözülmesine dayanır. Birleşik moleküler mekanik ve düzlem gerilme modellerinin çözümü için Lagrange çarpanları yöntemi kullanılmıştır. Kabul edilen bu çok ölçekli yaklaşımın ana avantajı, moleküler mekanik alanı veya alanları ile herhangi bir düzlem gerilme elemanı veya elemanları arasındaki birleşimin, doğru izdüşüm matrislerinin kullanılması ile çözüm ağını değiştirmeden kolaylıkla sağlanabilmesidir. Bu sayede, geliştirilen yaklaşım düzlem gerilme alanı üzerindeki herhangi bir eleman veya elemanlarda atomsal ölçeklerde çok hızlı analizler yapılabilmesine olanak sağlar. Kabul edilen yaklaşımın etkinliği, hatasız ve hatalı grafen tabakalarının statik ve/veya kırılma problemlerinde gösterilmiştir. Atomal modellerde, harmonik ve geliştirilmiş Morse potansiyel fonksiyonları kullanılmıştır. Sonuçta, kabul edilen çok ölçekli formülasyonun grafen tabakalarının statik ve kırılma davranışlarını oldukça yüksek doğrulukta hesapladığı görülmüştür. Bu yaklaşım diğer birçok nano yapıdaki malzemelerde atomal sonuç istenen bölge veya bölgelere kolaylıkla uygulanabilir.

1. INTRODUCTION

Since the experimental detection of carbon nanotubes (CNTs) in 1991 [1], extensive studies have been conducted on its extraordinary properties and researchers have been interested in other carbon based nanostructures such as graphene sheets (GSs) and carbon nanocones (CNCs). CNT can be viewed as a GS rolled into a tube and exhibits exceptional mechanical, thermal and electrical properties such as approximate Young's modulus of 1.0 TPa and thermal conductivity of 3000 W/mK [2,3].

On the other hand, GSs possess most of the extraordinary properties of CNTs [3-5]. Graphene is the basic structural element of CNTs, CNCs and fullerenes; as a result, it is the starting point of material models of these carbon structures. Recently, new techniques were developed for mass production of GSs [5, 6], and subsequently the potential of using these nanostructures for multiple usages such as nanosensors, nanocomposites, nanooscillators and nano-electro-mechanical systems has been increasing [7, 8].

Similar to CNTs and GSs, CNCs are conical graphitic structures and have very promising mechanical, electrical and thermal properties [9-14]. Ge and Sattler [15] first proposed that five apex angles such as 19.2° , 38.9° , 60° , 86.6° and 123.6° can be used to distinguish CNCs. Krishnan et al. [16] verified the existence of the five types of CNCs experimentally. CNCs are suited for high resolution and/or high intensity applications due to its small size, high stiffness and conical geometry; thus, it can be used as scanning probe tips (i.e., atomic force microscope (AFM) and scanning tunneling microscope (STM) probes), electron field emitters and in nanoindentation applications [16-20].

Prediction of mechanical properties of carbon base structures is important and very useful in the design of materials made of these structures. Experimental measurements [21-29] and computational simulations are commonly used to characterize carbon base structures. Since experimental measurements of mechanical

properties of carbon based structures are very costly due to its nanoscale dimensions, powerful computational simulation tools are widely employed to characterize these nano structures.

Computational approaches can be classified as atomistic and continuum modeling methods. Known as being very accurate, atomistic modeling methods are based on principles of quantum-molecular mechanics including the classical molecular dynamics (MD) and *ab initio* methods; on the other hand, they are computationally much more expensive than using the continuum models and only suitable for small systems having limited number of atoms and very short time scales [30-32]. Continuum modeling approaches are based on simulating carbon base structures with well-known structural members such as beams, shells and plates.

Atomistic based finite element (FE) modeling approaches have been used to analyze carbon based structures in many recent works in literature due to its computational cost and CPU time advantages. In this thesis, equivalent models of single-layer graphene sheets (SLGSs), single wall carbon nanotubes (SWCNTs) and single wall carbon nanocones (SWCNCs) are developed by using molecular mechanic (MM) based FE approach. Then, elastic, fracture, vibrational and buckling characteristics of SWCNTs; vibrational and elastic buckling characteristics of SWCNCs, and elastic, fracture and vibrational characteristics of SLGSs are investigated. In addition, an equivalent dynamic model is developed for SLGSs, and then 2-D and 3-D transient behavior of SLGSs are investigated. Moreover, multiscale models of SLGSs are developed for coupling of atomistic and continuum methods.

Relevant works about elastic, vibrational and buckling behavior of GSs, CNTs and CNC in literature are summarized as follows. Odegard et al. [33] developed a model that links the molecular mechanics and solid mechanics, which is established by equating the molecular potential energy terms with the mechanical strain energy of a representative volume element of a continuum model. Li and Chou in the works [34-36] developed a similar approach named “molecular structural mechanics” to model CNTs and GSs similar to space-frame structures and investigated the elastic and vibrational characteristics of CNTs and GSs. In their approach, Euler-Bernoulli beam elements are used to represent covalent bonds between carbon atoms; then, unknown beam parameters are obtained by using energy equivalence of the MM and continuum mechanic (CM) models. Harmonic expressions for potential energy term

are used in molecular structural mechanics [34] and applied to small deformation of CNTs and GSs. Tserpes and Papanikos [37] introduced an atomistic base FE method, based on the approach of Li and Chou [34] to model CNTs by using commercial FE codes. Elastic characteristics of SLGSs are studied by Sakhaee-Pour [38]. By using the methods developed by Li and Chou [34] and Tserpes and Papanikos [37], Sakhaee-Pour et al. [39] and Hashemnia et al. [40] studied natural frequencies and mode shapes of SLGSs, and Fan et al. [41] and Cheng et al. [42] examined mechanical properties of CNTs such as Young's modulus, natural frequency and buckling load. In addition, Lee and Lee [43] examined vibration properties of CNTs and CNCs by using the approach presented in [34,37] and predicted fundamental frequencies of SWCNCs below 20 GHz with a cone having the height of 20 Å. Sadeghi and Naghdabadi [44] introduced a hybrid atomistic-structural element to model linear and nonlinear vibrations of GSs in which hybrid element formulation is based on a nonlinear inter-atomic potential function that can model nonlinear dynamic response of GSs. Wang et al. [45], Kitipornchai et al. [46] and He et al. [47] presented the vibration analysis of multi-walled graphene sheets (MWGSs) using continuum-plate models. Atalaya et al. [48] derived a nonlinear finite elasticity theory for graphene resonators for both elastostatics and elastodynamics problems. Scarpa et al. [49] developed truss-type analytical models to describe linear elastic properties of GSs. Then, Scarpa et al. [50] analyzed natural frequencies and acoustic wave propagation characteristics of graphene nanoribbons where an equivalent atomistic-continuum FE model is employed by using the formulation in [49]. Chowdhury et al. [51] studied transverse vibrations of GSs using the MM approach. Gupta and Batra [52] analyzed elastic and vibrational properties of GSs by using MM simulations. Mianroodi et al. [53] examined nonlinear vibration properties of SLGSs using a membrane model. Ansari et al. [54] studied to investigate the vibrations of single layer GSs using a nonlocal continuum plate model. Arash and Wang [55] investigated free vibrations of SLGSs and MLGSs by employing nonlocal continuum theory and molecular dynamics simulations. Chandra et al. [56] examined the vibrations of bilayer GSs by using analytical and atomistic FE models. Avila et al. [57] analyzed elastic and vibrational properties of graphene based nanostructures by using MM based FE approach. Gibson et al [58] briefly reviewed some numerical and experimental studies about the vibrations of CNTs and their composites. Li and Chou in the works [59] investigated buckling characteristics of CNTs by using

molecular structural mechanic approach. Both axial compression and bending loading conditions are considered in the elastic buckling behavior of the CNTs in [59] where buckling forces are reported to be in the range of $\sim 0.1\text{--}39$ nN. Li and Chou [59] reported that the buckling load in axial compression is higher than bending load for CNTs. Sakhaee-Pour [60] analyzed elastic buckling of SLGSs by using atomistic based FE approach. Mir et al. [61] studied natural frequencies and mode shapes of SWCNTs by using atomistic based FE approach. Computational tools are widely used to characterize mechanical properties of CNCs [13, 14, 43, 62–65]. Kumar et al. [13] investigated the Young's and shear modulus of CNCs employing second-generation reactive empirical bond-order potential. Wei et al. [14] examined the elastic and plastic properties of SWCNCs by using MD simulations. Tsai and Fang [62] and Liew et al. [63] analyzed the buckling behavior of CNCs by using MD simulations. Liao et al. [64] investigated tensile and compressive behaviors of open-tip CNCs employing MD simulations. Abadi et al. [65] studied free vibrational properties of CNCs based on a nonlocal continuum shell model.

In the works [34–42, 57, 59–61], Euler-Bernoulli beam elements are used to represent bond interactions between C-C atoms in GSs, CNTs and CNCs. On the other hand, Scarpa and Adhikari [49] proposed a beam model considering the shear deformation effects and they found the C-C bond thickness d , Poisson's ratio ν , Young's modulus E and shear modulus G by using the AMBER force model constants [34]. Both of the models in Li and Chou [34] and Scarpa and Adhikari [49] yield the same deformation results as the structural mechanic stiffness constants in the AMBER force model are equal if the corresponding element properties are used. Lee and Lee [43] used Timoshenko beam element formulations which include shear deformation effects but they employed Euler-Bernoulli beam element constants [37]; this assumption affects the natural frequencies of SWCNC that are found to be lower than those of Euler-Bernoulli beam elements. If shear deformation effects are considered, parameters of shear beam formulations given in Scarpa and Adhikari [49] should be used. Even though there are some studies on nanocones, a few studies exists on buckling behavior of SWCNCs by using atomic based FE approach. In addition, Lee and Lee [43] studied of vibrations of SWCNCs; however, they did not examine the effects of cone height and used Timoshenko beam formulations with Euler-Bernoulli beam parameters which may lead to lower modal frequencies than actual values.

Motivated by these facts, mechanical properties of SLGSs, SWCNTs and SWCNCs are obtained by using the MM based FE approach [34, 37] where Euler-Bernoulli beam elements with consistent mass matrix is used.

Although there are numerous studies on static and quasi-static problems of SLGSs and CNTs in literature [34-43], no work exists on dynamic analyses of SLGSs and CNTs by the use of beam analogy and FE formulations based on the MM model. Development of accurate FE models based on the MM principles will enable fast analysis of nanostructures. In this thesis, modal and dynamic analyses of SLGSs are completed by using the beam analogy and consistent mass matrices. In the works [35, 36, 39-43, 55, 57] studying the vibrations of GSs and CNTs, the global mass matrix is derived based on the assumption that the carbon nuclei masses (e.g., 1.9926×10^{-26} kg) are concentrated at the joints of the frame structure. Due to the negligible radius of carbon atomic nucleus (e.g., $r_c = 2.75 \times 10^{-5}$ Å), torsional and flexural rotation coefficients of mass matrices are assumed to be zero and a lumped mass matrix for the beam elements is used, which is sufficient to study the vibrations of GSs and CNTs; nonetheless, it yields singularity problems in transient analyses unless special measures are taken. On the other hand, to obtain natural frequencies and corresponding modes of CNTs, consistent mass matrices are considered in [61], where the density of beam elements is selected to be the density of the CNT in the associated MM models. However, due to this assumption, the total mass of the MM model is different from the mass of the original structure which also affects the associated natural frequencies. Hence, an equivalent model for SLGSs in transient analyses is developed in this thesis by using an atomistic FE approach [34] that employs a consistent mass matrix of Euler Bernoulli beam elements in which an equivalent density parameter for the beam elements is derived by the equivalency of natural frequencies of the MM model and continuum plane-stress FE model. In addition, the Young's modulus and Poisson's ratio of plane stress model are obtained by using the MM model. It is shown that the proposed approach can reflect 2-D and 3-D vibrational characteristics of SLGSs. Moreover, the response to initial displacements are computed for two- and three-dimensional FE models where initial displacements are applied incrementally on SLGSs and nodal coordinates of the original SLGS structure are updated at each displacement increment; hence, large deformation effects and uniform initial displacement conditions are considered in all

analyses. It is noteworthy that the Morse potential can easily be adapted to include nonlinear effects in our analyses. The Newmark method is employed to integrate the associated equations of transient analyses. It is also shown that power spectral density (PSD) properties of transient analyses are in good agreement with modal features of SLGSs, that verifies the numerical results. Comparisons are made among the results of the MM based model, CM based model and relevant works in literature.

Relevant works about fracture behavior of GSs and CNTs in literature are summarized as follows. Experimental observations show that some defects such as one atom vacancy and Stone-Wales (SW) defects commonly exist in CNTs and GSs. These defects may be induced due to stress or may emerge during the growth or processing [29, 66- 71] and negatively affect mechanical strength of these carbon based structures. Hence, prediction of mechanical behavior of defected carbon based structures is important and very useful in the design of materials having nanographene structures. Lee et al. [21] studied experimentally the elastic properties and intrinsic breaking strength of free-standing monolayer graphene membranes and measured the Young's modulus of 1.0 TPa and tensile strength of 130 ± 10 GPa. Yu et al. [29] investigated the tensile strength of MWCNTs experimentally and found it in the range of 11 to 63 GPa. Atomistic modeling methods such as quantum mechanic (QM) and MD simulations are commonly used to determine the effects of defects on mechanical properties of GSs and CNTs in literature [72-84]. However, despite of their accuracy, atomistic modeling approaches are computationally very expensive than continuum modeling approaches. Tserpes et al. [85] proposed an atomistic-based progressive fracture model for simulating the fracture behavior of SWCNTs by using commercial FE codes, where non-linear characteristic of Euler-Bernoulli (EB) beam elements (i.e., Beam4 element in ANSYS) is obtained by using the modified Morse potential. Tserpes and Papanikos [86] studied the effect of the SW defect on the fracture behavior of SWCNTs. By using commercial FE codes, Mohammadpour and Awang [87] studied tensile properties of SWCNTs by using an approach similar to Tserpes et al. [85] and represented carbon-carbon (C-C) bonds by using Timoshenko beam elements (i.e., Beam188 element in ANSYS). Wernik and Meguid [88] analyzed the nonlinear mechanical properties of SWCNTs by using an atomistic-based continuum modeling technique, where beam and rotational spring

elements are used to represent stretching and angle-bending component of the modified Morse interatomic potential. Xiao et al. [89] developed an atomistic based finite bond element model for the prediction of fracture and progressive failure of defect-free and defected SLGSs and SWCNTs, whose model is equivalent to the analytical molecular structural mechanical model in the work [90] for defect-free SWCNT. Xiao et al. [91] also studied effects of multiple SW defects on mechanical properties of GSs and CNTs. Rossi and Meo [92] studied mechanical properties of SWCNTs by using FE models based on the MM models. The interactions between the C-C bonds are modeled by using non-linear elastic and torsional spring elements in [92]. Rossi and Meo [93, 94] also examined tensile properties (i.e., ultimate strength and strain) of SWCNTs. Georgantzinos et al. [95] analyzed stress-strain behavior of SLGSs by using a spring-based FE model. Sun and Zhao [96] investigated tensile stiffness and strength of SWCNTs by using the MM based FE approach where the C-C bonds are simulated with two node elastic rod elements.

Although progressive fracture of SLGSs and SWCNTs are studied earlier, they are obtained without consideration of geometric nonlinear effects. However, the fracture in these nanostructures occur at relatively large strain values; hence, large deformation effects and geometric nonlinearities have to be considered which are the main motivation behind this study and examined in this paper. In this study, equivalent nonlinear SLGS and SWCNTs fracture models are developed by using the atomistic based FE approach in which the modified Morse potential along with an iterative solution procedure is used. The proposed model is basically a combination of the structural mechanic approach of Li and Chou [34] and the atomistic-based progressive fracture model of Tserpes et al. [37]. To this end, we coded our own SLGSs and SWCNTs FE models by using MATLAB®, and large deformation and nonlinear geometric effects are taken into account. At each load step, initial displacement is applied incrementally on SLGSs and SWCNTs, and atomistic coordinates of the original SLGS and SWCNTs structures are updated. Formulation underlying the proposed approach is applied to pristine and defected (i.e., SW and one atom vacancy defects) zigzag and armchair SLGSs and pristine, reconstructed and non-reconstructed one- and two-atom vacancy defected zigzag and armchair SWCNTs. The initial reconstructed nanotube models are obtained by using MD

simulations. The numerical results are compared with and found to be in good agreement with the results reported in literature.

Recently developed multiscale modeling techniques yield promising results in treating the bridging phenomena at atomistic and continuum scales. The aim of these methods is to solve problems in different scales efficiently such as QM/MM/quasi-continuum mechanics (QCM)/CM [77, 97-99]. Those methods have taken the advantages of both atomistic and continuum models. For example, in studying fracture, the MM models are used to obtain more accurate results in the small domain around the crack where bond breaking is expected, while the CM models based on the FE method are used to obtain more efficient solution away from the crack where a homogeneous and smooth deformation field is expected. The bridging scale method [100-101], Arlequin method [102-103], bridging domain method [76, 104-107], handshake or coupled length scale methods [108-110] and generalized space-time mathematical homogenization theory [111] are some of these methods used to link atomistic and continuum models. The Arlequin, bridging domain and handshake methods are overlapping domain decomposition methods, in which strain energies of the atomistic and continuum models are scaled in the overlapping domain. Compatibility of the models is enforced by using Lagrange multipliers in the Arlequin and bridging domain methods. On the other hand, the bridging scale method used for coupling of MD and CM models does not contain an overlapping domain. This method consists of a two-scale decomposition such as a coarse scale to represent the CM model and a fine scale to represent atomistic model, and these scales evolve on separate time scales. A projection of the fine scale solution onto the solution of the coarse scale model is used to link the models. The handshake methods use continuum and atomistic models; atomistic and continuum models are overlapped and contribution of each model to the Hamiltonian is taken to be average of the two Hamiltonians. The homogenization theory constructs an equivalent continuum description directly from MD equations. A brief review of available these coupling methods can be found in [112-114].

In this thesis, a coupling method for the MM and CM models is derived based on an augmented formulation of atomistic and continuum displacement fields in a moving least square sense, which originates from an unconstrained optimization problem to be solved. In order to solve the augmented problem, the Lagrange multiplier method

is used which allows multiscale analyses of multiple numbers of MM domains in a single CM domain. The CM domain covers entire domain and the MM domain is patched on the element(s) of the CM domain. In contrast to alternative approaches existing in literature, there is no need for an overlapping domain in the proposed approach and the MM domain(s) can be placed arbitrarily in the CM domain; hence, one can focus on any desired subdomain where we need to obtain atomistic solution. In addition, there is no need for a constraint on the meshes of the MM and CM domains. Efficiency of the proposed approach is illustrated by using defect-free and defected monolayer graphene layers. In the atomistic models, harmonic potentials and modified Morse potentials are employed. In the CM domain, it is assumed that deformations are elastic and plane stress conditions exist, for which elasticity modulus and Poisson's ratio values of the CM domain are obtained by the use of full MM models, and compared with the results presented in literature. It is shown that the proposed formulation can compute the deformations of monolayer graphenes in high accuracy, enables to obtain the MM solution(s) in any part of the CM domain and can be applied to other nano structured materials. Main advantage of the proposed formulation is that it can be used to connect the MM domain(s) to any subdomain of the CM domain by proper choice of projection matrices without changing the mesh. Therefore, it enables fast reanalysis of any subdomain of the CM domain at fine scales. In addition, appropriate stiffness matrices of the MM and CM domains which exported as superelements can be embedded into the formulations that enables linking by commercial softwares. By updating the elasticity parameters of the CM domain based on the MM solutions, nonlinear effects are easily considered in iterative solutions of large deformation problems that provide more accurate nonlinear solutions.

2. STRUCTURES OF CARBON- BASED NANOSTRUCTURES

Graphene is a term that refers to one atom thick planar sheet of covalently bonded carbon atoms which are densely packed in a honeycomb crystal lattice. Graphite is a basic material found in nature and when taken apart graphite sheets become graphene. Rolled up layer of a GS forms CNT and folded up of a GS becomes fullerene (i.e., see Figure 2.1).

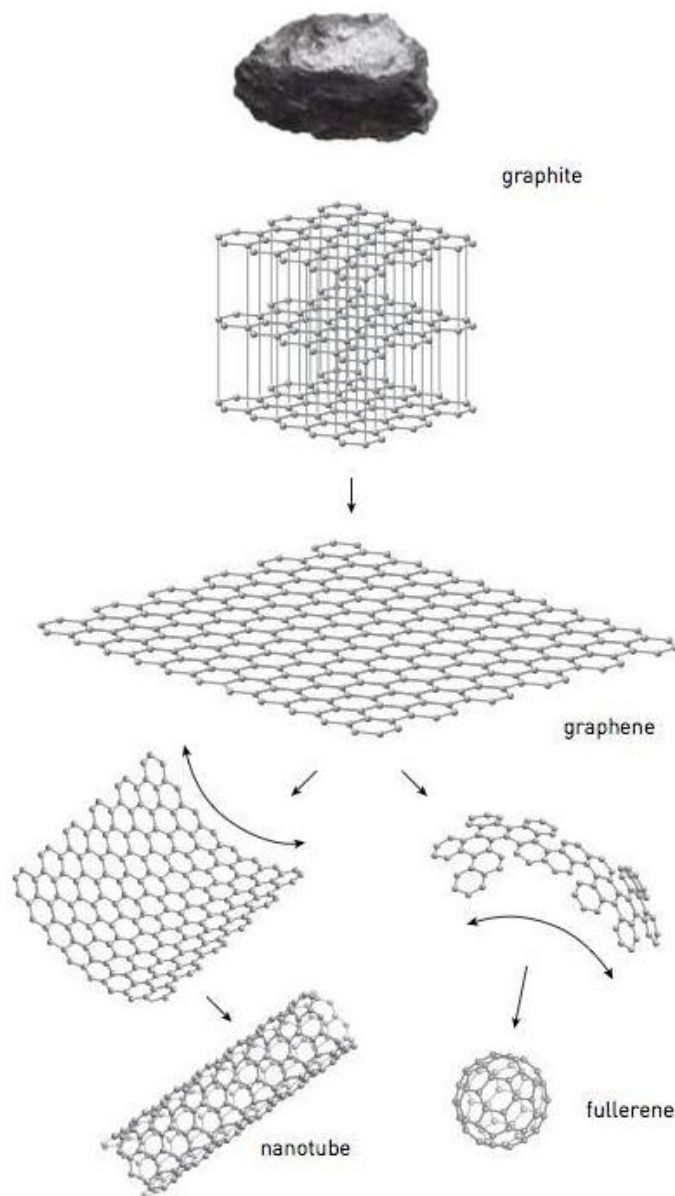


Figure 2.1: Graphite, graphene, CNT and fullerene [115].

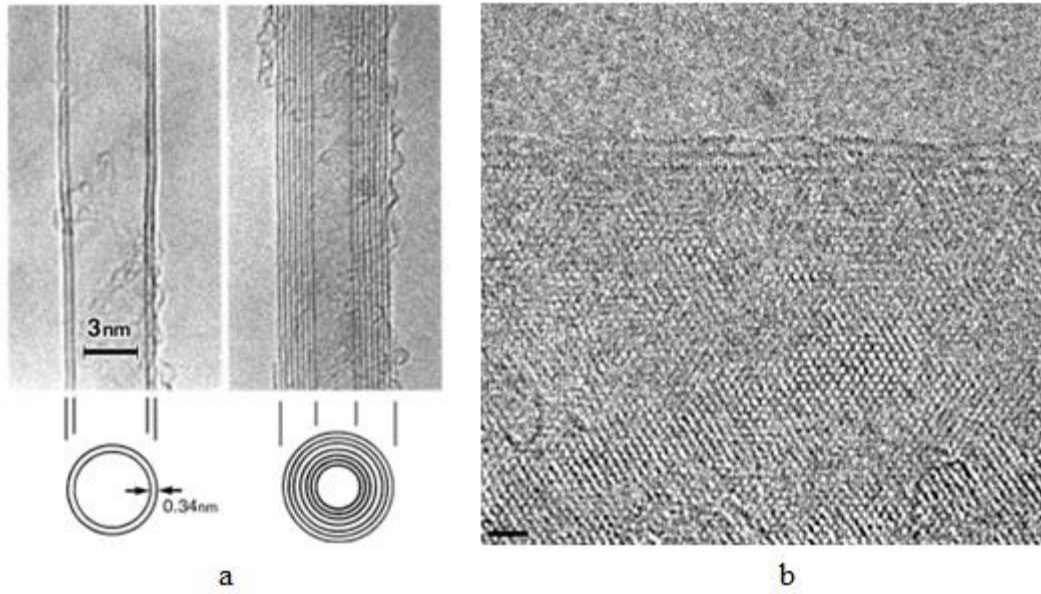


Figure 2.2: (a) Multi-layer carbon nanotube (MLCNTs) [1,116], (b) graphene membrane [117].

Figure 2.2 (a) shows the electron micrographs of microtubules of graphitic carbon with outer diameter of 4-30 nm and length of up to 1 μm . These tubes consisted of two or more seamless graphene cylinders concentrically arranged [116]. Figure 2.2 (b) shows the TEM image of a few-layer graphene membrane near its edge where the number of dark lines indicates the thickness of two to four layers [117]. Figure 2.3 shows the transmission electron micrographs (TEM) of the four distinctly different types of nano cones.

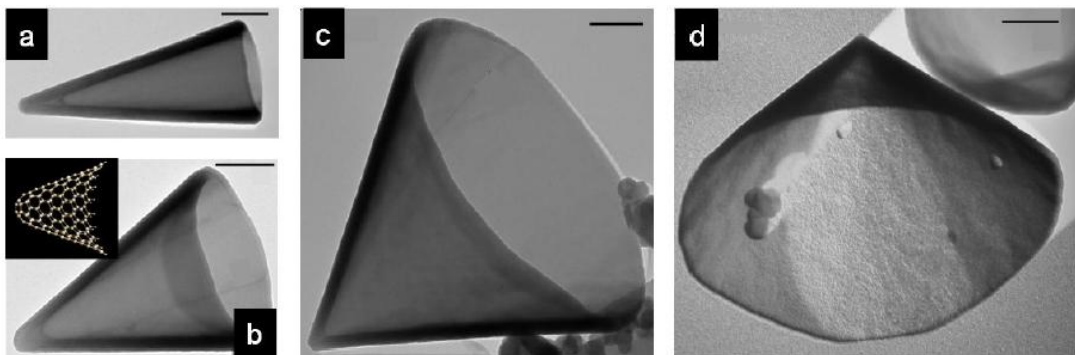


Figure 2.3: TEM images of carbon nanocones, (a)-(d) shows cones with nominal apex angle $\alpha = 19.2^\circ, 38.9^\circ, 60^\circ$ and 83.6° , respectively [118].

The CNTs, GSs and CNCS are composed of covalently bonded carbon atoms which are densely packed in a hexagonal carbon rings. The covalent bond is a very strong bond and significantly contributes to the mechanical properties of carbon based structures. The atomic structures of CNTs depend on the tube chirality, which is defined by the chiral vector C_h and the chiral angle θ (see Figure 2.4). The chiral vector C_h can be defined in terms of the lattice translation indices (m,n) and the basic vectors a_1 and a_2 of the hexagonal lattice as follows

$$C_h = ma_1 + na_2 \quad (2.1)$$

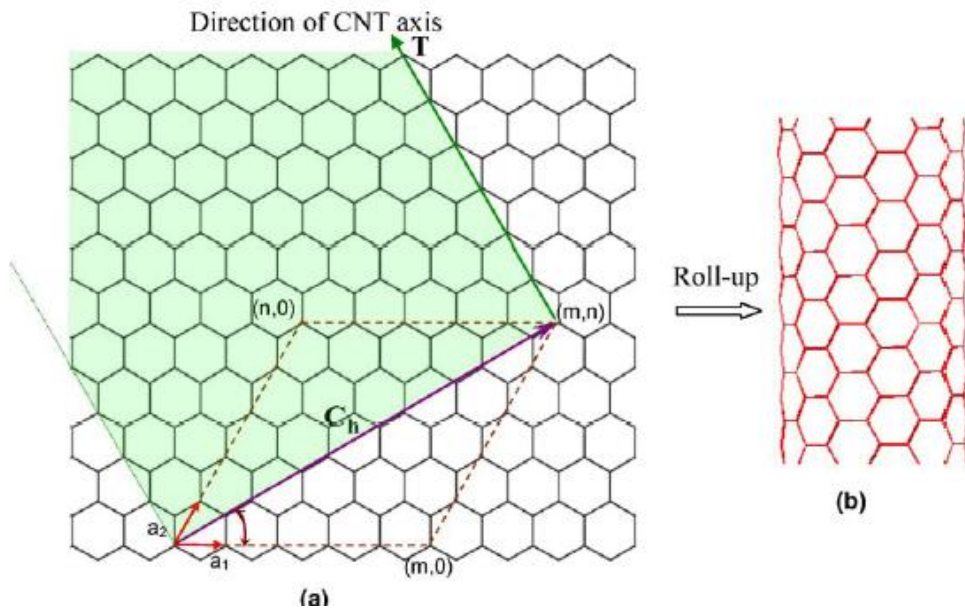


Figure 2.4: Roll-up vector defining the structures of CNTs (a) GS and (b) SWCNTs [119].

The chiral angle θ is defined as the angle between vectors C_h and a_1 and calculated as follows

$$\theta = \sin^{-1} \left[\frac{\sqrt{3}m}{2\sqrt{n^2 + mn + m^2}} \right] \quad (2.2)$$

The CNT diameter and chirality are completely specified by the two integers (m,n), which are referred as the chiral indices of the CNTs. Table 2.1 shows the three major categories of CNTs and Figure 2.5 shows these types of CNTs.

Table 2.1: Types of CNTs based on chiral indices.

Nanotube type	Chiral indices (m,n)	Chiral angle, θ
Armchair	(m,m)	30°
Zig-zag	($m,0$)	0
Chiral	(m,n); $m \neq n \neq 0$	$0 < \theta < 30^\circ$

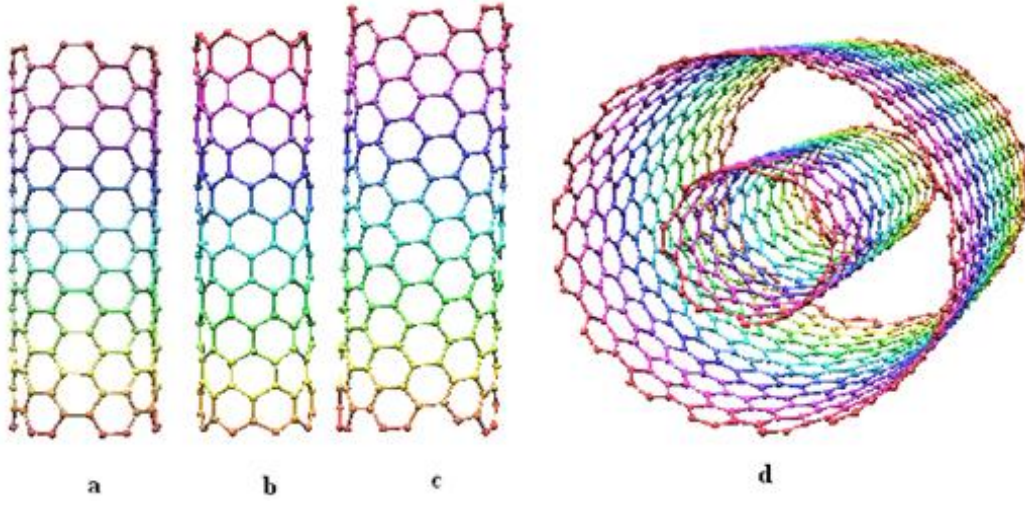


Figure 2.5: CNTs (a) armchair (6,6), (b) zig-zag (8,0), (c) chiral (8,5) (d) MWCNT (7,7) (10,10).

The length of chiral vector and the diameter of any CNT can be respectively calculated as follows

$$L = |\mathbf{C}_h| = a\sqrt{n^2 + mn + m^2} \quad (2.3)$$

$$d_t = \frac{L}{\pi} = \frac{a\sqrt{n^2 + mn + m^2}}{\pi} \quad (2.4)$$

where a is the lattice constant of graphite and equal to $a = |\mathbf{a}_1| = |\mathbf{a}_2| = \sqrt{3}a_{C-C}$ and a_{C-C} is the carbon-carbon (C-C) bond length and equal to 1.421 Å.

The electronic properties of CNTs are dependent on the chirality. The condition for achieving metallic CNTs can be expressed by $m-n=3q$, where q being an integer [120]. Figure 2.6 shows that every possible CNTs configuration (m,n) can be mapped by symmetry operations on the red and blue colored circles.

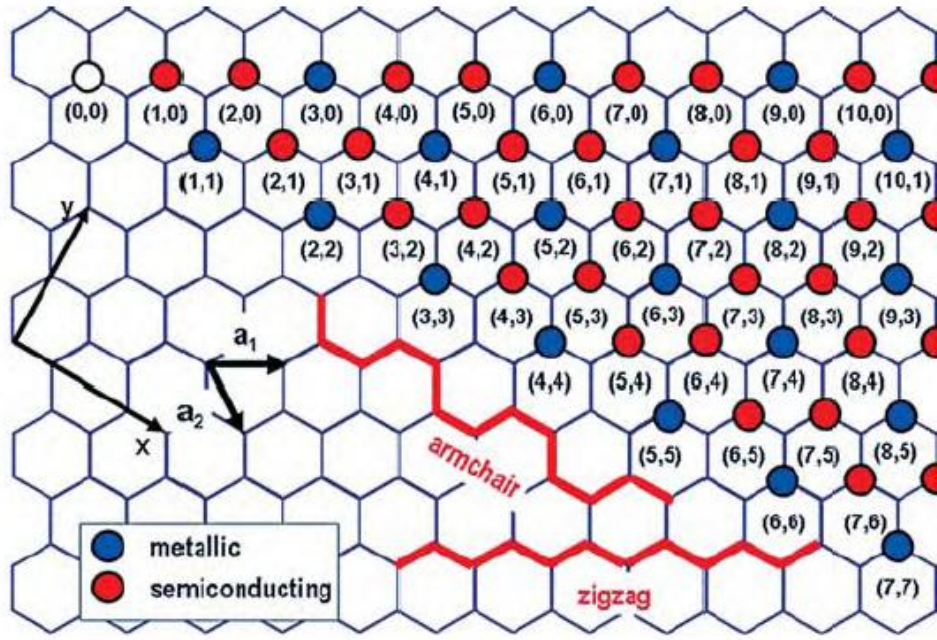


Figure 2.6: A map showing which (m,n) gives semiconducting and metallic tubes can be drawn. Only armchair CNTs ($m=n$) are strictly metallic [120].

CNCs having five possible closed cone structures can be constructed by using GSs [121, 122]. By rotating a fragment of GSs in multiples of 60° , we obtain the original structure due to the hexagonal symmetry of GSs that is the only way to generate smoothly joined CNCs by folding over a GS and the overlaps are called the disclinations. Folding over a GS in this manner creates five possible closed distinct CNC structures and the apex angles of a cone can be calculated as follows [123]

$$\alpha = 2 \arcsin\left(1 - \frac{\theta}{360}\right) \quad (2.5)$$

where θ is the disclination angle in degrees. Taking θ as 60° , 120° , 180° , 240° and 300° , the apex angles of CNCs are calculated 112.9° , 83.6° , 60° , 38.9° and 19.2° , respectively (i.e., see Figure 2.3). The CNTs can be seen as a special case of the CNCs with a zero apex angle. Figure 2.7 shows the cone sheet with the dislocation angle of 240° corresponding to the cone with the apex angle of 38.9° SWCNC.

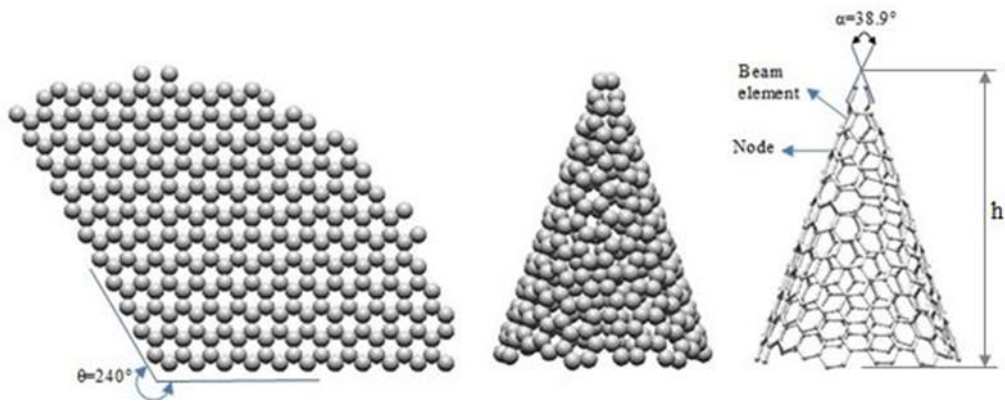


Figure 2.7: The cone sheet with the dislocation angle of 240° corresponding to the cone with the apex angle of 38.9° SWCNC.

3. FINITE ELEMENT MODELS OF CARBON-BASED NANOSTRUCTURES

3.1 FE Formulation

For the simulation of static and dynamic behaviors of SLGSs, SWCNTs and SWCNCs, an atomistic modeling approach is used. When carbon based nanostructures such as GSs, CNTs and CNCs are subjected to external forces, the positions of the atomic nuclei are controlled by the covalent bonds between C-C atoms. Hence, deformation pattern of these nanostructures is very similar to deformation of frame structures. To this end, SLGSs, SWCNTs and SWCNCs are modeled as 2- D and/or 3-D frame-like structures in simulations and a covalent bond between two carbon atoms is represented by an Euler-Bernoulli beam element having consistent mass matrices. Figures 3.1-3.3 show the molecular and equivalent FE models of the SLGS, SWCNT and SWCNCs, respectively.

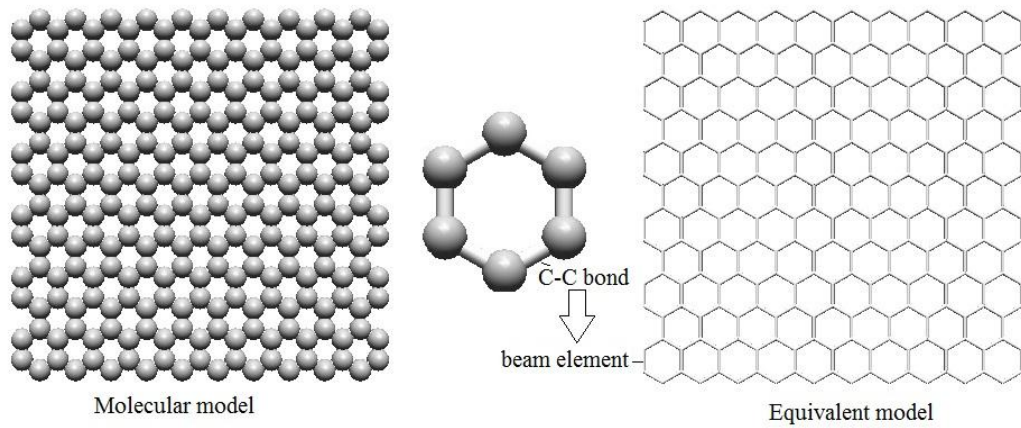


Figure 3.1: Molecular and equivalent FE models of the graphene layer.

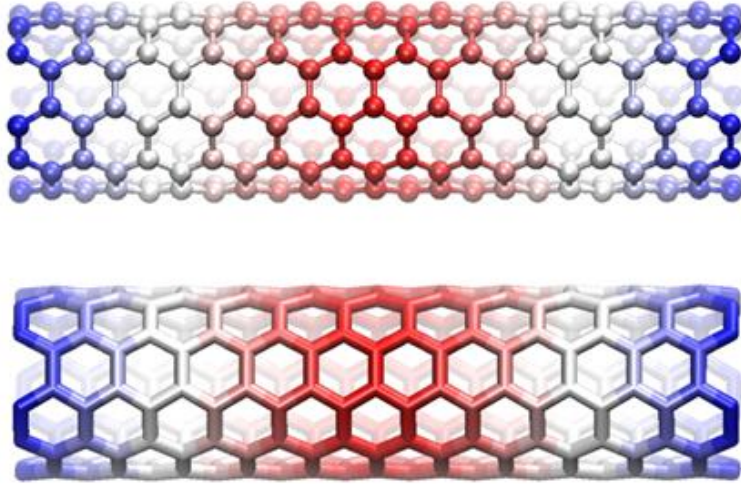


Figure 3.2: Molecular and equivalent FE models of the SWCNT.

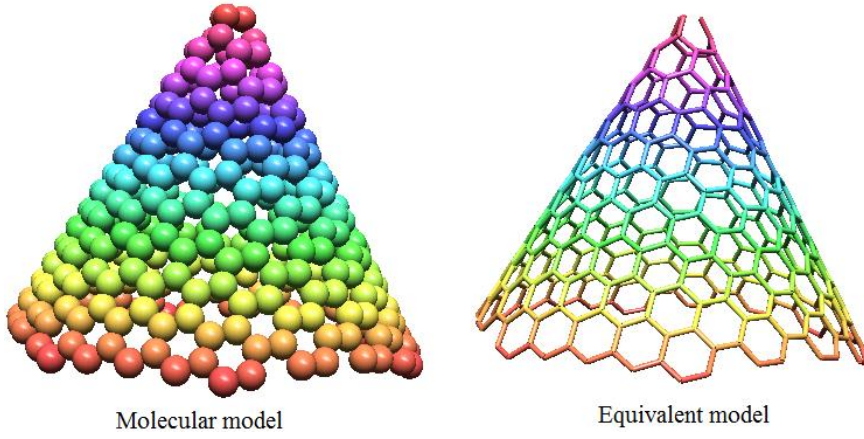


Figure 3.3: Molecular and equivalent FE models of the SWCNC.

The element stiffness matrix and consistent mass matrix for a planar Euler-Bernoulli beam element are given by equations (3.1) and (3.2), respectively.

$$\mathbf{K} = \begin{bmatrix} \frac{EA}{L} & 0 & 0 & -\frac{EA}{L} & 0 & 0 \\ 0 & \frac{12EI}{L^3} & \frac{6EI}{L^2} & 0 & -\frac{12EI}{L^3} & \frac{6EI}{L^2} \\ 0 & \frac{6EI}{L^2} & \frac{4EI}{L} & 0 & -\frac{6EI}{L^2} & \frac{2EI}{L} \\ -\frac{EA}{L} & 0 & 0 & \frac{EA}{L} & 0 & 0 \\ 0 & -\frac{12EI}{L^3} & -\frac{6EI}{L^2} & 0 & \frac{12EI}{L^3} & -\frac{6EI}{L^2} \\ 0 & \frac{6EI}{L^2} & \frac{2EI}{L} & 0 & -\frac{6EI}{L^2} & \frac{4EI}{L} \end{bmatrix} \quad (3.1)$$

$$\mathbf{M} = \rho AL \begin{bmatrix} \frac{1}{3} & 0 & 0 & \frac{1}{6} & 0 & 0 \\ 0 & \frac{13}{35} & \frac{11L}{210} & 0 & \frac{9}{70} & -\frac{13L}{420} \\ 0 & \frac{11L}{210} & \frac{L^2}{105} & 0 & \frac{13L}{420} & -\frac{L^2}{140} \\ \frac{1}{6} & 0 & 0 & \frac{1}{3} & 0 & 0 \\ 0 & \frac{9}{70} & \frac{13L}{420} & 0 & \frac{13}{35} & -\frac{11L}{210} \\ 0 & -\frac{13L}{420} & -\frac{L^2}{140} & 0 & -\frac{11L}{210} & \frac{L^2}{105} \end{bmatrix} \quad (3.2)$$

The element stiffness matrix and consistent mass matrix for a 3-D Euler-Bernoulli beam element are given by equations (3.3) and (3.4).

$$\mathbf{K} = \begin{bmatrix} K_{ii} & K_{ij} \\ K_{ij} & K_{jj} \end{bmatrix}, \quad \mathbf{M} = \begin{bmatrix} M_{ii} & M_{ij} \\ M_{ij} & M_{jj} \end{bmatrix} \quad (3.3)$$

where the sub-matrices, K_{ii} , K_{ij} , K_{jj} , M_{ii} , M_{ij} and M_{jj} are given by

$$K_{ii} = \begin{bmatrix} \frac{EA}{L} & 0 & 0 & 0 & 0 & 0 \\ 0 & \frac{12EI_x}{L^3} & 0 & 0 & 0 & \frac{6EI_x}{L^2} \\ 0 & 0 & \frac{12EI_y}{L^3} & 0 & -\frac{6EI_y}{L^2} & 0 \\ 0 & 0 & 0 & \frac{GJ}{L} & 0 & 0 \\ 0 & 0 & -\frac{6EI_y}{L^2} & 0 & \frac{4EI_y}{L} & 0 \\ 0 & \frac{6EI_x}{L^2} & 0 & 0 & 0 & \frac{4EI_x}{L} \end{bmatrix}$$

$$K_{ij} = \begin{bmatrix} -\frac{EA}{L} & 0 & 0 & 0 & 0 & 0 \\ 0 & -\frac{12EI_x}{L^3} & 0 & 0 & 0 & \frac{6EI_x}{L^2} \\ 0 & 0 & -\frac{12EI_y}{L^3} & 0 & -\frac{6EI_y}{L^2} & 0 \\ 0 & 0 & 0 & -\frac{GJ}{L} & 0 & 0 \\ 0 & 0 & -\frac{6EI_y}{L^2} & 0 & \frac{2EI_y}{L} & 0 \\ 0 & -\frac{6EI_x}{L^2} & 0 & 0 & 0 & \frac{2EI_x}{L} \end{bmatrix}$$

$$K_{jj} = \begin{bmatrix} \frac{EA}{L} & 0 & 0 & 0 & 0 & 0 \\ 0 & \frac{12EI_x}{L^3} & 0 & 0 & 0 & -\frac{6EI_x}{L^2} \\ 0 & 0 & \frac{12EI_y}{L^3} & 0 & \frac{6EI_y}{L^2} & 0 \\ 0 & 0 & 0 & \frac{GJ}{L} & 0 & 0 \\ 0 & 0 & \frac{6EI_y}{L^2} & 0 & \frac{4EI_y}{L} & 0 \\ 0 & -\frac{6EI_x}{L^2} & 0 & 0 & 0 & \frac{4EI_x}{L} \end{bmatrix}$$

$$M_{ii} = \rho AL \begin{bmatrix} \frac{1}{3} & 0 & 0 & 0 & 0 & 0 \\ 0 & \frac{13}{35} & 0 & 0 & 0 & \frac{11L}{210} \\ 0 & 0 & \frac{13}{35} & 0 & -\frac{11L}{210} & 0 \\ 0 & 0 & 0 & \frac{J}{3A} & 0 & 0 \\ 0 & 0 & -\frac{11L}{210} & 0 & \frac{L^2}{105} & 0 \\ 0 & \frac{11L}{210} & 0 & 0 & 0 & \frac{L^2}{105} \end{bmatrix}$$

$$M_{ij} = \rho AL \begin{bmatrix} \frac{1}{6} & 0 & 0 & 0 & 0 & 0 \\ 0 & \frac{9}{70} & 0 & 0 & 0 & \frac{13L}{420} \\ 0 & 0 & \frac{9}{70} & 0 & -\frac{13L}{420} & 0 \\ 0 & 0 & 0 & \frac{J}{6A} & 0 & 0 \\ 0 & 0 & \frac{13L}{420} & 0 & -\frac{L^2}{140} & 0 \\ 0 & -\frac{13L}{420} & 0 & 0 & 0 & -\frac{L^2}{140} \end{bmatrix}$$

$$M_{jj} = \rho AL \begin{bmatrix} \frac{1}{3} & 0 & 0 & 0 & 0 & 0 \\ 0 & \frac{13}{35} & 0 & 0 & 0 & -\frac{11L}{210} \\ 0 & 0 & \frac{13}{35} & 0 & \frac{11L}{210} & 0 \\ 0 & 0 & 0 & \frac{J}{3A} & 0 & 0 \\ 0 & 0 & \frac{11L}{210} & 0 & \frac{L^2}{105} & 0 \\ 0 & -\frac{11L}{210} & 0 & 0 & 0 & \frac{L^2}{105} \end{bmatrix} \quad (3.4)$$

where L denotes the initial length of a $C-C$ bond and equals to 0.1421 nm. In addition, for the computational model, numerical values of the following stiffness parameters should be given a priori: A is the cross-sectional area, E and G are respectively the Young's and shear moduli, I and J are respectively the moment of inertia and polar moment of inertia of the cross section and ρ is the beam element density.

Note that the consistent mass matrix formulation does not neglect the effects of rotational degrees-of-freedom (DOF). On the other hand, neglecting these rotational DOF yield singularity in time integration of associated dynamic equations unless special measures are taken; thus, although the effects of rotational DOF are very small, they are considered in all subsequent analyses.

2-D Euler-Bernoulli beam element having three nodal DOF such as two translational DOF in the x - and y - directions and a rotational DOF about the z - axis. This element is designed to resist axial and bending deformations.

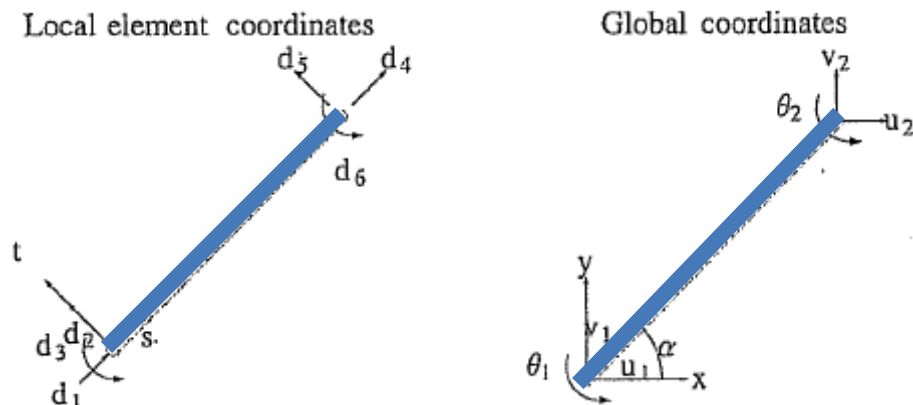


Figure 3.4 Local and global DOF of the 2-D EB element [124].

Figure 3.4 shows the local and global coordinate systems of a planar EB beam element. The local s axis is along the element axis and t axis is aligned 90° counterclockwise from the s axis. The nodal DOF in local coordinate system for a planar EB beam element are defined as follows

d_1, d_2 Displacements at node 1

d_3 Rotation at node 1

d_4, d_5 Displacements at node 2

d_6 Rotation at node 2

In global x and y coordinate system, the nodal displacements and rotations are defined for a planar beam element as follows

u_1, v_1 x and y displacements at node 1

θ_1 Rotation about z axis at node 1

u_2, v_2 x and y displacements at node 2

θ_2 Rotation about z - axis at node 2

The transformation between the global and local DOF can be written for a planar EB beam element as follows

$$\begin{pmatrix} d_1 \\ d_2 \\ d_3 \\ d_4 \\ d_5 \\ d_6 \end{pmatrix} = \begin{bmatrix} l_s & m_s & 0 & 0 & 0 & 0 \\ -m_s & l_s & 0 & 0 & 0 & 0 \\ 0 & 0 & 1 & 0 & 0 & 0 \\ 0 & 0 & 0 & l_s & m_s & 0 \\ 0 & 0 & 0 & -m_s & l_s & 0 \\ 0 & 0 & 0 & 0 & 0 & 1 \end{bmatrix} \begin{pmatrix} u_1 \\ v_1 \\ \theta_1 \\ u_2 \\ v_2 \\ \theta_2 \end{pmatrix} \quad (3.5)$$

where

$$l_s = \cos \alpha = \frac{x_2 - x_1}{L} \quad (3.6)$$

$$m_s = \sin \alpha = \frac{y_2 - y_1}{L} \quad (3.7)$$

$$L = \sqrt{(x_2 - x_1)^2 + (y_2 - y_1)^2} \quad (3.8)$$

where α is the angle between the local s axis and global x axis measured counterclockwise, (x_1, y_1) and (x_2, y_2) are the coordinates of the two nodes at the EB beam element ends, and L is the length of the EB element. Equation (3.5) can be written as

$$\mathbf{d}_l = \mathbf{T}_{2D} \mathbf{d} \quad (3.9)$$

$$\mathbf{d}_l = \begin{bmatrix} d_1 & d_2 & d_3 & d_4 & d_5 & d_6 \end{bmatrix}^T \quad (3.10)$$

$$\mathbf{T}_{2D} = \begin{bmatrix} l_s & m_s & 0 & 0 & 0 & 0 \\ -m_s & l_s & 0 & 0 & 0 & 0 \\ 0 & 0 & 1 & 0 & 0 & 0 \\ 0 & 0 & 0 & l_s & m_s & 0 \\ 0 & 0 & 0 & -m_s & l_s & 0 \\ 0 & 0 & 0 & 0 & 0 & 1 \end{bmatrix} \quad (3.11)$$

$$\mathbf{d} = \begin{bmatrix} d_1 & v_1 & \theta_1 & u_2 & v_2 & \theta_2 \end{bmatrix}^T \quad (3.12)$$

3-D Euler-Bernoulli beam element has six nodal DOF per node; translations in the nodal x , y and z directions and rotations about the nodal x , y and z axes. This element is an extension of the 2-D beam element to 3-D. This element is designed to resist axial, bending and torsional deformations. Figure 3.5 shows the local coordinate system of a 3-D EB beam element. The local t -axis runs along the centroidal axis of the EB element. The local s - and r -axes are the principal moment of inertia axes for the cross section.

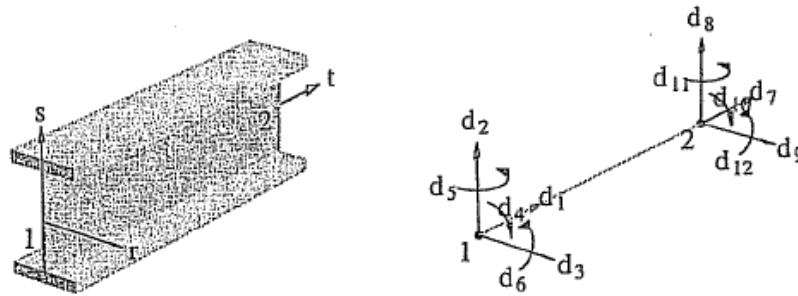


Figure 3.5 Local DOF of the 3-D EB element [124].

The nodal DOF in local coordinate system for a 3-D EB beam element are defined as follows

d_1, d_2, d_3 Displacements at node 1

d_4, d_5, d_6 Rotation at node 1

d_7, d_8, d_9 Displacements at node 2

d_{10}, d_{11}, d_{12} Rotation at node 2

In global x, y and z coordinate system, the nodal displacements and rotations are defined for a 3-D beam element as follows

u_1, v_1, w_1 x, y and z displacements at node 1

$\theta_{x1}, \theta_{y1}, \theta_{z1}$ Rotations about z axis at node 1

u_2, v_2, w_2 x, y and z displacements at node 2

$\theta_{x2}, \theta_{y2}, \theta_{z2}$ Rotations about z axis at node 2

The transformation between the global and local DOF can be written for a 3-D EB beam element as follows

$$\begin{pmatrix} d_1 \\ d_2 \\ d_3 \\ d_4 \\ d_5 \\ d_6 \\ d_7 \\ d_8 \\ d_9 \\ d_{10} \\ d_{11} \\ d_{12} \end{pmatrix} = \begin{bmatrix} \mathbf{H} & \mathbf{0} & \mathbf{0} & \mathbf{0} \\ \mathbf{0} & \mathbf{H} & \mathbf{0} & \mathbf{0} \\ \mathbf{0} & \mathbf{0} & \mathbf{H} & \mathbf{0} \\ \mathbf{0} & \mathbf{0} & \mathbf{0} & \mathbf{H} \end{bmatrix} \begin{pmatrix} u_1 \\ v_1 \\ w_1 \\ \theta_{x1} \\ \theta_{y1} \\ \theta_{z1} \\ u_2 \\ v_2 \\ w_2 \\ \theta_{x2} \\ \theta_{y2} \\ \theta_{z2} \end{pmatrix} \quad (3.13)$$

Equation (3.13) can be written as

$$\mathbf{d}_l = \mathbf{T}_{3D} \mathbf{d} \quad (3.14)$$

$$\mathbf{d}_l = \begin{bmatrix} d_1 & d_2 & d_3 & d_4 & d_5 & d_6 & d_7 & d_8 & d_9 & d_{10} & d_{11} & d_{12} \end{bmatrix}^T \quad (3.15)$$

$$\mathbf{T}_{3D} = \begin{bmatrix} \mathbf{H} & \mathbf{0} & \mathbf{0} & \mathbf{0} \\ \mathbf{0} & \mathbf{H} & \mathbf{0} & \mathbf{0} \\ \mathbf{0} & \mathbf{0} & \mathbf{H} & \mathbf{0} \\ \mathbf{0} & \mathbf{0} & \mathbf{0} & \mathbf{H} \end{bmatrix} \quad (3.16)$$

$$\mathbf{d} = \begin{bmatrix} v_1 & w_1 & \theta_{x1} & \theta_{y1} & \theta_{z1} & u_2 & v_2 & w_2 & \theta_{x2} & \theta_{y2} & \theta_{z2} \end{bmatrix}^T \quad (3.17)$$

where \mathbf{H} is the 3×3 rotation matrix and $\mathbf{0}$ is a 3×3 zero matrix. Thus, the complete transformation matrix \mathbf{T}_{3D} is a 12×12 matrix. The rotation matrix \mathbf{H} transforms a vector quantity from the local coordinate system to the global one. The components of a vector along the local s , t and r coordinates simply the sum of projections of its x , y and z components along the local axes. In matrix form, the transformation can be written as follows

$$\begin{pmatrix} t \\ s \\ r \end{pmatrix} = \begin{bmatrix} l_t & m_t & n_t \\ l_s & m_s & n_s \\ l_r & m_r & n_r \end{bmatrix} \begin{pmatrix} x \\ y \\ z \end{pmatrix} \quad (3.18)$$

$$\mathbf{H} = \begin{bmatrix} l_t & m_t & n_t \\ l_s & m_s & n_s \\ l_r & m_r & n_r \end{bmatrix} \quad (3.19)$$

where l_t is the cosine of the angle between the t and x axes; m_t is the cosine of the angle between the t and y axes; n_t is the cosine of the angle between the t and z axes; l_s is the cosine of the angle between the s and x axes; m_s is the cosine of the angle between the s and y axes; n_s is the cosine of the angle between the s and z axes; l_r is the cosine of the angle between the r and x axes; m_r is the cosine of the angle between the r and y axes; n_r is the cosine of the angle between the r and z axes.

The stiffness matrix in the local coordinate system can be related to those in the global coordinate system for 2-D or 3-D beam elements as follows

$$\mathbf{K} = \mathbf{T}^T \mathbf{K}_l \mathbf{T} \quad (3.20)$$

where \mathbf{K} is the global element stiffness matrix of the EB beam element; \mathbf{K}_l is the local element stiffness matrix of the EB beam element (i.e., Equations 3.1 and 3.4). In addition, by using the transformation matrix \mathbf{T} , the mass matrix in the global coordinate system is obtained as follows

$$\mathbf{M} = \mathbf{T}^T \mathbf{M}_l \mathbf{T} \quad (3.21)$$

where \mathbf{M} is the global element mass matrix of the EB beam element; \mathbf{M}_l is the local element mass matrix of the EB beam element (i.e., Equations 3.2 and 3.4).

3.2 Solution Procedure For Small Deformation Static Problems

After the assembly procedure, the global system of equations consists of n equations in n unknowns for small deformation static analyses

$$\mathbf{K}_{glob} \mathbf{d} = \mathbf{F} \quad (3.22)$$

where \mathbf{K}_{glob} is the global stiffness matrix, \mathbf{F} is the vector of applied force and \mathbf{d} is the displacement vector. After the application of boundary conditions, solutions for global nodal unknowns follow the standard FE procedure. For computing the element solution, the global DOF for each element are first transformed into the local DOF by multiplying them by the transformation matrix \mathbf{T} for the element.

For the computational models, numerical values of the following parameters should be given a priori: E , G , A , I , J and ρ . To obtain these parameters energy equivalence concept is employed. This concept is summarized in the following sections.

3.3 Application of Atomistic Modeling Approach

To obtain geometric and material properties of the beam elements, energy equivalence concept is employed. In this analogy, stretching, bending and twisting potential energy terms based on the MM and structural mechanic models are assumed to be independent of each other and then corresponding terms are set equal

to each other in these two models. In graphite structures, bonded such as the covalent bond and non-bonded such as van der Waals and electrostatic forces interactions are generally taken into account. Comparing the bonded interaction, non-bonded interactions have less contribution on the mechanical characteristics of carbon based structures. As a result, the general expression of the total potential energy of the force field in the MM model can be expressed as the sum of energies of bonded interactions [33, 34]

$$U_{total} = \sum U_r + \sum U_\theta + \sum U_\phi + \sum U_\omega \quad (3.23)$$

where U_r is the potential energy for bond stretching, U_θ for bond angle bending, U_ϕ for a dihedral angle torsion and U_ω for out-of-plane torsion. Nonetheless, U_ϕ and U_ω terms can be merged into a single term. Figure 3.6 shows the different types of MM potential energies.

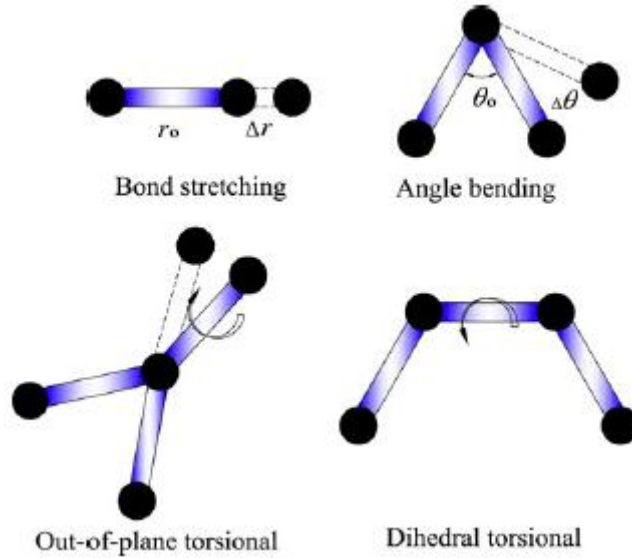


Figure 3.6: Potential energies in MMs [38].

Under the small deformation assumption, the following simple harmonic expressions of potential energy components are adequate for describing the total potential energy [34]

$$U_r = \frac{1}{2} k_r (\Delta r)^2 \quad (3.24)$$

$$U_{\theta} = \frac{1}{2} k_{\theta} (\Delta\theta)^2 \quad (3.25)$$

$$U_{\tau} = U_{\phi} + U_{\omega} = \frac{1}{2} k_{\tau} (\Delta\phi)^2 \quad (3.26)$$

where k_r , k_{θ} and k_{τ} respectively denote the bond stretching, angle bending and torsional force constant and the symbols Δr , $\Delta\theta$ and $\Delta\phi$ represent the bond stretching increment, bond angle change and twisting angle change, respectively. In this study, the AMBER force model is chosen [33, 34]. The AMBER force model constants k_r , k_{θ} and k_{τ} are taken as $6.52 \times 10^{-7} \text{ N nm}^{-1}$, $8.76 \times 10^{-10} \text{ N nm rad}^{-2}$ and $2.78 \times 10^{-10} \text{ N nm rad}^{-2}$ respectively.

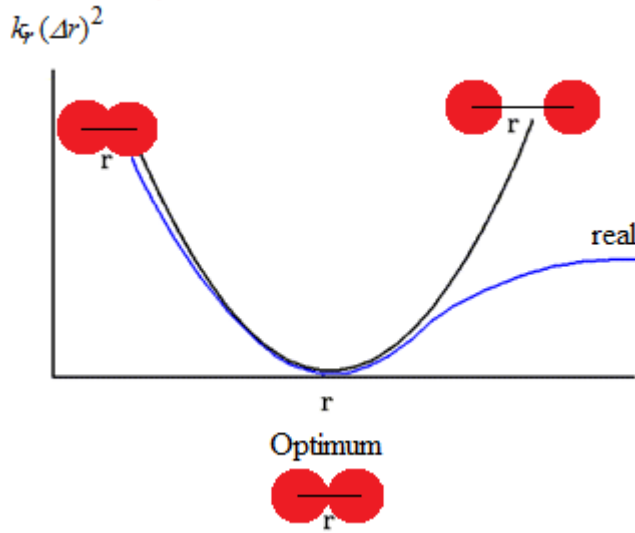


Figure 3.7: Bond stretching energy in MMs.

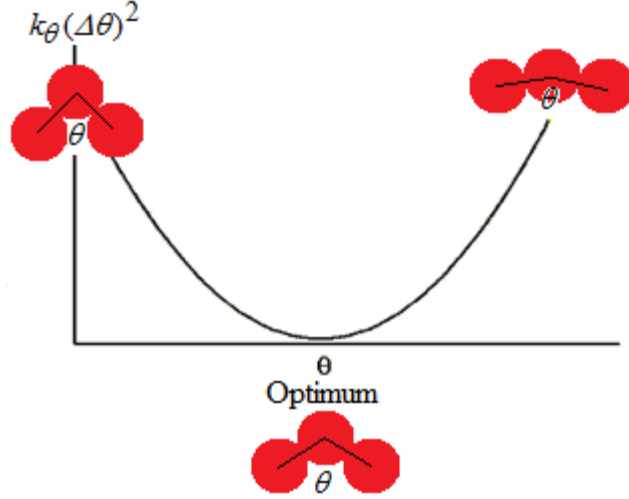


Figure 3.8: Angle bending energy in MMs.

There are two approaches to model interatomic behavior by the use of beam elements such as the model proposed by Li and Chou [34] that neglects the shear deformation effect and the model proposed by Scarpa and Adhikari [49] that considers the shear deformation effect.

Following the approach of Li and Chou [34], the strain energy of a uniform beam due to pure tension, bending and torsion can be written as

$$U_A = \frac{1}{2} \frac{EA}{L} (\Delta L)^2 \quad (3.27)$$

$$U_B = \frac{1}{2} \frac{EI}{L} (2\alpha)^2 \quad (3.28)$$

$$U_T = \frac{1}{2} \frac{GJ}{L} (\Delta\beta)^2 \quad (3.29)$$

where U_A , U_B and U_T are respectively axial, bending and torsion strain energies, L is the length of the beam element, A is the cross-sectional area, E and G are respectively Young's and shear moduli, I and J are respectively the moment of inertia and polar moment of inertia of the cross section, ΔL is the axial stretching deformation, α is the rotational angle at the ends of the beam element, and $\Delta\beta$ is the relative rotation between the two ends of the beam element. According to structural mechanics, Figure 3.9 shows the potential energies of a beam.

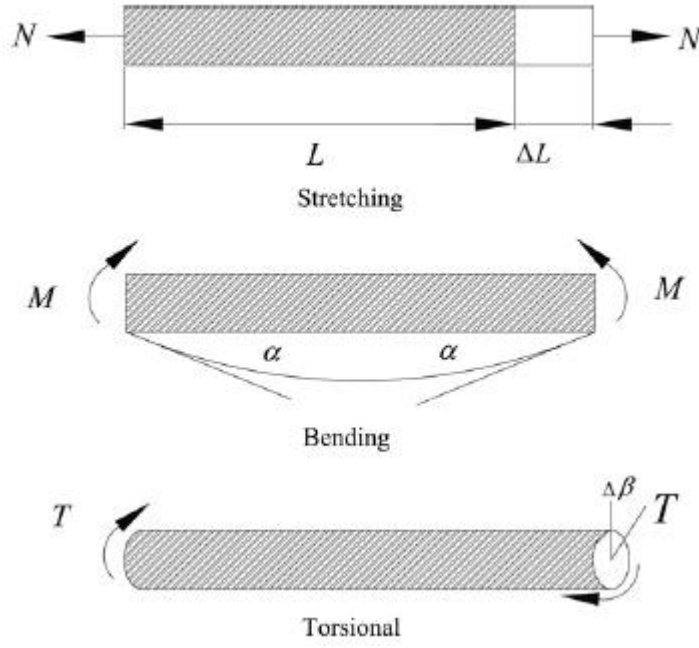


Figure 3.9: Potential energies in structural mechanics [38].

Using the equivalency of the corresponding terms in potential energy components of the MM and CM models, the following relations are obtained [34]

$$\frac{EA}{L} = k_r, \frac{EI}{L} = k_\theta, \frac{GJ}{L} = k_\tau \quad (3.30)$$

Assuming that the cross section of beam elements is uniform and circular, then the Young's modulus E , the shear modulus G and diameter of the cross section d are obtained by plugging in the cross sectional area $A = \pi d^2 / 4$, moment of inertia $I = \pi d^4 / 64$ and polar moment of inertia $J = \pi d^4 / 32$ as follows [37]

$$E = \frac{k_r^2 L}{4\pi k_\theta}, \quad G = \frac{k_r^2 k_\tau L}{8\pi k_\theta^2}, \quad d = 4 \sqrt{\frac{k_\theta}{k_r}} \quad (3.31)$$

Table 3.1 summarizes the geometric and material properties of the beam element which are the inputs to the FE models.

Table 3.1: Geometric and material properties of beam elements.

	Present work	Scarpa and Adhikari [49]
Thickness, d	1.47 \AA	0.84 \AA
Elastic modulus, E	$5.488 \times 10^{-8} \text{ N/\AA}^2$	$16.71 \times 10^{-8} \text{ N/\AA}^2$
Shear modulus, G	$8.711 \times 10^{-9} \text{ N/\AA}^2$	$80.8 \times 10^{-9} \text{ N/\AA}^2$

On the other hand, Scarpa and Adhikari [49] proposed a beam model considering the shear deformation effects where, instead of Equation (3.25), the following bending strain energy expression is suggested

$$U_B = \frac{1}{2} \frac{EI}{L} \frac{(4 + \Phi)}{(1 + \Phi)} (2\alpha)^2 \quad (3.32)$$

where Φ is the shear deformation constant defined by

$$\Phi = \frac{12EI}{GA_s L^2} \quad (3.33)$$

where $A_s = A/F_s$, and F_s is the shear correction factor given by

$$F_s = \frac{6(1 + \nu)}{7 + 6\nu} \quad (3.34)$$

where ν is the Poisson's ratio of the beam element. By equating the Equations (3.24) and (3.26) to Equations (3.27) and (3.29) respectively, expressions for E and G are obtained. Then, by plugging-in the expressions of E and G together with the Equation (3.34) into the Equation (3.33), the shear deformation constant is found as follows

$$\Phi = \frac{9\pi^2 k_r d^4 (1 + \nu)}{16L^2 \pi^2 k_\tau (7 + 6\nu)} \quad (3.35)$$

After substituting the Equation (3.35) into the Equation (3.32) which is then equated with the Equation (3.25), the resulting equation is minimized to obtain ν and d that are used to calculate E and G . In sum, the thickness, Young's modulus and shear modulus of the beam element representing the interatomic bond are listed in Table 3.1 [49].

Both of the beam models proposed by Li and Chou [34] and Scarpa and Adhikari [49] employ identical axial and torsion strain energy expressions, but they approximate the bending strain energy term by using different approaches. The strain energy term of Li and Chou [34] (i.e., given by the Equations (3.33) to (3.35)) and the strain energy term of Scarpa and Adhikari [49] (i.e., given by Equations (3.33), (3.35) and (3.38)) give the same AMBER force model constants (

$$k_r = 6.52 \times 10^{-7} \text{ Nnm}^{-1}, k_\theta = 8.76 \times 10^{-10} \text{ Nnmrad}^{-2} \text{ and } k_\tau = 2.78 \times 10^{-10} \text{ Nnmrad}^{-2})$$

when the data set given in Table 3.1 are employed. On the other hand, the deformation in graphene and graphitic layers are due to hinging-stretching mechanism [49] and hinging creates shear stresses. Nonetheless, our aim is to represent the potential energy of interatomic bonds and the beam model proposed by Li and Chou [34] can exactly represent this potential energy of interatomic bonds. Consequently, even though the beam model proposed by Li and Chou [34] neglects the shear deformation effect which is valid for slender beams. As long as its spring constant is equal to the corresponding AMBER force model constants, it will yield correct deformation results. Subsequently, the analyses are carried out by using the beam model of Li and Chou [34] due to its simplicity. In addition, the Poisson's ratio is not needed to construct equivalent FE formulation [34], and E , G , d and L values are sufficient to set up the FE model.

If small deformation assumption exists, both of the models in Li and Chou [34] and Scarpa and Adhikari [49] are sufficient to determine the behavior of an atomic bond. However, this assumption is not adequate for failure analysis which should be analyzed as a large deformation problem and geometric nonlinear effects have to be considered. For large deformation problems, shear beam element (i.e., Timoshenko beam element) is not preferred since it is more difficult to be adapted for the modified Morse potential energy terms than the EB beam element. To this end, the modified Morse potential along with an iterative solution procedure is used for large deformation problems in this thesis. Implementation of this pairwise potential function is very easy in comparison with some other multibody potentials such as Brenner potential function whose some applications can be found in literature [72, 85-95].

Under the uniaxial loading and small strain hypothesis [33, 90, 92-94], the atomistic interaction is mainly governed by the bond stretching and bond angle bending terms.

As a result, according to the modified Morse potential, the potential energy can be expressed as

$$U_{total} = \sum U_r + \sum U_\theta \quad (3.36)$$

$$U_r = D_e \left\{ \left[1 - e^{-\beta(r-r_0)} \right]^2 - 1 \right\} \quad (3.37)$$

$$U_\theta = \frac{1}{2} k_\theta (\theta - \theta_0)^2 + \left[k_{sextic} (\theta - \theta_0)^4 \right] \quad (3.38)$$

where U_r is the bond energy due to bond stretching, U_θ is the bond energy due to angle bending, r and θ are the current bond length and current angle of the adjacent bonds, respectively.

Table 3.2. Modified Morse potential parameters [72].

r_0	1.421 Å	θ_0	2.094 rad
β	2.625 Å^{-1}	k_θ	$0.9 \times 10^{-8} \text{ NÅ/rad}^2$
D_e	$6.03105 \times 10^{-9} \text{ NÅ}$	k_{sextic}	0.754 Å^4

Values of the parameters in the modified Morse potential functions are the same as those in [72] and listed in Table 3.2. Figure 3.10 shows the tensile energy –strain curve of the modified Morse potential.

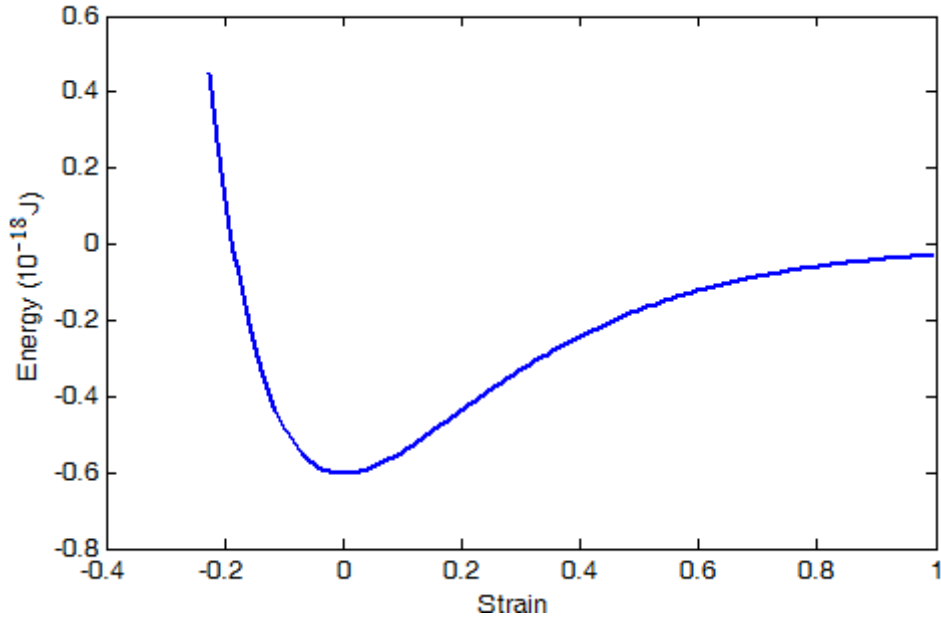


Figure 3.10: Tensile energy-strain curve of the modified Morse potential.

The multiple layers of CNTs are held together thorough Van der Waals forces. The Van der Waals force is a non-bonded interaction, and it can be an attraction force or a repulsion force. These interactions are often modeled using the general Lennard-Jones (LJ) potential. The general LJ potential is commonly expressed as

$$U(r) = 4\varepsilon \left[\left(\frac{\sigma}{r} \right)^{12} - \left(\frac{\sigma}{r} \right)^6 \right] \quad (3.39)$$

where, r is the distance between inreacting atoms, ε and σ are the LJ parameters. For carbon atoms, the LJ parameters are $\varepsilon=0.0556$ kcal/mole and $\sigma=3.4$ Å [125]. The potential $U(r)$ is usully truncated at an interatomic distance of 2.5σ without a significant loss of accuracy. Based on the LJ potential, the Van der Waals force between interacting atoms can be written as follows

$$F(r) = -\frac{dU(r)}{dr} = 24 \frac{\varepsilon}{\sigma} \left[2 \left(\frac{\sigma}{r} \right)^{13} - \left(\frac{\sigma}{r} \right)^7 \right] \quad (3.40)$$

The variations of the LJ potential and Van der Waals force with the distance between two interacting atoms are shown in Figure 3.11.

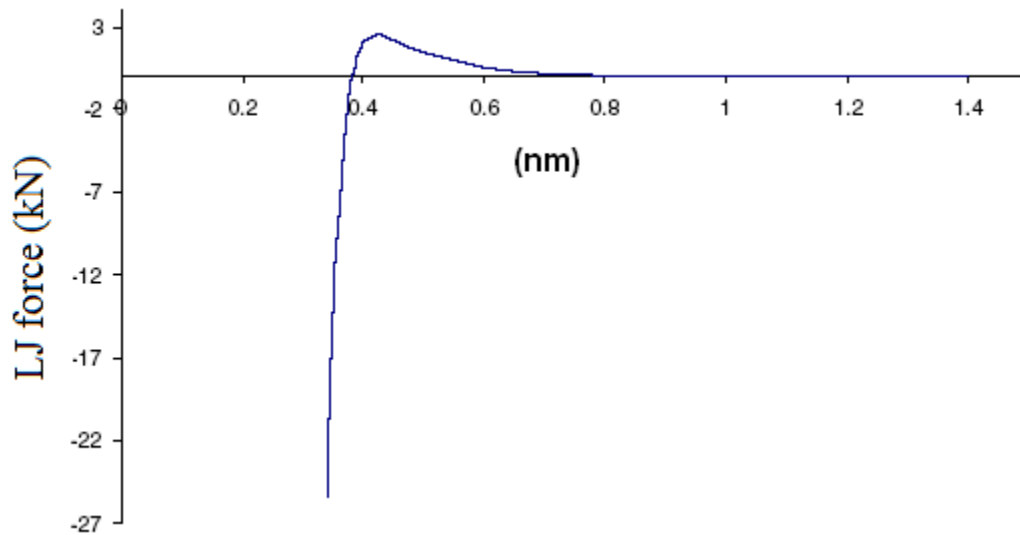


Figure 3.11: Van der Waals force as the distance between two interacting atoms changes.

Tersoff-Brenner many body interatomic potential for carbon [126-127], which is widely used in the study of carbon base nanostructures, is introduced as follows

$$V(r_{ij}) = V_R(r_{ij}) - B_{ij} V_A(r_{ij}) \quad (3.41)$$

For atoms i and j , where r_{ij} is the distance between atoms i and j , V_R and V_A are the repulsive and attractive pair terms given by

$$V_A(r) = \frac{S D^{(e)}}{S-1} e^{-\sqrt{\frac{2}{S}} \beta (r-R^{(e)})} f_c(r) \quad (3.42)$$

$$V_R(r) = \frac{D^{(e)}}{S-1} e^{-\sqrt{2S} \beta (r-R^{(e)})} f_c(r) \quad (3.43)$$

the parameters $D^{(e)}$, S , β , and $R^{(e)}$ are determined from the known physical properties of carbon, graphite and diamond. The function f_c is merely a smooth cutoff function to limit the range of the potential and is given by

$$f_c(r) = \begin{cases} 1 & r < R^{(1)}, \\ \frac{1}{2} \left\{ 1 + \cos \left[\frac{\pi(r-R^{(1)})}{R^{(2)}-R^{(1)}} \right] \right\} & R^{(1)} < r < R^{(2)}, \\ 0 & r > R^{(2)} \end{cases} \quad (3.44)$$

which is continuous and has a cutoff of $R^{(2)} = 0.2$ nm and $R^{(1)} = 0.17$ nm to include only the first-neighbor shell for carbon atoms. The parameter B_{ij} in Equation (3.41) represents a multi-body coupling between the bond from atom i to atom j and the local environment of atom i , and is given by

$$B_{ij} = \left[1 + \sum_{k(\neq i,j)} G(\theta_{ijk}) f_c(r_{ik}) \right]^{-\delta} \quad (3.45)$$

where r_{ik} is the distance between atoms i and k , f_c is the cutoff function in Equation (3.44), θ_{ijk} is the angle between bonds $i-j$ and $i-k$, and the function G is given by

$$G(\theta) = a_0 \left[1 + \frac{c_0^2}{d_0^2} - \frac{c_0^2}{d_0^2 + (1 + \cos \theta)^2} \right] \quad (3.46)$$

Values of the parameters are listed in Table 3.3.

Table 3.3: Tersoff- Brenner potential constants [127].

$D^{(e)}$	6.000 eV	δ	0.5
$R^{(e)}$	0.139 nm	a_0	0.00020813
S	1.22	c_0	330
β	21 n/m	d_0	3.5

Based on this set of parameters, the corresponding equilibrium bond length can be determined by

$$\frac{\partial V}{\partial r_{ij}} = 0 \quad (3.47)$$

4. CHARACTERIZATION, DYNAMIC AND FRACTURE ANALYSES OF GRAPHENE SHEETS (GSs)

In this section, an equivalent dynamic and nonlinear fracture model of SLGSs is developed by using the MM based FE approach where bond interactions are represented by EB beams; then, two- and three-dimensional modal, transient and nonlinear fracture analyses of SLGSs are completed. In order to observe vibrational characteristics of SLGSs, lumped mass matrix is generally used in literature, which is sufficient to determine vibrational characteristics of GSs and CNTs. As mass lumping by neglecting rotational inertia of beam elements causes singularity problems in transient analysis, consistent mass matrices (e.g., Equations 3.2 and 3.4) are used in FE models in this thesis. An equivalent density parameter for the beam elements is derived by using the equivalency of natural frequencies of the MM model and continuum plane-stress FE model. The Newmark method is employed to integrate the associated equations of transient analyses [128].

An atomistic based FE model for prediction of fracture behavior of SLGSs is developed by considering large deformation and nonlinear geometric effects. The non-linear characteristic of beam elements are obtained by using the modified Morse potential. Formulation underlying the proposed approach is applied to defect-free, and Stone-Wales (SW) and one atom vacancy defected zigzag and armchair SLGSs [129].

4.1. Equivalent FE Models, Characterization and Vibration Analyses of SLGSs

As mentioned above, equivalent E and ν values of the CM model for SLGSs are calculated by simulating a test specimen under uni-axial tension. The MM model of zigzag type SLGSs has the dimension of $81.22 \text{ \AA} \times 126.46 \text{ \AA}$ having 4020 atoms and 5937 bonds. The equivalent CM plane-stress model has the same dimension of the MM model and it has 486 nodes and 442 quadrilateral elements. Figure 4.1 shows the MM model and equivalent continuum plane stress model of the SLGS. All of the static, vibrations and dynamic computations of the MM model are completed

by using a computer code developed in MATLAB environment and the results on vibration analyses are verified by using Ansys ® software where the analyses of 2-D and 3-D MM and CM models are performed by using Plane42, Shell63, Beam3, Beam4, Mass21 type elements. In the MATLAB code, the analyses by using the 2-D and 3-D CM models are completed by using plane-stress and shell elements, respectively.

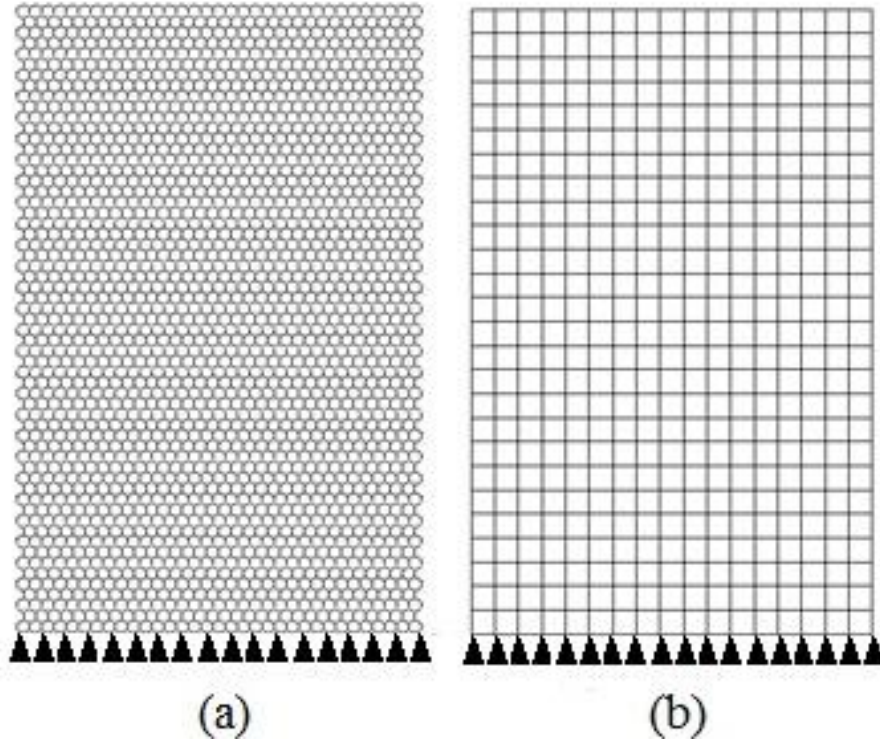


Figure 4.1: (a) Molecular and (b) equivalent plane stress FE models on which boundary conditions are shown.

To calculate Young's modulus E and Poisson's ratio ν , symmetry boundary conditions are applied to all the nodes on one edge and the nodes on the opposite edge are uniformly loaded. All load vector calculations are based on consistent load formulations and equivalent Young's modulus and Poisson's ratio are found as follows

$$E = \frac{\sigma}{\varepsilon} = \frac{F/A_0}{\Delta a/a} \quad (4.1)$$

$$\nu = -\frac{\Delta b/b}{\Delta a/a} \quad (4.2)$$

where F is the total applied force on the atoms at one end of the graphene sheet, A_0 is the cross-sectional area which is equal to bt (where b and t are the width and thickness of the sheet, respectively), a is the initial sheet length, Δa and Δb are respectively changes in the width and length of the SLGS. In all calculations, the nominal thickness of 0.34 nm is used for the SLGS. Table 4.1 lists values of tensile rigidity Y , Poisson's ratio ν and nominal thickness t of monolayer graphene in literature and found in our simulations. Note that there is a lack of experimental studies on the values of Poisson's ratio ν in literature and numerical results on Poisson's ratio are scattered in a wide range. Sakhaee-Pour [38] calculated the shear modulus and Poisson's ratio of SLGSs by using the shear test (that is, a tangential force is applied to all the nodes on one edge and the opposite edge is constrained). It is observed that such a numerical test does not reflect the exact shear behavior of SLGSs since the conditions of pure shear test could not be created and additional bending load is applied to the specimen. Such a simulation may result in the Poisson's ratio which is much larger than 0.5.

Table 4.1. Graphene data from literature and present work.

Reported by	Y (TPa nm)	Poisson's ratio	t (nm)	Method
Sakhaee-Pour [38]	0.337-0.354	1.129-1.441	0.34	Beam analogy
Li and Chou [34]	0.338-0.351	-	0.34	Beam analogy
Lee <i>et al.</i> [21]	0.335	-	0.335	Experimental
Present work	0.352	0.063	0.34	Beam analogy

Equivalent density parameter for the beam elements in the MM model is obtained by using the equivalency of natural frequencies of continuum plane stress FE model and those of the MM model. To this end, firstly natural frequencies of continuum plane stress model are obtained where density of continuum plane stress model is equal to density of graphite which is 2260 kg/m³; then, equivalent density parameter of the beam elements is calculated. After assembling the element stiffness and mass matrices, the natural frequencies and corresponding mode shapes are obtained by solving the following eigenproblem

$$(\mathbf{K} - \omega_i^2 \mathbf{M})\mathbf{d} = \mathbf{0} \quad (4.3)$$

where \mathbf{K} , \mathbf{M} , \mathbf{d} and ω_i are the global stiffness matrix, global mass matrix, displacement vector and the natural frequencies, respectively. In addition, the natural frequency is equal to $\omega=2\pi f$, where f has the unit of Hertz. In numerical solutions, free-fixed and free-free boundary conditions are taken into account. For free-fixed case, all the nodes on one edge are fully constrained and the nodes on the opposite edge are free (e.g., see Figure 4.1).

Table 4.2. Values of equivalent beam density ρ of Euler-Bernoulli beam elements.

Researcher	Equivalent beam density ρ kg/m ³	Method
Lee and Lee [43]	2300	Beam analogy
Mir et al [61]	2300	Beam analogy
Present work	5500	Beam analogy

Following the above mentioned procedure, Table 4.2 lists the values of equivalent density parameter ρ of beam elements assumed in literature and found in our study. Table 4.3 and Table 4.4 show the numerical results obtained by using the MM and shell models for in-plane and 3-D cases, where the first six natural frequencies obtained for free-free and free-fixed boundary conditions are given. Figure 4.2 shows the first three free-fixed in-plane deformation mode shapes of the lumped mass MM model, plane stress CM model and consistent mass MM model. Note also that the other mode shapes are found to be similar. Figure 4.3 shows the first three free-fixed 3-D deformation mode shapes of the lumped mass MM model, shell CM model and consistent mass MM model. In addition, the natural frequencies of the 3-D MM model are in good agreement with the results presented in literature [39].

Table 4.3: First six fundamental frequencies of 2-D SLGS (in GHz).

Model	Boundary conditions	1	2	3	4	5	6
Plane stress model	free-free	623.0	845.9	903.4	1167.7	1188.8	1323.1
Consistent mass matrix beam model	free-free	617.6	846.6	903.4	1178.4	1205.0	1333.1
Lumped mass matrix beam model	free-free	605.8	836.8	891.5	1149.7	1174.5	1314.1
Plane stress model	free-fixed	142.2	423.3	492.4	1001.9	1176.8	1178.8
Consistent mass matrix beam model	free-fixed	142.0	424.8	492.4	1002.7	1179.7	1194.4
Lumped mass matrix beam model	free-fixed	140.3	421.0	486.1	990.2	1163.8	1165.0

Table 4.4: First six fundamental frequencies of 3-D SLGS (in GHz).

Model	Boundary conditions	1	2	3	4	5	6
Consistent mass matrix beam model	free-free	13.8	14.5	31.9	37.0	39.4	48.2
Lumped mass matrix beam model	free-free	13.5	14.2	31.1	36.2	38.6	47.1
Shell model <u>divided by the thickness</u>	free-free	13.7	14.6	32.3	33.3	37.9	44.5
Consistent mass matrix beam model	free-fixed	2.37	8.03	14.6	27.0	38.5	43.1
Lumped mass matrix beam model	free-fixed	2.34	7.88	14.5	26.5	37.9	42.4
Shell model <u>divided by the thickness</u>	free-fixed	2.16	8.32	13.5	27.2	36.7	38.0

Note that unlike the results on in-plane MM and CM plane-stress models, there is a discrepancy between the calculated natural frequencies of the 3-D MM model and those of the 3-D shell model. If the natural frequencies of the 3-D shell model are divided by the thickness value, they are in close agreement with those of the 3-D MM model, which are shown in Table 4.4 for the free-free and free-fixed boundary conditions. Nonetheless, while the transient and static displacement solutions of the in-plane MM model and those of the plane-stress CM model match well, the transient and static out-of-plane displacements for the 3-D MM and CM shell models do not agree. This is originating from the fact that the out-of-plane bending rigidity of the 3-D CM shell model is in error that is already reported by other researchers [33, 40]; hence, corrections for the thickness value of the 3-D CM shell model are suggested in literature. Studies on this issue have been continuing. It is concluded that the proposed approach can compute the natural frequencies of SLGSs in high accuracy and employment of consistent mass matrix in FE model improves accuracy.

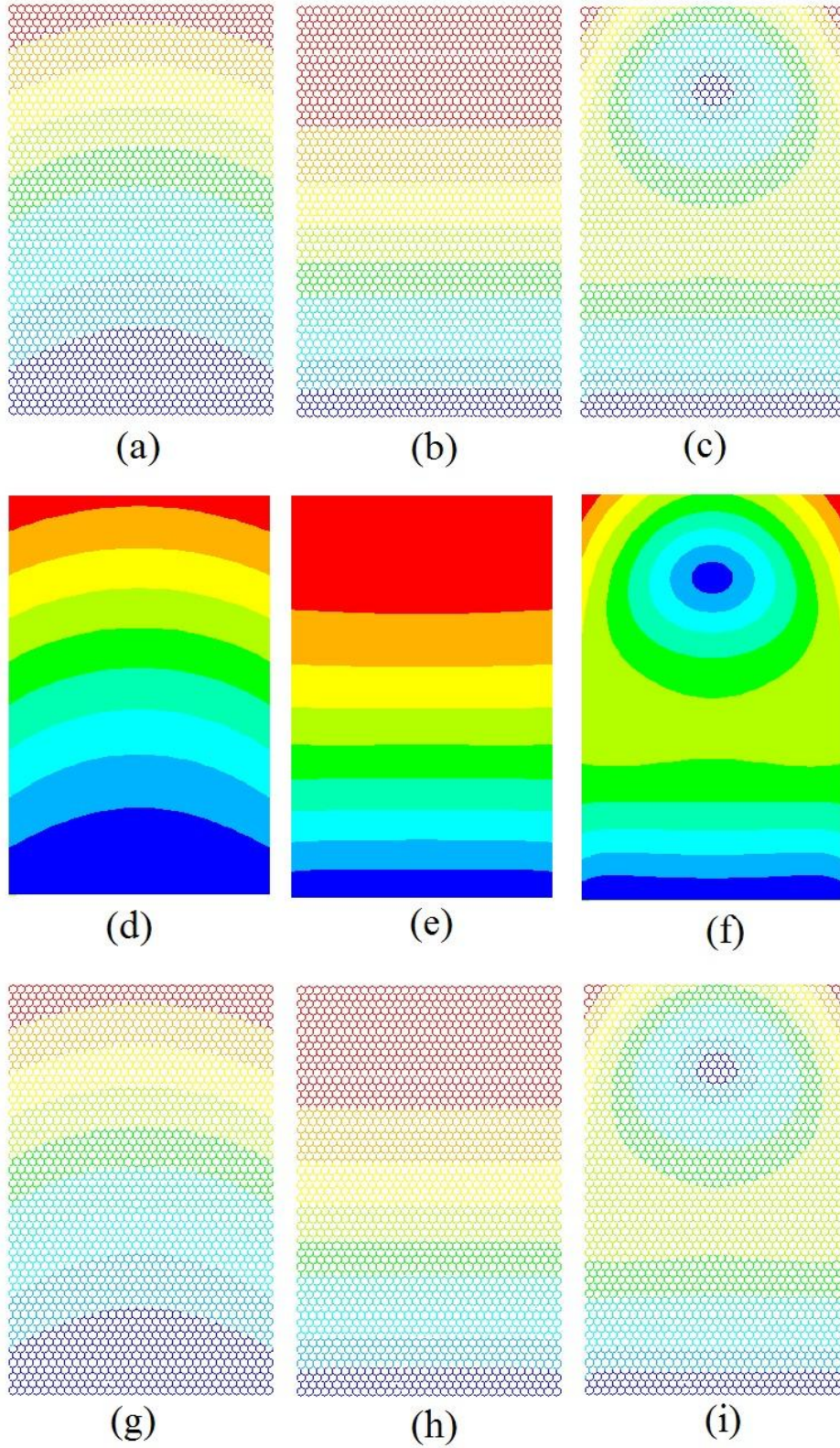


Figure 4.2: The first three in-plane mode shapes of the lumped mass MM model (a)-(c), plane stress CM model (d)-(f) and consistent mass MM model (g)-(i) where the boundary conditions are free-fixed.

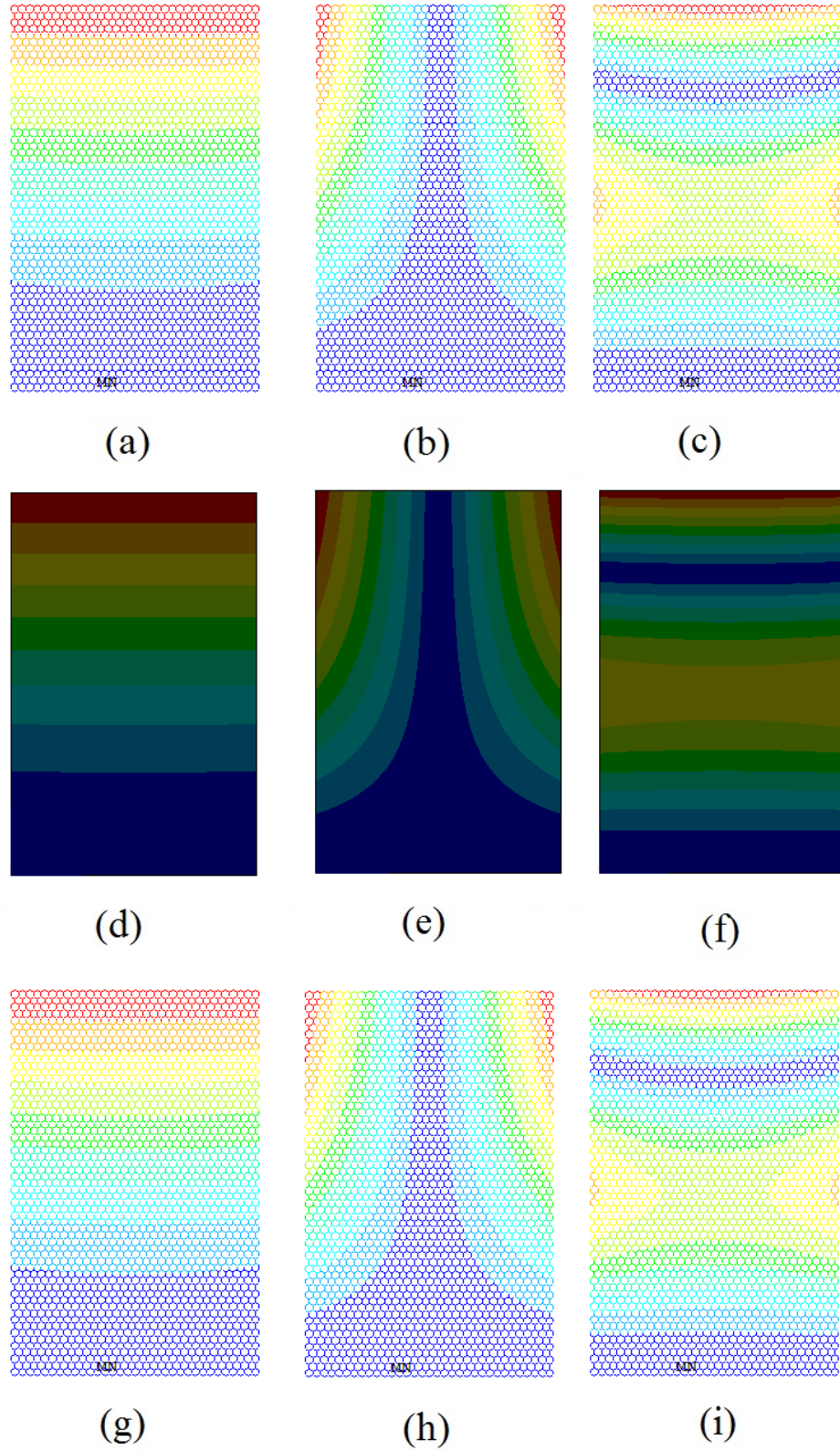


Figure 4.3: The first three 3-D mode shapes of the lumped mass MM model (a)-(c), shell CM model (d)-(f) and consistent mass MM model (g)-(i) where the boundary conditions are free-fixed.

4.2. Dynamic Analyses of SLGSs

2-D and 3-D transient behaviors of SLGSs are studied by employing the atomistic modeling approaches presented in Section 3. According to the theory of structural dynamics, the semidiscrete equation of motion for a damped structure is written as

$$\mathbf{M}\ddot{\mathbf{d}} + \mathbf{C}\dot{\mathbf{d}} + \mathbf{K}\mathbf{d} = \mathbf{F} \quad (4.4)$$

where \mathbf{M} is the mass matrix, \mathbf{C} is the viscous damping matrix, \mathbf{K} is the stiffness matrix, \mathbf{F} is the vector of applied force, and \mathbf{d} , $\dot{\mathbf{d}}$ and $\ddot{\mathbf{d}}$ are the displacement, velocity and acceleration vectors, respectively. The solution of the initial value problem for the system represented by Equation (4.4) is a displacement vector $\mathbf{d} = \mathbf{d}(t)$ satisfying the given initial conditions $\mathbf{d}(0) = \mathbf{d}_0$ and $\dot{\mathbf{d}}(0) = \mathbf{v}_0$. In transient calculations, the Newmark method with a-form implementation [130] is used to integrate Equation (4.4). The Newmark family of algorithms consists of the following equations

$$\mathbf{M}\mathbf{a}_{n+1} + \mathbf{C}\mathbf{v}_{n+1} + \mathbf{K}\mathbf{d}_{n+1} = \mathbf{F}_{n+1} \quad (4.5)$$

$$\mathbf{d}_{n+1} = \mathbf{d}_n + \Delta t \mathbf{v}_n + \frac{\Delta t^2}{2} [(1 - 2\beta)\mathbf{a}_n + 2\beta\mathbf{a}_{n+1}] \quad (4.6)$$

$$\mathbf{v}_{n+1} = \mathbf{v}_n + \Delta t [(1 - \gamma)\mathbf{a}_n + \gamma\mathbf{a}_{n+1}] \quad (4.7)$$

where \mathbf{d}_n , \mathbf{v}_n and \mathbf{a}_n are the approximations to $\mathbf{d}(t_n)$, $\dot{\mathbf{d}}(t_n)$ and $\ddot{\mathbf{d}}(t_n)$, respectively. Equation (4.5) is the equation of motion, and equations (4.6) and (4.7) are finite difference approximations for the evolution of the approximate solution in time. The parameters β and γ determine the accuracy and stability of the algorithm. Average acceleration method with parameter values $\beta=0.25$ and $\gamma=0.5$ which is implicit and unconditionally stable is used in this study. Effects of different β and γ values on the behavior of solutions can be found in [130]. Figure 4.4 shows the spectral radii for Newmark methods for varying β .

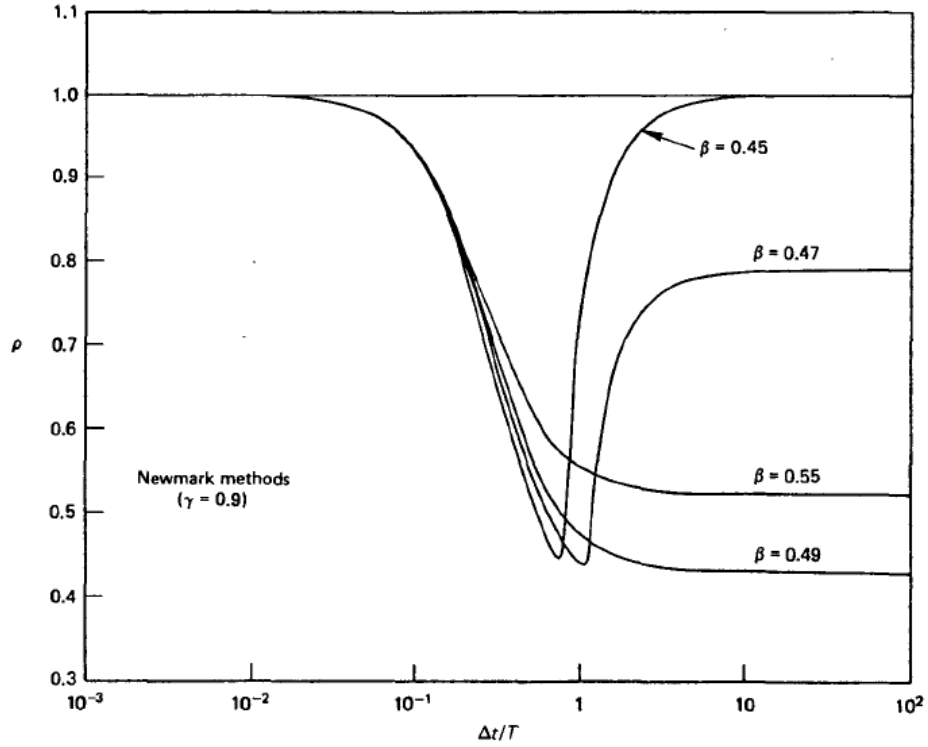


Figure 4.4: Spectral radii for Newmark methods for varying β [130].

Table 4.5: Properties of well-known members of the Newmark family [130].

Method	Type	β	γ
Average acceleration (trapezoidal rule)	Implicit	1/4	1/2
Linear acceleration	Implicit	1/6	1/2
Fox- Goodwin (royal road)	Implicit	1/12	1/2
Central difference	Explicit	0	1/2

Properties of some classical methods are summarized in Table 4.5. The average acceleration method is one of the most widely used methods for structural dynamics applications. Fox- Goodwin and linear acceleration methods are also implicit methods. However, these methods are conditionally stable and they are not economical for large-scale systems when compared to average acceleration method. The central difference method is conditionally stable. However, \mathbf{M} and \mathbf{C} matrices need to be diagonal. When the time step restriction is not too severe, the central difference method is generally the most economical and widely used [130].

Equations (4.5) to (4.7) are used to determine the three unknown vectors \mathbf{a}_{n+1} , \mathbf{d}_{n+1} and \mathbf{v}_{n+1} while \mathbf{a}_n , \mathbf{d}_n and \mathbf{v}_n are known vectors calculated in the previous step. Implementation of a-form is summarized the following lines. Firstly, predictors is defined as follows

$$\tilde{\mathbf{d}}_{n+1} = \mathbf{d}_n + \Delta t \mathbf{v}_n + \frac{\Delta t^2}{2} (1 - 2\beta) \mathbf{a}_n \quad (4.8)$$

$$\tilde{\mathbf{v}}_{n+1} = \mathbf{v}_n + \Delta t (1 - \gamma) \mathbf{a}_n \quad (4.9)$$

Equations (4.6) and (4.7) may then be written as

$$\mathbf{d}_{n+1} = \tilde{\mathbf{d}}_{n+1} + \Delta t^2 \beta \mathbf{a}_{n+1} \quad (4.10)$$

$$\mathbf{v}_{n+1} = \tilde{\mathbf{v}}_{n+1} + \Delta t \gamma \mathbf{a}_{n+1} \quad (4.11)$$

Then, \mathbf{a}_0 may be calculated as follows

$$\mathbf{M} \mathbf{a}_0 = \mathbf{F} - \mathbf{C} \mathbf{v}_0 - \mathbf{K} \mathbf{d}_0 \quad (4.12)$$

The recursion relation determines \mathbf{a}_{n+1} :

$$(\mathbf{M} + \Delta t \gamma \mathbf{C} + \Delta t^2 \beta \mathbf{K}) \mathbf{a}_{n+1} = \mathbf{F}_{n+1} - \mathbf{C} \tilde{\mathbf{v}}_{n+1} - \mathbf{K} \tilde{\mathbf{d}}_{n+1} \quad (4.13)$$

Following, Equations (4.10) and (4.11) are used to calculate \mathbf{d}_{n+1} and \mathbf{v}_{n+1} , respectively. In our numerical simulations, the viscous damping effect is neglected and the time step is chosen two orders of magnitude smaller than the periods of the first fundamental mode of the associated SLGS models. All the nodes on one edge are fully constrained, while the nodes on the opposite edge are subjected to initial displacements in dynamic simulations. Initial displacement is applied incrementally and then nodal coordinates, C-C bond lengths, angles between C-C-C bonds, stiffness and mass matrices of the original SLGS structure are updated at each displacement increment; then, the final configuration of the SLGSs is taken into account in all simulations. Thus, large deformation effects and uniform initial displacement conditions are considered in transient analyses. It is noteworthy that the Morse potential can easily be adapted to include nonlinear effects. Total initial displacement of 0.1 \AA is applied incrementally in positive x- and y-directions in planar simulations (e.g., see Figures 4.5 (a) and 4.5 (b)), while total displacement of 0.1 \AA is applied incrementally in positive z-direction in 3-D simulations (e.g., see Figure 4.5 (c)). Figure 4.5 shows the boundary conditions and loadings of the SLGSs

in 2-D and 3-D transient analyses. The MM and CM shell models of the SLGS used in transient analyses have the same dimensions as the models used in the vibrational analyses of the MM and CM shell models presented in Section 4.1.

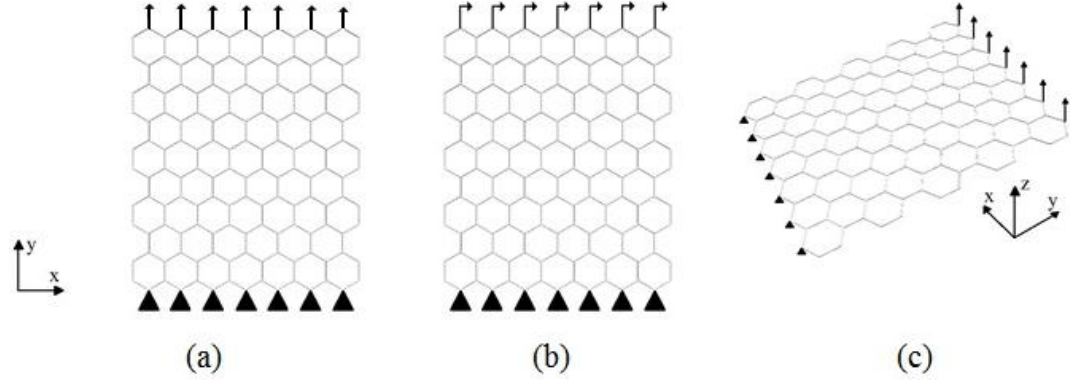


Figure 4.5: Boundary conditions and loadings of the MM models of SLGSs in transient analyses (a) 2-D model loaded in y-direction, (b) 2-D model loaded in x-direction and (c) 3-D model loaded in z-direction.

The time step is chosen as 100 ps for all transient analyses of 2-D SLGSs, which is sufficient to resolve transient behavior of the models. Figure 4.6 shows the displacement in y-direction for a node located in the middle of the SLGS subjected to in-plane initial displacement in y-direction as shown in Figure 4.5 (a). Figure 4.7 shows the displacement in x-direction for a node located in the middle of the SLGS subjected to in-plane initial displacement in x-direction as shown in Figure 4.5 (b). Observe in Figure 4.6 that beating occurs in mid-span displacement in y-direction due to very close natural frequencies existing in the SLGS structure. The frequency content of the displacement component in Figure 4.7 is examined by using the power spectral density plot shown in Figure 4.8 obtained by using Burg PSD estimator in MATLAB, that does not apply any window to data and minimizes the forward and backward prediction errors in the least square sense. The peak corresponding to the first natural frequency of 142 GHz appears in the spectrum plot. As can be seen in Figure 4.8, our findings are in good agreement with the first vibrational mode of the 2-D MM model subjected to free-fixed boundary conditions whose natural frequencies are listed in Table 4.3.

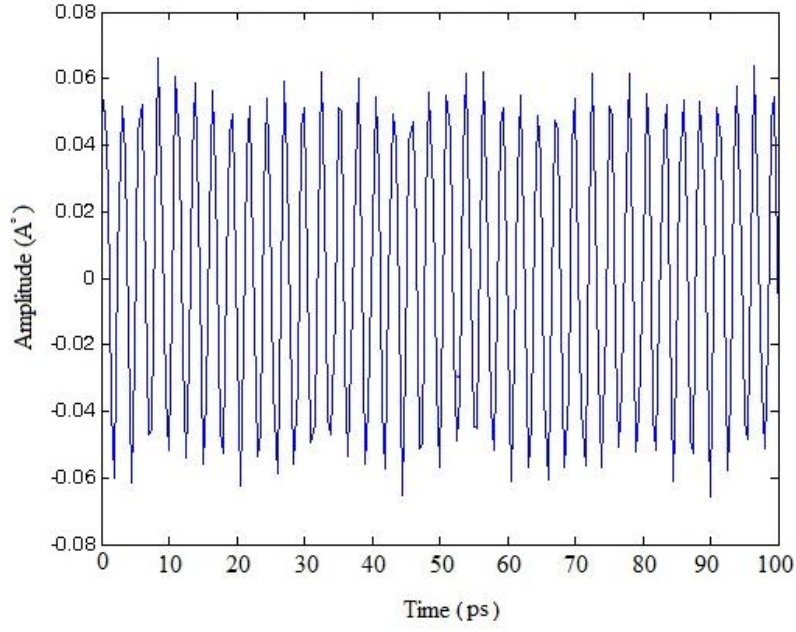


Figure 4.6: Variation of mid-span displacement in y-direction for 2-D MM model shown in figure 4.5 (a).

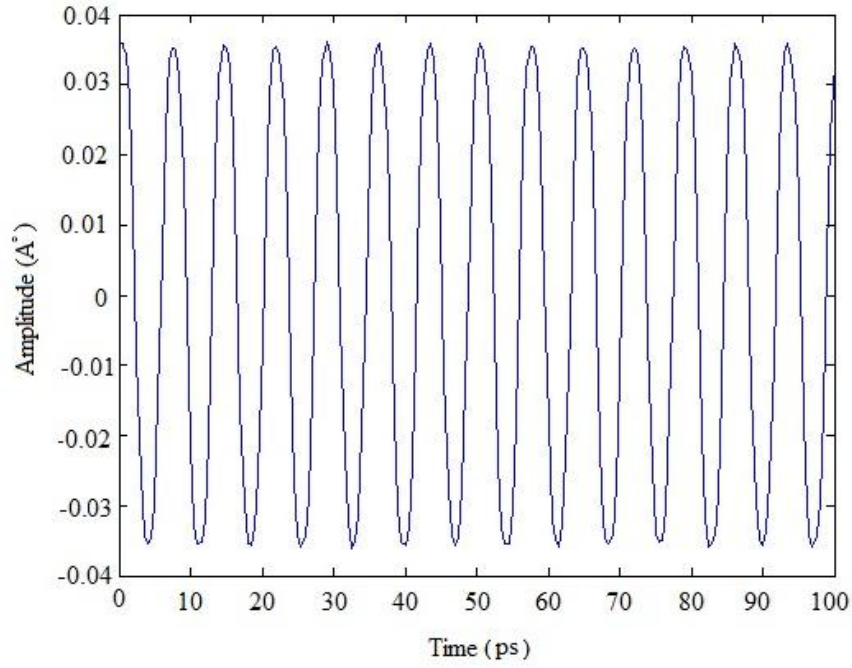


Figure 4.7: Variation of mid-span displacement in x-direction for 2-D MM model shown in Figure 4.5 (b).

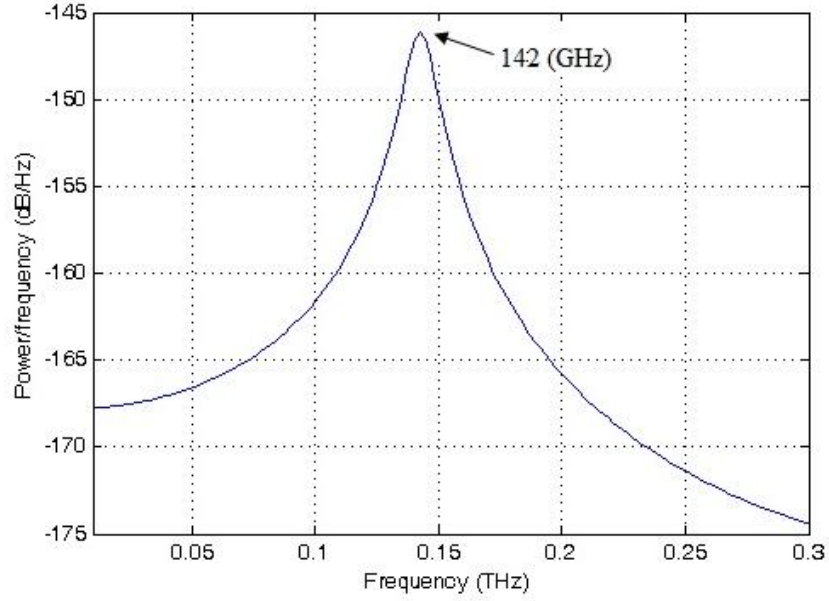


Figure 4.8: Power spectrum density plot of the 2-D MM model subjected to free-fixed boundary conditions.

For transient analyses of the 3-D SLGS models, the time step is chosen as 10 ns. Figure 4.9 shows the displacement in z-direction for a node located in the middle of the SLGS subjected to initial displacements shown in Figure 4.5 (c). Observe in Figure 4.9 that small amount of beating occurs in 3-D vibrations of the MM model of SLGSs as well. Figure 4.10 shows the frequency spectrum of the displacement component in Figure 4.9 obtained by using Burg PSD estimator in MATLAB. The peak corresponding to the first natural frequency of 2.37 GHZ appears in the spectrum plot. It can be seen that the findings of Figure 4.10 are in good agreement with the first natural frequency of the 3-D MM model of SLGSs subjected to free-fixed boundary conditions whose solutions are listed in Table 4.4. Although rotational DOF are included in FE models due to employment of consistent mass matrices, total translational kinetic energy is approximately 99.9% of the total kinetic energy; hence, it can be concluded that rotational kinetic energy is very small and employment of consistent mass matrix including rotational effects is acceptable.

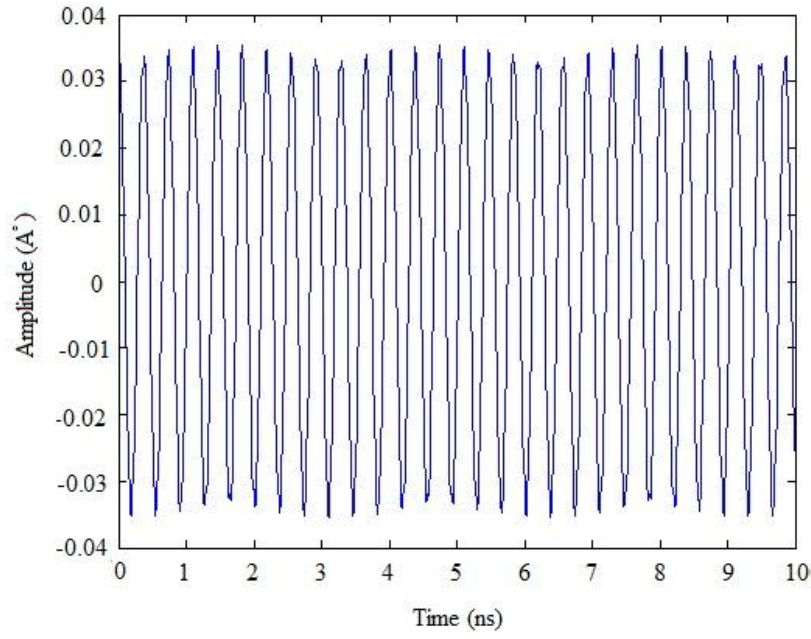


Figure 4.9: Variation of mid-span displacement in z-direction for the 3-D MM model shown in Figure 4.5 (c).

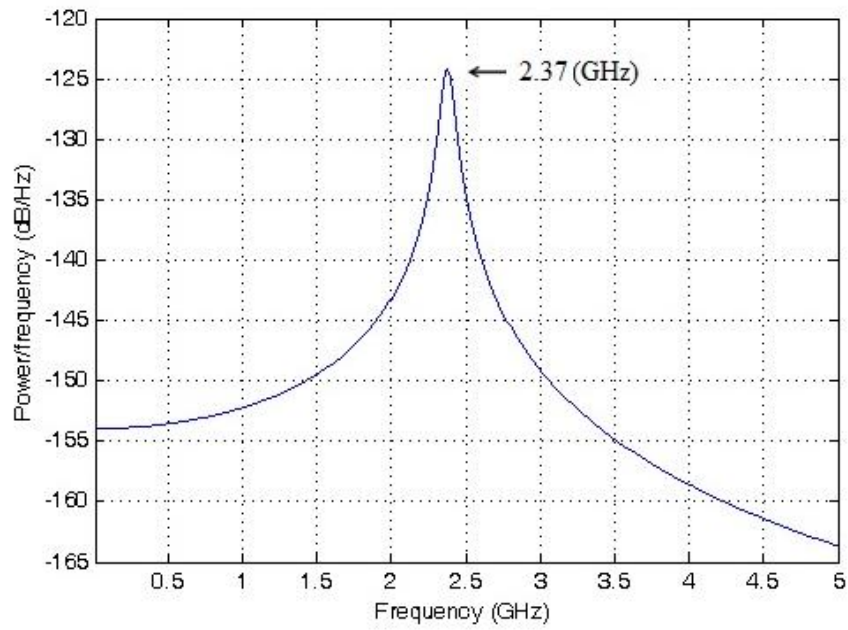


Figure 4.10: Power spectrum density plot of the 3-D MM model.

4.3. Fracture Analyses of SLGSs

In this section, an atomistic based FE model for prediction of fracture behavior of SLGSs is developed by considering large deformation and nonlinear geometric effects. EB beam elements are used to represent covalent bonds and non-linear characteristic of the beam elements are obtained by using the modified Morse potential. Formulation underlying the proposed approach is applied to defect-free, Stone-Wales (SW) and non-reconstructed one atom vacancy defected zigzag and armchair SLGSs.

4.3.1. FE formulation of the C-C bonds

The proposed model is basically a combination of the structural mechanic approach of Li and Chou [34] and the atomistic-based progressive fracture model of Tserpes et al. [85]. We already investigated mechanical properties, modal and transient behavior of SLGSs in Sections 4.1 and 4.2. Harmonic expressions for potential energy term are used and geometric constants are given in Table 4.6.

Table 4.6. Geometric properties of the EB beam element.

Bond thickness, d	1.47 \AA
Cross-sectional area, A	1.687 \AA^2
Moment of inertia, I	0.22682 \AA^4

If small deformation assumption exists, these parameters are sufficient to determine the behavior of an atomic bond. However, this assumption is not adequate for failure analysis of SLGSs which should be analyzed as a large deformation problem and geometric nonlinear effects have to be considered. To this end, at each load step, the loading is applied incrementally, non-linear characteristic of the EB beam elements are obtained by using the modified Morse potential and nodal coordinates are updated in this study. Planar beam formulation is sufficient to determine in plane fracture behavior of SLGSs and the element stiffness matrix of a planar EB beam element is given by Equation (3.1)

On the other hand, the EB beam element formulation does not consider shear deformation effects and exactly represent potential energy of interatomic bonds. Scarpa and Adhikari [49] proposed a beam model considering the shear deformation effects and they found new geometric and material properties of the beam element by

using the AMBER force model constants [34]. Both of the models in Li and Chou [34] and Scarpa and Adhikari [49] yield the same deformation results for small deformation problems. For large deformation problems, shear beam element (i.e., Timoshenko beam element) is not preferred since it is more difficult to be adapted for the modified Morse potential energy terms than the EB beam element.

For in-plane deformation problems of SLGSs, the atomistic interaction is mainly governed by the bond stretching and bond angle bending terms. As a result, according to the modified Morse potential, the potential energy can be expressed as Equations (3.37) – (3.38). The following equations can be obtained by differentiation of Equations (3.37)- (3.38)

$$F = 2\beta D_e (1 - e^{-\beta(r-r_0)}) e^{-\beta(r-r_0)} \quad (4.14)$$

$$M = k_\theta (\theta - \theta_0) + \left[+3k_{sextic} (\theta - \theta_0)^4 \right] \quad (4.15)$$

Equations (4.14)- (4.15) represent the force/bond length and momentum/C-C-C angle variation. Belytschko et al. [72] reported that the bond angle-bending potential does not contribute to the stretching energy and it has little effect on fracture in CNTs. The bond angle-bending potential energy term can be added to stabilize the molecular structure which is considered by the rigidity of the EB beam element and extra moment effect originating from Equation (4.15) (i.e., the second term in Equations (3.38) and (4.15)) is neglected. Note that force-strain curve obtained by using Equation (4.14) is highly nonlinear at large strain values and force-strain curve shapes of Brenner and modified Morse potential functions are very similar prior to the inflection point [72] (i.e., see Figure 4.11).

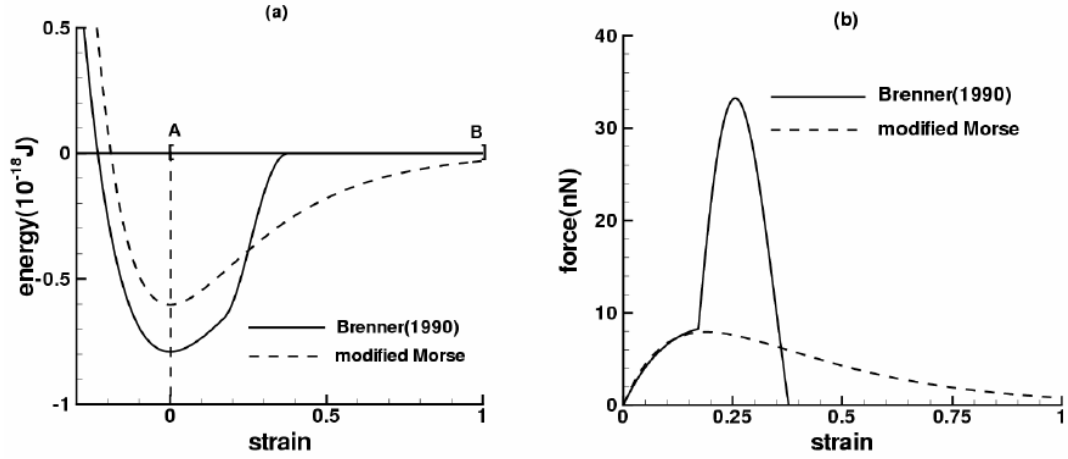


Figure 4.11: The Brenner and modified Morse potentials and tensile force fields. (a) potential field for Brenner and modified Morse potential (b) force fields in segment [AB] in part (a) [73].

Belytschko et al. [72] studied the fracture of CNTs by using MM simulations and reported that the fracture is almost independent of the dissociation energy and depends primarily on the inflection point of the interatomic potential. After the inflection point, the shape of the potential function is not important since material damage occurs. A cut-off distance (r_{cf}) based on bond-breaking criterion is very often used in atomistic simulations and different cut-off distances have been suggested in literature [75, 90]; in this thesis, the value of $r_{cf} = 0.169$ nm is employed which corresponds to the inflection point at approximately 19 % strain (i.e., the maximum of the interatomic force curve).

4.3.2. FE models of defect-free and defected SLGSs

Equivalent FE models of the defect-free and defected SLGSs are illustrated in Figure 4.12. The overall dimensions of the SLGSs are its length in the armchair (L_x) and zigzag (L_y) directions that are shown in Figure 4.12. In our simulations, the defect-free model of SLGSs has $125.52 \text{ \AA} \times 126.46 \text{ \AA}$ dimensions, and contains 6180 atoms (i.e., nodes) and 9159 bonds (i.e., elements).

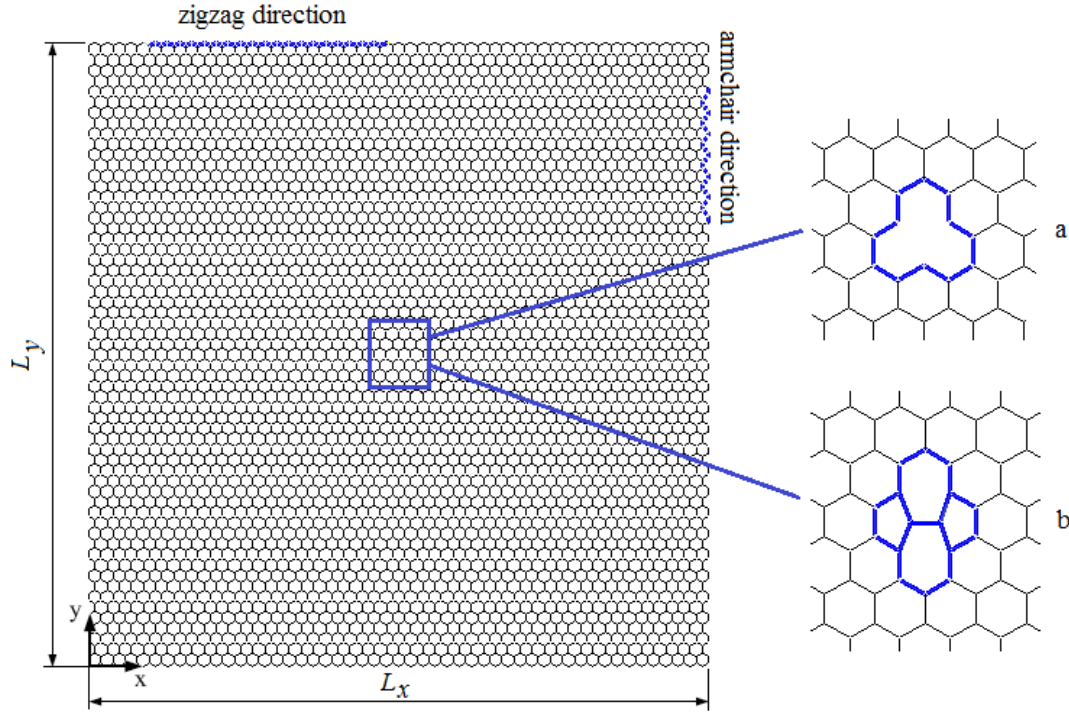


Figure 4.12: Equivalent FE model of the defect-free and defected SLGS model; (a) one atom vacancy, (b) SW defects

Production of mass-quantities of defect-free GSs or CNTs may prove challenging and different types of defects may exist in practice. It is reported in several QM and MD studies that these defects significantly affect the mechanical performance of these carbon based structures [71, 73, 75-79, 83]. In addition, a lot of MM based numerical studies exist about the effect of defects on fracture behavior of CNTs and GSs [72, 85, 86, 89, 91, 94]. The possible and mostly studied GS defects are incomplete bonding defects such as vacancies and topological defects such as the SW transformation. In addition, rehybridization and heterogeneous defects may exist in GS structures. These defects may be induced due to stress or emerge during the growth or synthesis processing [67]. Vacancy defects originate from missing atoms in the GSs and may occur due to an electron irradiation or oxidative purification. The SW defect involves the 90° rotation of a carbon bond about its center and is originally presented as the “SW transformation” [131]. Finally, four hexagons transform into two pentagons and two heptagons.

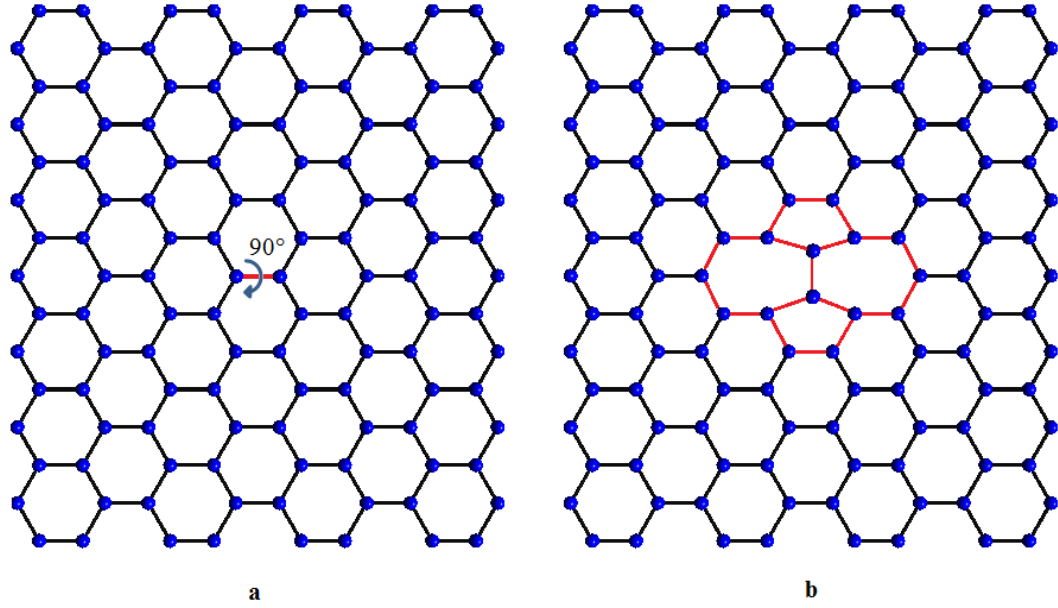


Figure 4.13: The SW defect generated by rotating the C–C bond (a) defect- free lattice and (b) SW- defected lattice.

Figure. 4.13 shows the SW (5-7-7-5) defect formation in the undeformed hexagonal lattice schematically. In this study, we considered one atom vacancy and SW defects, and investigated the effects of these defects on fracture behavior of SLGSs. Both zigzag and armchair directions are taken into account (e.g., see Figure 4.12). In all calculations, we assumed that the SW and one atom vacancy defects are located in the middle of the SLGSs. Figure 4.12 shows the defect-free sheet and the middle areas of the sheet where defects are located in the simulations. Sammalkorpi et al. [71] investigated the effect of reconstructed and non-reconstructed vacancy defects on tensile behavior of CNTs and show that the strength reduction caused by reconstructed case is smaller than that caused by their non-reconstructed case. Sammalkorpi et al. [71] used an annealing step beginning the MD simulations at high temperature for reconstruction. However, reconstruction does not occur in our simulation since the distance between the potential reaction atoms exceeds the interaction cut-off. On the other hand, although metastable, the non-reconstructed SWLNT configurations can be present at low temperatures and low dose irradiation [132, 133], and non-reconstructed defected SWCNTs used in several works in literature [85, 131, 134]. We considered non-reconstructed one atom vacancy defect in computational models, and one carbon atom and corresponding three C-C bonds are removed in the defect-free SLGSs (i.e., Figure 4.12). Nardelli et al. [68, 70] showed that defect nucleation in armchair CNTs and GSs under transverse tension

occurs via SW transformation at critical tensile strain of 5% in CNTs and somewhat later in GSs due to the absence of the additional curvature effect of the tubular structure. In addition, Zhang et al. [135] found that this transformation occurs at critical tensile strain of 6% for armchair CNTs and 12% for zigzag CNTs. In this study, strain barrier of 6 % for armchair SLGSs are considered for the formation of SW defects. It is noteworthy that 5% and 6% values of the strain barrier for the formation of SW defects did not affect our numerical results considerably. Tserpes et al. [86] used a combination of the stress-strain curve of defect-free and SW-defected CNTs to simulate fracture behavior of SWCNTs, and assumed that SWCNT dimensions remain unchanged after the formation of SW defects and neglected the deformation around the defect nucleation region. However, after the SW transformation, new configurations of the bonds affect the locations of neighboring atoms which change their locations into new lesser potential energy configurations. On the other hand, Xiao et al. [89, 91] proposed an interaction based mechanics approach to calculate the deformations caused by the formation of SW defects. In our study, to simulate the SW transformation, we started the simulations with defect-free GSs and the configurations of bonds are changed at the defect formation strain (e.g., Figure 4.13); then, initial pre-strain is applied to obtain minimized energy configurations of atoms and the simulation is continued until catastrophic failure of the SLGS.

4.3.3 Computational results

The procedure in our numerical studies is summarized in this section. Described by the modified Morse potential, the non-linear behavior of bonds is represented by EB beam elements and an incremental procedure is followed similar to [85] to apply the loading. Geometric parameters given in Table 4.6 are used for the EB beam elements. Note that the elasticity modulus is updated during load increments as the ratio of the stress to strain at a single point of the stress-strain curve, it is called the secant modulus in literature. Initial secant modulus of beam elements (i.e., 6.93 TPa) is obtained through the stress-strain curve of the C-C bond according to the modified Morse potential. Force- displacement, force- strain, stress- strain and secant modulus-strain curves of the C-C bond are shown in Figures 4.14 -4.17, respectively.

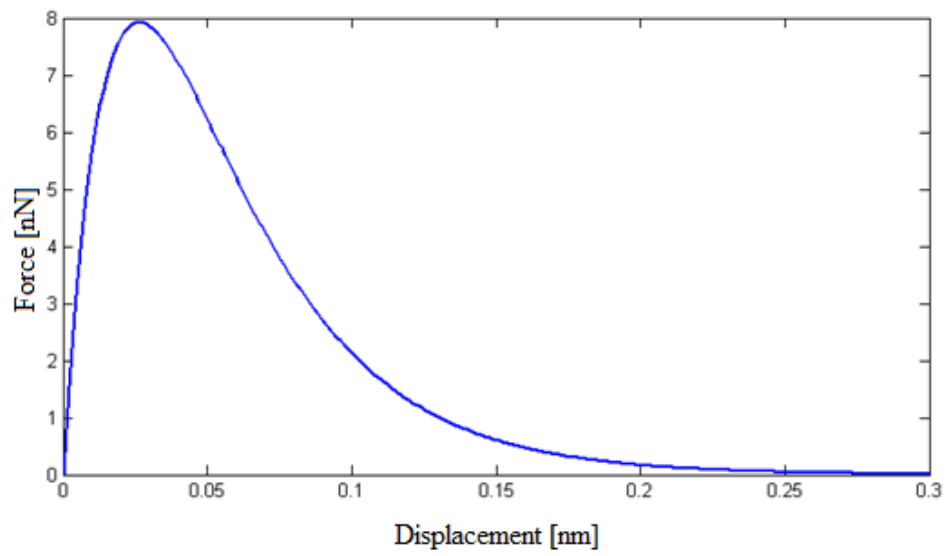


Figure 4.14: Force - displacement curve.

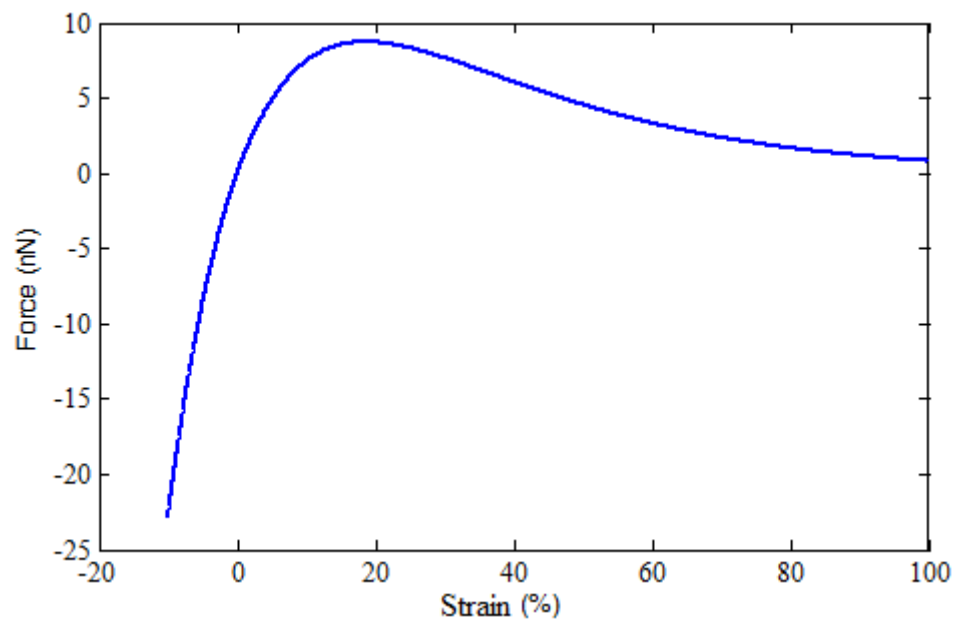


Figure 4.15: Force - strain curve.

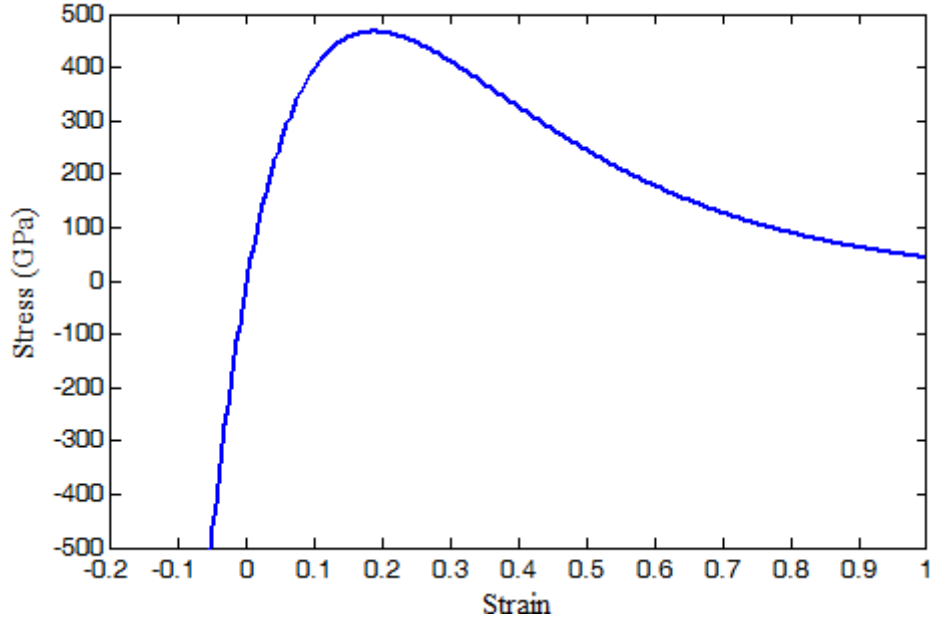


Figure 4.16: Stress - strain curve.

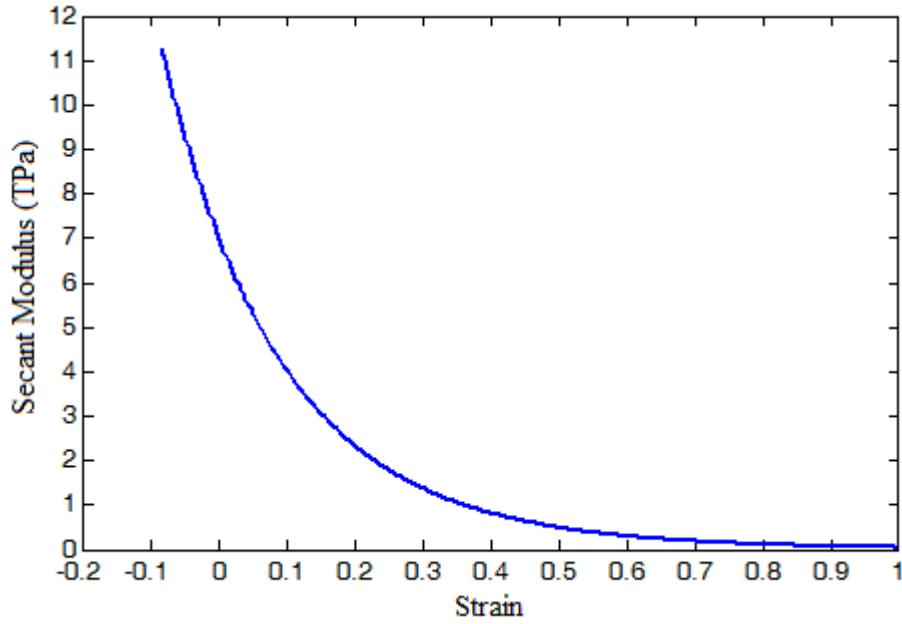


Figure 4.17: Secant's modulus - strain curve.

In simulations, all the nodes at one end of the zigzag (i.e., x - direction) or armchair (i.e., y - direction) SLGSs are fully constrained, while the nodes at the other end are subjected to an incremental displacement. The secant modulus and nodal coordinates of each element of the original SLGS structure is updated at each load step. At each load step, the secant modulus of each element is set to $F/(A\varepsilon)$, where A is the cross

sectional area of the element, ε axial strain of the each element, and F the interatomic force is calculated by Equation (4.14). When the axial strain of a bond reaches the critical fracture strain, then its stiffness matrix is multiplied by a very small number to simulate the bond break. Following, very small additional displacement is applied to the SLGSs and this iterative procedure goes on until the complete failure of SLGSs takes place. The strain in SLGSs is calculated by $\varepsilon_L = (L_s - L_{s0}) / L_{s0}$ where L_{s0} is the initial (equilibrium) length and L_s is the current length of the sheet material. The stress is calculated by $\sigma = F_g / (L_w t)$ where F_g is the corresponding applied tensile force computed by summation of the longitudinal reaction forces of the constrained nodes, L_w is the width of SLGSs and t is the thickness of the SLGSs. In all calculations, the thickness of 0.34 nm is used for the SLGSs. Accuracy of the results depends on the number of load steps. Hence, an acceptable strain increment is determined on a trial and error base to guarantee the convergence of numerical results. All fracture computations of the MM model are completed by using a computer code developed in MATLAB environment.

Table 4.7: Predicted failure strain (ϵ_f) and stress (σ_f) values of SLGSs .

Study	Method	Type	ϵ_f / σ_f (GPa)	Defect-free	SW	One atom vacancy
Present (with geometric nonlinearity effect)	MM	zigzag	ϵ_f	0.130	-	0.077
			σ_f	82.22	-	69.92
Present (without geometric nonlinearity effect)	MM	zigzag	ϵ_f	0.142	-	0.085
			σ_f	95.68	-	78.61
Present (with geometric nonlinearity effect)	MM	armchair	ϵ_f	0.174	0.088	0.108
			σ_f	102.15	77.38	86.34
Present (without geometric nonlinearity effect)	MM	armchair	ϵ_f	0.190	0.093	0.120
			σ_f	122.37	87.4	102.74
Yanovsky et al. [84]	QM	zigzag	ϵ_f	0.123	-	-
			σ_f	90.5	-	-
		armchair	ϵ_f	0.123	-	-
			σ_f	138.6	-	-
Xu [80]	MD	zigzag	ϵ_f	0.16	-	-
			σ_f	83	-	-
		armchair	ϵ_f	0.24	-	-
			σ_f	98	-	-
Liu et al. [81]	QM	zigzag	ϵ_f	0.194	-	-
			σ_f	110	-	-
		armchair	ϵ_f	0.266	-	-
			σ_f	121	-	-
Zhao et al.[82]	MD	zigzag	ϵ_f	0.130	-	-
			σ_f	90	-	-
		armchair	ϵ_f	0.20	-	-
			σ_f	107	-	-
Wang et al. [83]	MD	zigzag	ϵ_f	0.13	-	-
			σ_f	90	-	-
		armchair	ϵ_f	0.22	-	-
			σ_f	105	~ 92	~82
Ansari et al. [73]	MD	zigzag	ϵ_f	0.20	-	-
			σ_f	115.72	-	-
Xaio et al.[89]	MM	armchair	ϵ_f	-	~0.097	-
			σ_f	-	-	-

Table 4.7 shows the predicted failure strain (ϵ_f) and stress (σ_f) values of the SLGSs along with the experimental and numerical results in literature. It is observed in Table 4.7 that calculated failure strain and stress values lie in the same range with the results in literature. Moreover, our numerical results are very consistent with the numerical results on CNTs in literature [72, 78, 85, 86, 88, 89, 136]. It can be seen in Table 4.7 that by including large deformation and geometric nonlinearity effects, fracture stress and strain values reduced by about 11-17 % and 4-10 %, respectively. According to Table 4.7, the SLGS exhibits an orthotropic fracture behavior. Namely, it is stiffer in the armchair direction (i.e., x - direction) than in the zigzag direction

(i.e., y- direction). The fracture stress and strain values in the armchair direction are approximately 24 % and 34 % larger than those in the zigzag direction, respectively. This result agrees with the studies in literature. As expected, the fracture stress and strain values of defect-free SLGSs are the highest in Table 4.7 and these values reduce by the presence of defects in the structure. It is observed in Table 4.7 that fracture stresses of the zigzag and armchair SLGSs reduced by 14.9 % and 15.4 % if one atom vacancy defect exists in structures, respectively. It can be seen that SW defects resulted in reduction in fracture stress and strain values of the armchair SLGS structures (see Figure 4.12 b) as bond rearrangement causes stress concentration in vertical bonds and early bond fracture occurs. This result agrees with calculations on CNTs in literature [86, 89].

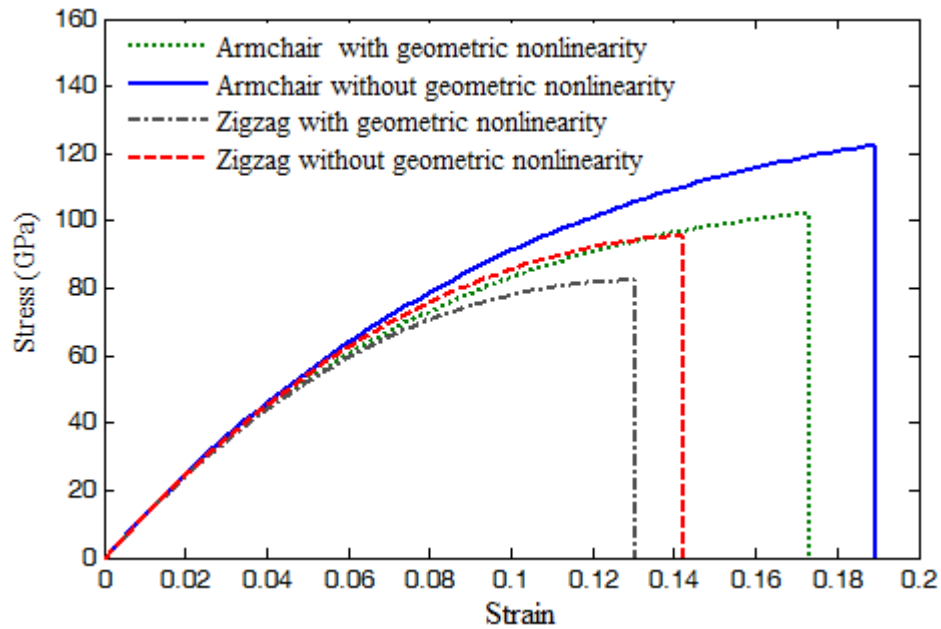


Figure 4.18: Stress- strain curves for defect-free armchair and zigzag type SLGSs with and without geometric nonlinearity effects.

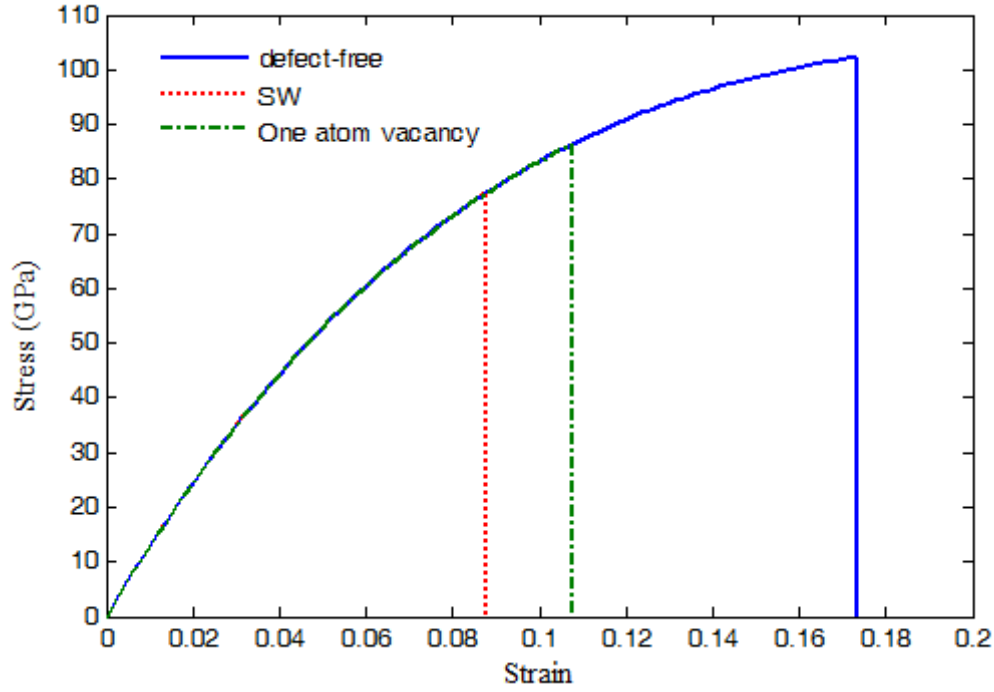


Figure 4.19: Stress- strain curves of armchair type SLGSs.

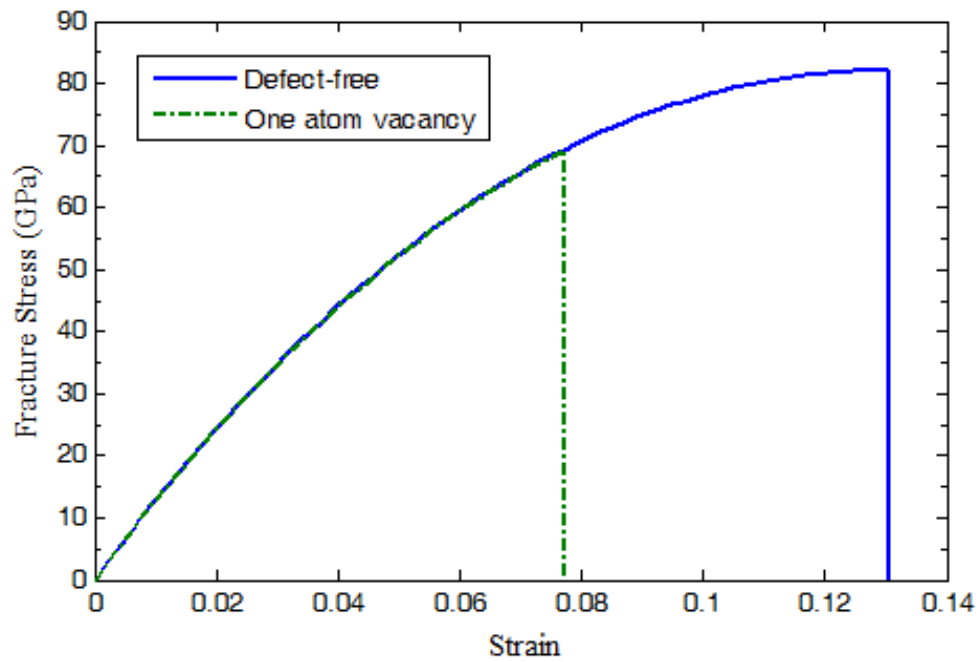


Figure 4.20: Stress- strain curves of zigzag type SLGSs.

Figure 4.18 shows the calculated stress–strain curves of defect-free armchair and zigzag type SLGSs with and without geometric nonlinearity effects. It can be seen in Figure 4.18 that consideration of geometric nonlinearity effects resulted in reduction

in fracture stress and strain values significantly. Figures 4.19 and 4.20 respectively show the stress- strain curves for defect-free and defected armchair and zigzag SLGSs by considering geometric nonlinearity effects. As can be seen in Figures 4.18 – 4.20, the resulting stress exhibits a sudden drop to zero when the stress reaches to the fracture stress. Hence, it is concluded that the fracture of all types of SLGSs are brittle which are also reported in several studies in literature [72, 73, 83, 85, 86, 91, 95].

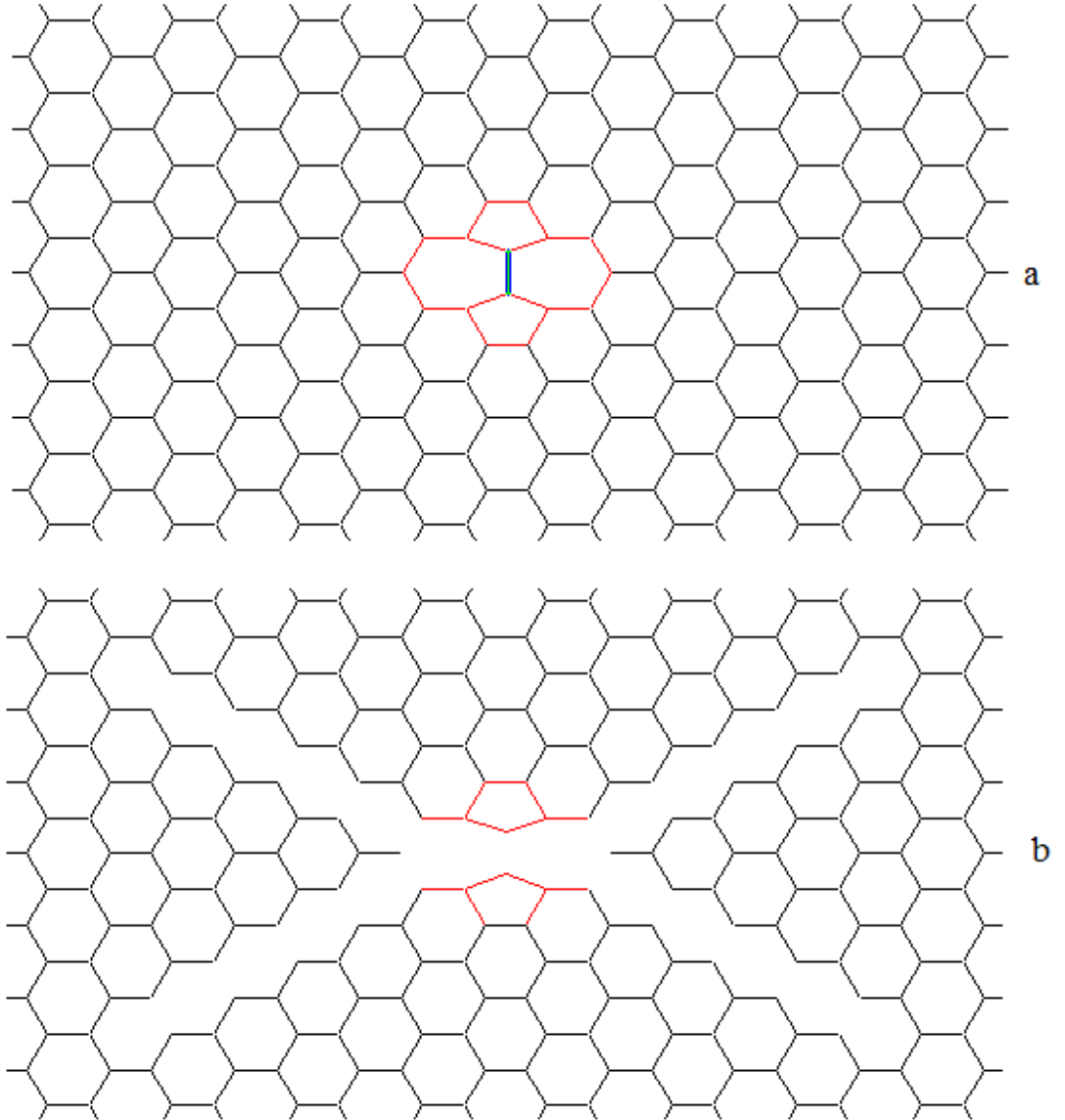


Figure 4.21: (a) Fracture initiation and (b) propagation directions of the SW-defected armchair SLGS.

Our proposed approach is able to give the correct prediction of fracture initiation and post failure behavior of SLGSs. However, the accuracy of predicting crack propagation in nanoscale is limited as the modified Morse potential function does not consider many-body interactions and it is not capable of describing the behavior of SLGSs after the C-C bonds are broken where the reconfiguration of bonds and structural transformations may occur. Figures 4.21 and 4.22 respectively show the fracture initiation and crack propagation directions of the SW-defected armchair SLGSs and one atom vacancy defected zigzag SLGSs.

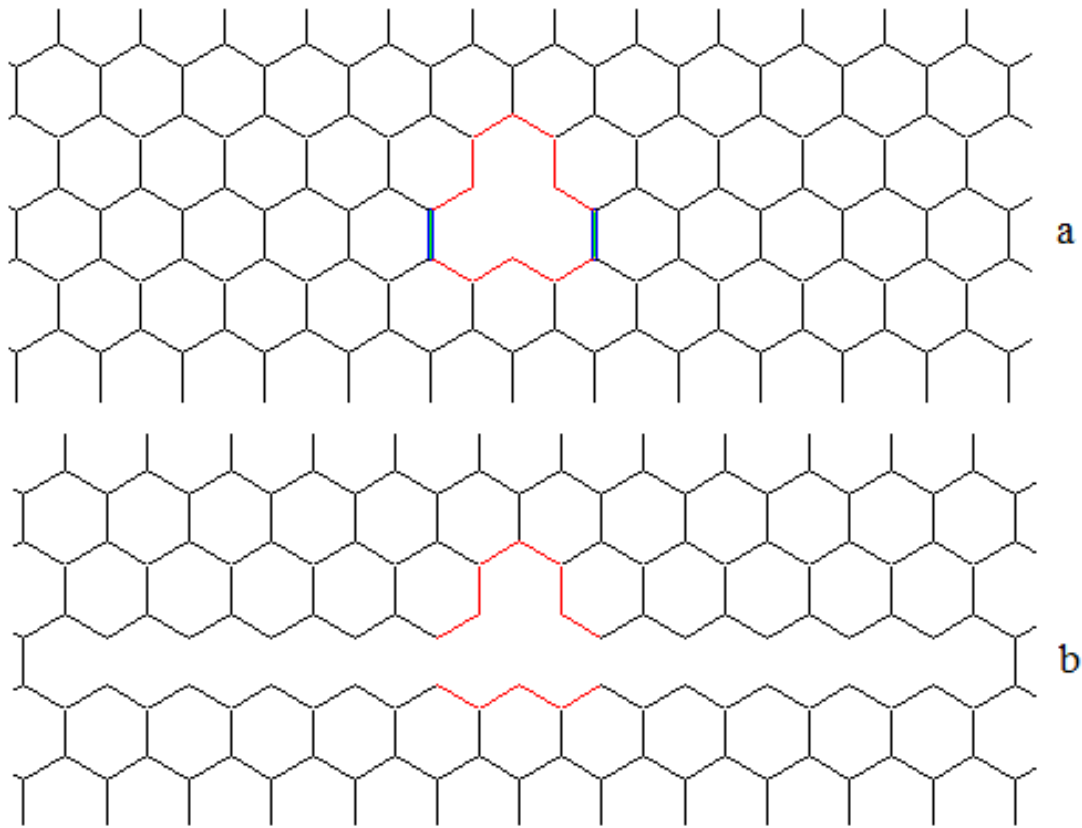


Figure 4.22: (a) Fracture initiation and (b) propagation directions of one atom vacancy defected zigzag SLGS.

As can be seen in Figure 4.21 that the fracture initiated from the vertical bond which connects the two pentagons and continued diagonal crack paths. Crack propagation direction is in maximum shear stress directions having an angle of $\pm 45^\circ$ with the horizontal direction. Similar fracture patterns are also observed in literature [72, 86, 89] for the SW- defected CNTs and SLGSs. As can be seen in Figure 4.22, the fracture initiated from the vertical bond which is shown in dark colour in Figure

4.22a and propagated in the same row of bonds. The same crack propagation characteristic has been observed in studies on CNTs in literature [72, 85].

5. COUPLED MOLECULAR/CONTINUUM MECHANICAL MODELING OF SLGSs

In this section, a coupling method for the MM and CM models is derived based on an augmented formulation of atomistic and continuum displacement fields in a moving least square sense, which originates from an unconstrained optimization problem to be solved. The augmented problem is solved by the Lagrange multiplier method and it allows multiscale analyses of multiple numbers of molecular mechanics (MM) domains in a single continuum mechanics (CM) domain. In contrast to alternative approaches in literature, there is no need for an overlapping domain in the proposed approach and the MM domain(s) can be placed arbitrarily in the CM domain; hence, one can focus on any desired CM subdomain where we need to obtain atomistic solution. Formulations underlying the proposed approach are presented and applied to defect-free and defected SLGSs. In the atomistic models, harmonic and modified Morse potentials are employed to simulate problems of defect-free small deformation and defected large deformation SLGSs. In the CM domain, it is assumed that deformations are elastic and plane stress conditions exist whose elasticity modulus and Poisson's ratio values are obtained by the use of MM models. In order to verify the proposed approach, deformation and damage of SLGSs are examined and comparisons are made with the results given in literature. It is shown that proposed approach can compute the deformations of SLGSs in high accuracy, enables to obtain MM solution in any part of the CM domain and can be easily applied to other materials such as carbon nanotubes [137].

5.1 Computational Framework

This section presents a mathematically consistent coupled framework for linking the MM model used at very fine-scales and CM model used at coarse scales. The coupled approach consists of three components: the atomistic domain, continuum

domain and coupling method. We will present these components in the following subsections.

5.1.1 Atomistic and continuum domain formulations

For the atomistic scale simulation of SLGSs, an atomistic based FE model presented in Sections 3 and 4 is used. In the continuum domain, it is assumed that plane stress conditions exist, for which elasticity modulus and Poisson's ratio values of the CM domain are obtained by the use of full atomistic MM models. By updating the elasticity parameters of the CM domain based on the MM solutions, nonlinear effects are considered in iterative solutions of large deformation problems. In atomistic and continuum plane stress calculations, the nominal thickness of 0.34 nm is used for the graphene layer.

Linear quadrilateral (rectangular) elements are used in plane stress models. The main reason is that the linear quadrilateral elements are usually more accurate than linear triangular elements as the strain vector of the linear quadrilateral elements is not constant. Hence, more realistic presentation of strain is obtained when linear quadrilateral (rectangular) elements are used. The element stiffness matrix for linear quadrilateral (rectangular) elements is as follows

$$\mathbf{K}_e^C = \int_A h \mathbf{B}^T \mathbf{C} \mathbf{B} dA = \int_{-1}^1 \int_{-1}^1 ahb \mathbf{B}^T \mathbf{C} \mathbf{B} d\xi d\eta \quad (5.1)$$

where \mathbf{B} is the strain matrix, \mathbf{C} is the material constant matrix and the dimension of the element is defined $2a \times 2b \times h$. A local natural coordinate system (ξ, η) with its origin located at the center of the quadrilateral element is defined. Figure 5.1 show the quadrilateral element and the corresponding coordinate systems.

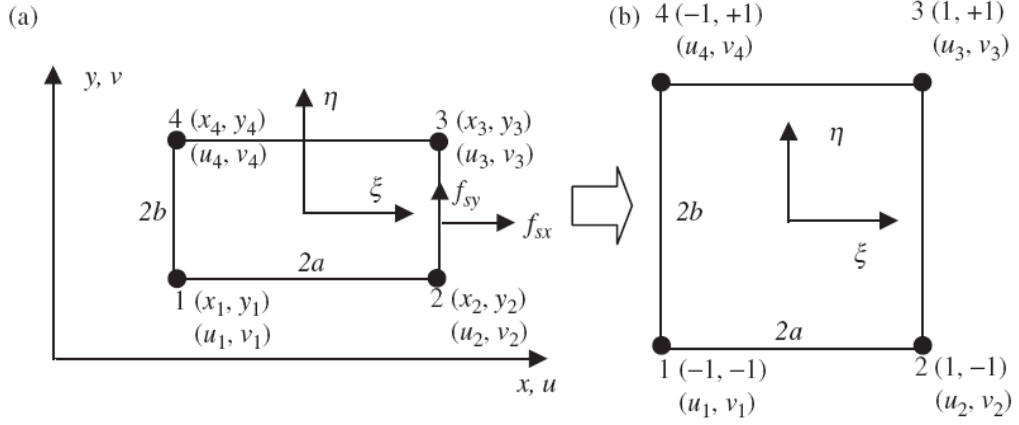


Figure 5.1: Quadrilateral element and coordinate systems. (a) Quadrilateral element in physical system, (b) square element in natural coordinate system [138].

The relationship between the physical coordinate (x, y) and local coordinate system (ξ, η) is as follows

$$\xi = \frac{x}{a}, \quad \eta = \frac{y}{b} \quad (5.2)$$

Equation 5.2 defines a very simple coordinate mapping between physical and natural coordinates systems for quadrilateral element as shown in Figure 5.1. The displacement vector \mathbf{U} as follows

$$\mathbf{U}(x, y) = \mathbf{N}(x, y) \mathbf{d}_e^C \quad (5.3)$$

where the nodal displacement vector \mathbf{d}_e^C is arranged in the form as follows

$$\mathbf{d}_e^C = \begin{bmatrix} u_1 & v_1 & u_2 & v_2 & u_3 & v_3 & u_4 & v_4 \end{bmatrix}^T \quad (5.4)$$

In global x and y coordinate system, the nodal displacements and rotations are defined for rectangular element as follows

- u_1, v_1 x and y displacements at node 1
- u_2, v_2 x and y displacements at node 2
- u_3, v_3 x and y displacements at node 3
- u_4, v_4 x and y displacements at node 4

and the interpolation functions are given by

$$\mathbf{N} = \begin{bmatrix} N_1 & 0 & N_2 & 0 & N_3 & 0 & N_4 & 0 \\ 0 & N_1 & 0 & N_2 & 0 & N_3 & 0 & N_4 \end{bmatrix} \quad (5.5)$$

where N_i ($i=1,2,3,4$) are the interpolation function corresponding to the four nodes of the rectangular element and defined as follows

$$\begin{aligned} N_1 &= \frac{1}{4}(1-\xi)(1-\eta) \\ N_2 &= \frac{1}{4}(1+\xi)(1-\eta) \\ N_3 &= \frac{1}{4}(1+\xi)(1+\eta) \\ N_4 &= \frac{1}{4}(1-\xi)(1+\eta) \end{aligned} \quad (5.6)$$

The strain matrix \mathbf{B} has the form

$$\mathbf{B} = \mathbf{L}\mathbf{N} \quad (5.7)$$

where \mathbf{L} is called a differential operation matrix and defined as follows

$$\mathbf{L} = \begin{bmatrix} \partial/\partial x & 0 \\ 0 & \partial/\partial y \\ \partial/\partial y & \partial/\partial x \end{bmatrix} \quad (5.8)$$

By substituting Equations (5.8) and (6.5) into Equation (5.7), we have

$$\mathbf{B} = \begin{bmatrix} -\frac{1-\eta}{a} & 0 & \frac{1-\eta}{a} & 0 & \frac{1+\eta}{a} & 0 & -\frac{1+\eta}{a} & 0 \\ 0 & -\frac{1-\xi}{b} & 0 & -\frac{1+\xi}{b} & 0 & \frac{1+\xi}{b} & 0 & \frac{1-\xi}{b} \\ -\frac{1-\xi}{b} & -\frac{1-\eta}{a} & -\frac{1+\xi}{b} & \frac{1-\eta}{a} & \frac{1+\xi}{b} & \frac{1+\eta}{a} & \frac{1-\xi}{b} & -\frac{1+\eta}{a} \end{bmatrix} \quad (5.9)$$

Material constant matrix \mathbf{C} for plane stress and isotropic materials is defined as follows

$$\mathbf{C} = \frac{E}{1-\nu^2} \begin{bmatrix} 1 & \nu & 0 \\ \nu & 1 & 0 \\ 0 & 0 & (1-\nu)/2 \end{bmatrix} \quad (5.10)$$

where E is the elasticity modulus and ν is the Poisson's ratio of the element.

5.1.2 Coupling strategy

Consider a planar body which is decomposed into two domains: an atomistic domain Ω^A and a continuum domain Ω^C . The superscripts 'A' and 'C' are used to denote atomistic and continuum identifiers, respectively. Γ^A represents the boundary of the atomistic domain Ω^A which surrounds outer elements of Ω^A . Possible compositions of Ω^A and Ω^C domains are shown in Figure 5.2, where it is noteworthy that location(s) and number of the MM domains can be arbitrary. For simplicity, we will consider the case that the MM domain is located in the center of an element in the CM domain (e.g., see Figure 5.2b). It is assumed that atomistic domain Ω^A is traction free, and the traction is only applied to the boundary Γ^C of the continuum domain Ω^C . The displacement field is decomposed into a fine scale solution \mathbf{u}^A and a coarse scale solution \mathbf{u}^C .

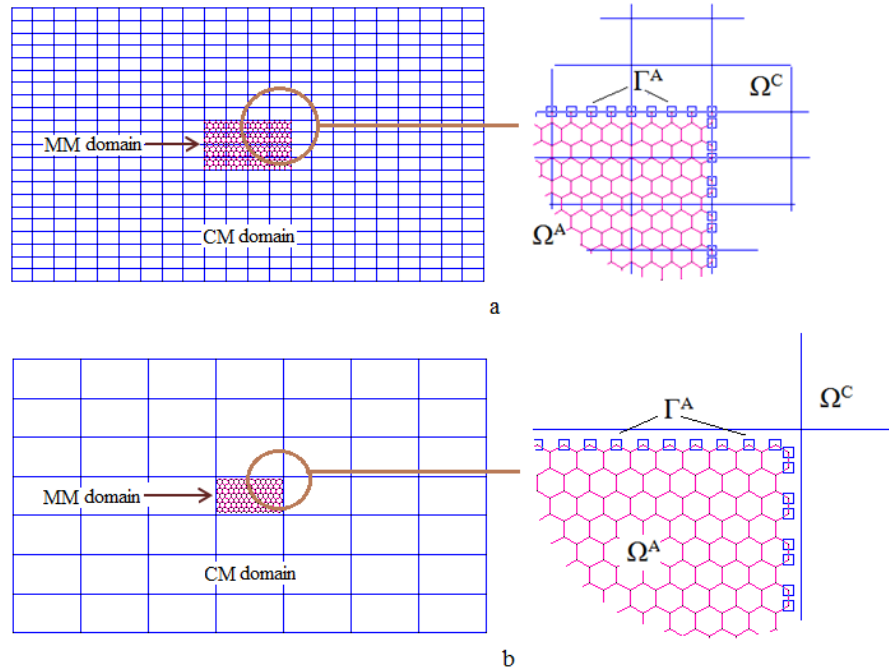


Figure 5.2: Composition of Ω^A and Ω^C domains, (a) atomistic domain overlaps with several CM elements, (b) atomistic domain coincides with one CM element.

In this paper, the CM domain is modeled as a plane-stress material, while the atomistic bonds are modeled by using Euler-Bernoulli beams. The variational formulations and Galerkin approximation to plane-stress material and Euler-

Bernoulli beam are omitted for brevity (e.g., see [124]). In brief, the associated FE formulations can be written in the following matrix forms at element level

$$\mathbf{K}_e^C \mathbf{u}_e^C = \mathbf{f}_e^C \quad (5.11)$$

$$\mathbf{K}_e^A \mathbf{u}_e^A = \mathbf{f}_e^A \quad (5.12)$$

where the subscript e denotes the element number, and \mathbf{K}_e^C and \mathbf{K}_e^A are element stiffness matrices for the plane-stress continuum element and Euler-Bernoulli beam element, respectively; \mathbf{u}_e^C and \mathbf{u}_e^A are unknown nodal displacement vectors for the plane-stress continuum element and beam element, respectively; \mathbf{f}_e^C and \mathbf{f}_e^A are element force vectors for the plane-stress continuum element and beam element, respectively. Following, by assembling the element equations given by Equations (5.11) and (5.12), the global equation systems for the plane-stress CM domain and atomistic fine-scale domain can be respectively written as follows

$$\mathbf{K}^C \mathbf{u}^C = \mathbf{f}^C \quad (5.13)$$

$$\mathbf{K}^A \mathbf{u}^A = \mathbf{f}^A \quad (5.14)$$

The missing link between the continuum and atomistic domains is the coupling method. The relations between the displacement field of an atomistic domain and that of the surrounding continuum domain can be expressed as follows

$$\mathbf{u}^C(\mathbf{x}) = E[\mathbf{u}^A(\mathbf{x} + (\delta\mathbf{x}))] \quad (5.15)$$

$$\mathbf{f}^C(\mathbf{x}) = E[\mathbf{f}^A(\mathbf{x} + (\delta\mathbf{x}))] \quad (5.16)$$

where the $E[.]$ is the operator taking the average of the argument, \mathbf{x} is the location vector and $\delta\mathbf{x}$ is the perturbation given to \mathbf{x} . In addition, due to the FE formulation, we have

$$\mathbf{u}_e^C(\mathbf{x}) = \sum_{i=1}^P N_i(\mathbf{x}) \mathbf{u}_i^C \quad (5.17)$$

where $N_i(\mathbf{x})$ are the shape functions, and P equals to 3 for planar triangular elements and 4 for planar quadrilateral elements. Referring to Figure 5.2b, the following relation should hold for an atomistic domain having the boundary Γ^A whose surrounding continuum domain has the solution of $\mathbf{u}_e^C(\mathbf{x})$

$$E \left[\begin{matrix} A \\ \Gamma^A \end{matrix} \right] = \mathbf{u}_e^C(\mathbf{x}) \quad (5.18)$$

For instance, if an atomistic domain lies in a planar quadrilateral continuum element (i.e., Figure 5.2b); then, we can write the following relations for a node on Γ^A

$$E \left[\begin{matrix} A \\ \Gamma^A \end{matrix} \right] = u_e^C(\mathbf{x}) = N_1(\mathbf{x})u_{1e}^C + N_2(\mathbf{x})u_{2e}^C + N_3(\mathbf{x})u_{3e}^C + N_4(\mathbf{x})u_{4e}^C \quad (5.19)$$

$$E \left[\begin{matrix} A \\ \Gamma^A \end{matrix} \right] = v_e^C(\mathbf{x}) = N_1(\mathbf{x})v_{1e}^C + N_2(\mathbf{x})v_{2e}^C + N_3(\mathbf{x})v_{3e}^C + N_4(\mathbf{x})v_{4e}^C \quad (5.20)$$

where u_e^C and v_e^C represent respectively the horizontal and vertical displacement components, and $(u_{1e}^C, u_{2e}^C, u_{3e}^C, u_{4e}^C)$ and $(v_{1e}^C, v_{2e}^C, v_{3e}^C, v_{4e}^C)$ respectively denote the nodal values of horizontal and vertical displacement components. The subscript Γ^A denotes that the associated variable is evaluated on Γ^A . Following, we can write two equations per an atomistic node on the boundary Γ^A for horizontal and vertical displacement components that can be arranged in matrix form as follows

$$\begin{bmatrix} N_1(x_1) & N_1(x_1) & N_2(x_1) & N_2(x_1) & N_3(x_1) & N_3(x_1) & N_4(x_1) & N_4(x_1) \\ \cdot & \cdot & \cdot & \cdot & \cdot & \cdot & \cdot & \cdot \\ \cdot & \cdot & \cdot & \cdot & \cdot & \cdot & \cdot & \cdot \\ \cdot & \cdot & \cdot & \cdot & \cdot & \cdot & \cdot & \cdot \\ N_1(x_n) & N_1(x_n) & N_2(x_n) & N_2(x_n) & N_3(x_n) & N_3(x_n) & N_4(x_n) & N_4(x_n) \end{bmatrix} \begin{bmatrix} u_{1e}^C \\ v_{1e}^C \\ u_{2e}^C \\ v_{2e}^C \\ u_{3e}^C \\ v_{3e}^C \\ u_{4e}^C \\ v_{4e}^C \end{bmatrix} = \begin{bmatrix} u_1^A \\ v_1^A \\ u_2^A \\ v_2^A \\ \cdot \\ \cdot \\ u_n^A \\ v_n^A \end{bmatrix} \quad (5.21)$$

where n is the number of atoms on the boundary Γ^A . Then, Equation (5.21) can be written as

$$\mathbf{A} \mathbf{u}_e^C = \mathbf{u}_{\Gamma^A}^A \quad (5.22)$$

where the coefficient matrix $A \in R^{n \times m}$ supplies projection of displacements of the CM and MM domains, m equals to 6 for a planar triangular and 8 for a quadrilateral element, and \mathbf{x}_i are the coordinates of the i th atom.

Locations of atoms on Γ^A used for least squares projection may be located on CM element boundaries as shown in Figure 5.2b or inside a CM element as shown in Figure 5.2a; nonetheless, by proper choice of projection matrix A , Equation (5.22) can be used for projection for all cases. Note that Equation (5.22) is an overdetermined equation system whose solution can be calculated by using the pseudo-inverse in a least-square sense as follows

$$\mathbf{u}_e^C = (A^T A)^{-1} A^T \mathbf{u}_{\Gamma^A}^A \quad (5.23)$$

which is a least squares fit equation that links the atomistic displacements on the boundary Γ^A with nodal displacements of Ω_e^C . Locations and number of overlapping elements can be selected arbitrarily, and no bridging domain is used. Following, the coupling of CM and MM solutions is set up as an optimization problem to solve Equations (5.13), (5.14) and (5.23) concurrently. Common approach to the solution of constrained optimization is to introduce m Lagrange multipliers λ_i and define an equivalent unconstrained optimization problem as follows [124]:

Find \mathbf{u}^C , \mathbf{u}^A and λ such that

$$\text{minimize } L = \frac{1}{2} \mathbf{u}^{CT} \mathbf{K}^C \mathbf{u}^C + \frac{1}{2} \mathbf{u}^{AT} \mathbf{K}^A \mathbf{u}^A - \mathbf{u}^{CT} \mathbf{f}^C - \mathbf{u}^{AT} \mathbf{f}^A + \lambda^T (\mathbf{u}^C - B \mathbf{u}^A) \quad (5.24)$$

where L is the Lagrangian, superposed T denotes matrix transpose and

$$B = (A^T A)^{-1} A^T \quad (5.25)$$

Solution of Equation (5.24) yields \mathbf{u}^A and \mathbf{u}^C by the least squares fit of \mathbf{u}^A and \mathbf{u}^C on Γ^A . By using Equations (5.22) and (5.25), we introduce two new projection matrices E_1 and E_2 to extract the DOF determined below

$$\mathbf{u}_e^C = B \mathbf{u}_{\Gamma^A}^A = B E_2 \mathbf{u}^A \quad (5.26)$$

$$\mathbf{u}_e^C = \mathbf{E}_1 \mathbf{u}^C \quad (5.27)$$

$$\mathbf{E}_1 \mathbf{u}^C = \mathbf{B} \mathbf{E}_2 \mathbf{u}^A \quad (5.28)$$

where $\mathbf{E}_1 \in R^{k \times l}$ (k is equal to total DOF of elements in a single element Ω_e^C , which is 6 for a planar triangular element and 8 for a quadrilateral element, and l is equal to total DOF of elements in the entire Ω^C domain) and $\mathbf{E}_2 \in R^{p \times r}$ (p is equal to total DOF of atoms on the boundary Γ^A and r is equal to total DOF of atoms in the entire Ω^A domain). Note that the projection matrices \mathbf{E}_1 and \mathbf{E}_2 provide us extraction of selected DOF out of displacement components of the CM and MM domains, respectively. Rows of \mathbf{E}_1 and \mathbf{E}_2 are formed of unit vectors $\mathbf{e}_j = [\dots 0 \ 1 \ 0 \ \dots]$ whose j th component is equal to one and all other components are zero.

Using the optimization steps given on p.76 of [124], the solution of the optimization problem Equation (5.24) is given by:

$$\begin{bmatrix} \mathbf{K}^A & (\mathbf{B}\mathbf{E}_2)^T \\ \mathbf{B}\mathbf{E}_2 & \mathbf{0} \end{bmatrix} \begin{bmatrix} \mathbf{u}^A \\ \lambda \end{bmatrix} = \begin{bmatrix} \mathbf{f}^A \\ \mathbf{E}_1 \mathbf{u}^C \end{bmatrix} \quad (5.29)$$

and the augmented equation system can be expressed as

$$\begin{bmatrix} \mathbf{K}^C & \mathbf{0} & \mathbf{0} \\ \mathbf{0} & \mathbf{K}^A & (\mathbf{B}\mathbf{E}_2)^T \\ -\mathbf{E}_1 & \mathbf{B}\mathbf{E}_2 & \mathbf{0} \end{bmatrix} \begin{bmatrix} \mathbf{u}^C \\ \mathbf{u}^A \\ \lambda \end{bmatrix} = \begin{bmatrix} \mathbf{f}^C \\ \mathbf{f}^A \\ \mathbf{0} \end{bmatrix} \quad (5.30)$$

By solving the augmented equation system of (5.30), we get the solutions of Equations (5.13), (5.14) and (5.23) concurrently.

In brief, this approach is flexible such that it allows placement of the MM domain in any region of the CM domain without introducing an overlapping region. If the global stiffness matrices for the MM and CM domains are given, fine scale solution of any subdomain of the CM domain can be obtained by proper choice of projection matrices \mathbf{E}_1 and \mathbf{E}_2 .

5.2 Numerical Examples

For the validation of molecular, continuum and coupled models, two static loading and three fracture mechanic problems are solved. All coupled and full atomistic model computations are completed by using a computer code developed in MATLAB environment. Note that the full atomistic model having 494,548 atoms is solved by using Ansys software that is used as the reference solution.

5.2.1 Static loading

In the first example on static loading, the Young's and shear moduli of the zigzag type SLGSs having different sizes are calculated by using the full atomistic MM models based on harmonic potentials and compared with the results reported in literature. The models are assumed to be homogeneous, elastic, plane-stress and meshed with quadrilateral elements. In simulations, one end of the sheet is constrained and the other end is subjected to uniform tensile loads. All load vector calculations are based on consistent load formulations. The Young's modulus of a material is defined to be the ratio of normal stress to normal strain, i.e., $E = \sigma / \varepsilon$ for a graphene layer. The Poisson's ratio is defined as the ratio of transverse contraction strain to longitudinal extension strain in the direction of stretching force, i.e., $\nu = -\varepsilon_t / \varepsilon_l$. Once the Poisson's ratio is calculated, then the shear modulus can be found by $G = E / 2(1 + \nu)$. Table 5.1 lists the values of tensile rigidity Y and shear modulus G calculated by our model and presented in literature. Observe that Y and G values reported in literature show dispersion.

Table 5.1. Values of tensile rigidity Y , shear modulus G and thickness t of SLGSs.

Reported by	Y (TPa nm)	G (TPa)	t (nm)	Method
Li and Chou [34]	0.338-0.351	-	0.34	Numerical
Scarpa <i>et al.</i> [49]	0.064-0.546	-	0.074- 0.099	Numerical
Gupta and Batra [52]	0.340	1.4	0.1	Numerical
Lee <i>et al.</i> [21]	0.335	-	0.335	Experimental
Min and Aluru [139]	-	~0.470	0.333	Numerical
Tsai <i>et al.</i> [140]	0.310	0.358	0.34	Numerical
Present work	0.350-0.355	0.482-0.493	0.34	Numerical

Due to end effects, the Young's and shear moduli of a graphene layer are affected by the model size. For instance, a graphene layer having the model size of 27.07 Å x 41.20 Å has the Young's modulus of 1.032 TPa and shear modulus of 0.482 TPa. On the other hand, if the graphene layer has the model size of 962.4 Å x 1340.0 Å, then it has the Young's modulus of 1.047 TPa and shear modulus of 0.493 TPa. It is observed in Table 5.1 that calculated values of the tensile rigidity and shear moduli of SLGSs are in agreement with numerous experimental and numerical results in literature. The u_x and u_y displacement contours of the plane stress CM and MM models are shown in Fig 5.3 for the same tensile loading conditions. As can be seen in Fig 5.3, displacement contour plots are very similar and plane stress CM and MM models are almost equivalent. In addition, modal features of both models are found to be very similar. In sum, presented model can calculate the Young's modulus and Poisson's ratio accurately.

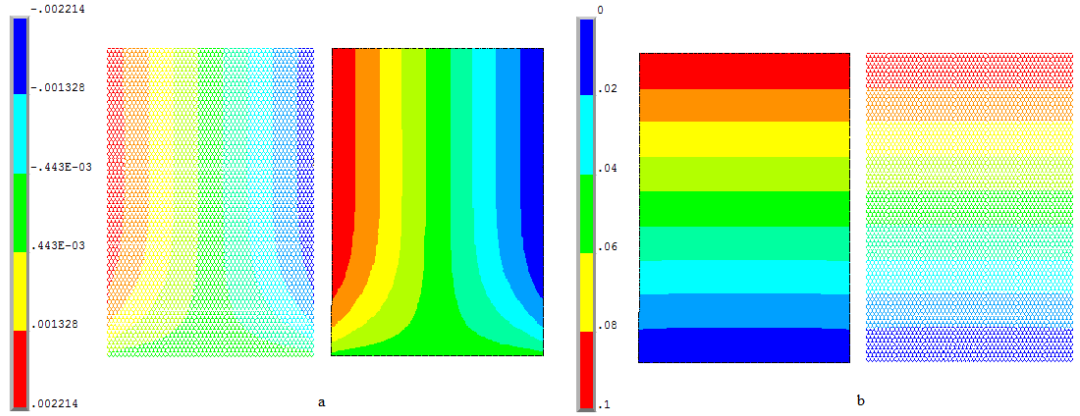


Figure 5.3: The displacement contours of the plane stress CM and MM models; (a) u_x component and (b) u_y component.

For the validation of the proposed CM/MM coupled formulation, further test problems are solved. To this end, the following error criteria ε_d is employed to determine the accuracy of the models in the atomistic domain

$$\varepsilon_d = \frac{\|\mathbf{d}^m - \mathbf{d}^a\|_2}{\|\mathbf{d}^a\|_2} \quad (5.31)$$

$$\|\mathbf{d}\|_2 = (\sum_j d_j^2)^{1/2} \quad (5.32)$$

where d^m and d^a are the vectors of atomic displacements calculated by coupled models and full atomistic models, respectively.

Following, in the second example on static loading, we considered that the MM domain overlaps with a CM element in the center of the CM domains. While the MM domain having the dimensions of $27.07 \text{ \AA} \times 41.20 \text{ \AA}$ is unchanged, three coupled CM/MM models having different CM element sizes are considered as shown in Figure 5.4. One end of the sample sheets is constrained and the other end is subjected to total initial displacement of 0.1 \AA in positive x- and/or y-directions (e.g., tensile and transverse directions). Both zigzag and armchair directional loading conditions are taken into account in analyses and total twelve validation tests are solved for the three coupled models shown in Figure 5.4.

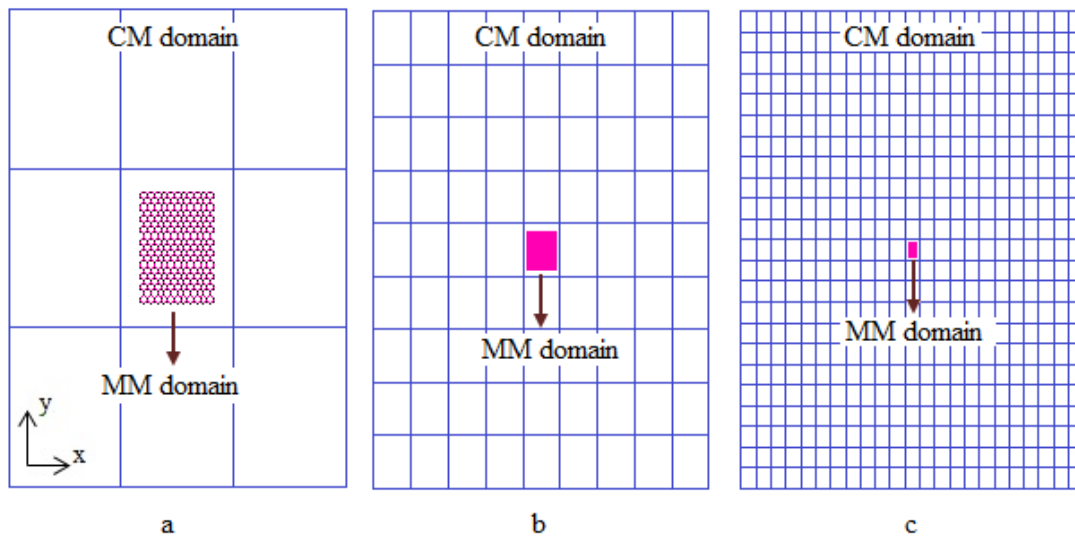


Figure 5.4: Coupled CM/MM models where the MM models are identical while the CM model changes as follows: (a) model #1, (b) model #2 and (c) model #3.

Table 5.2 shows the maximum displacement errors of some of these validation tests. It can be seen in Table 5.2 that the accuracy of the proposed coupled model is directly related to the element size in the plane stress CM domain. The differences between the displacements of the coupled CM/MM model and full atomistic models (i.e., relative error) are reduced by refinement of elements in the CM domain, while the dimensions of the MM domain are kept constant. It is concluded that sufficient

number of plane stress elements should be used in the CM domain to increase the accuracy of the solutions obtained by the CM/MM coupled formulation.

Table 5.2: Maximum displacement errors in the second numerical example on static loading.

CM/MM coupled model	# of atoms	# of nodes	# of atoms in full atomistic model	Width (Å)	Height (Å)	ε_d
Fig. a	460	16	8652	125.5	177.6	0.0229
Fig. b	460	100	77,364	376.5	535.7	0.0070
Fig. c	460	576	494,548	962.4	1340.0	0.0041

Figures 5.5 to 5.7 show the u_y displacement components at different atoms of the CM/MM coupled model shown in Figure 5.4b and full atomistic model. Both models are subjected to initial displacement of 0.1 Å in the positive y-direction (e.g., tensile direction).

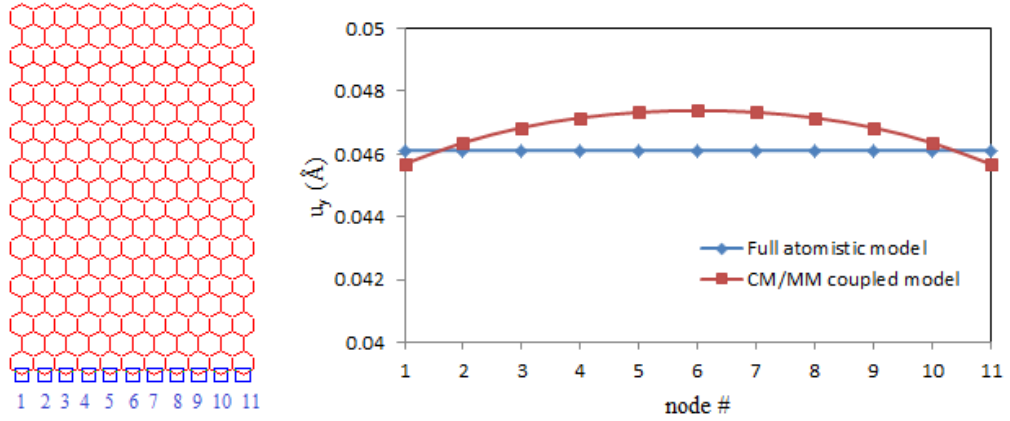


Figure 5.5: Displacement components u_y of the full atomistic and CM/MM coupled models at boundary nodes in the MM domain.

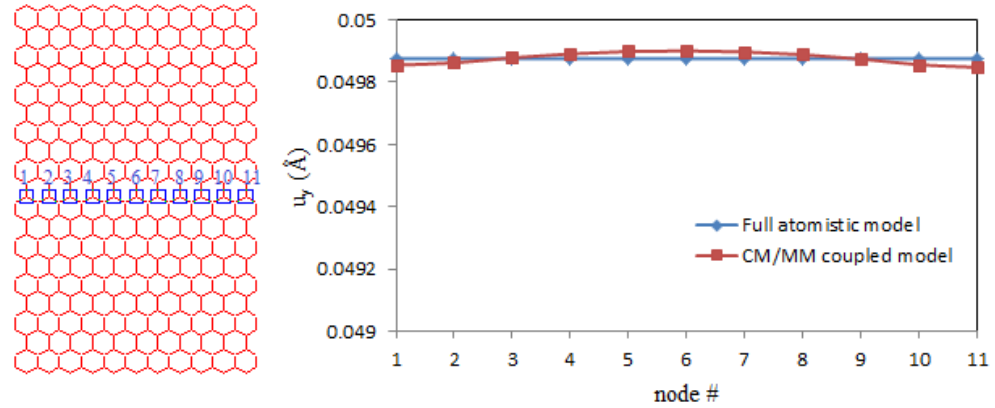


Figure 5.6: Displacement components u_y of the full atomistic and CM/MM coupled models in mid horizontal nodes in the MM domain.

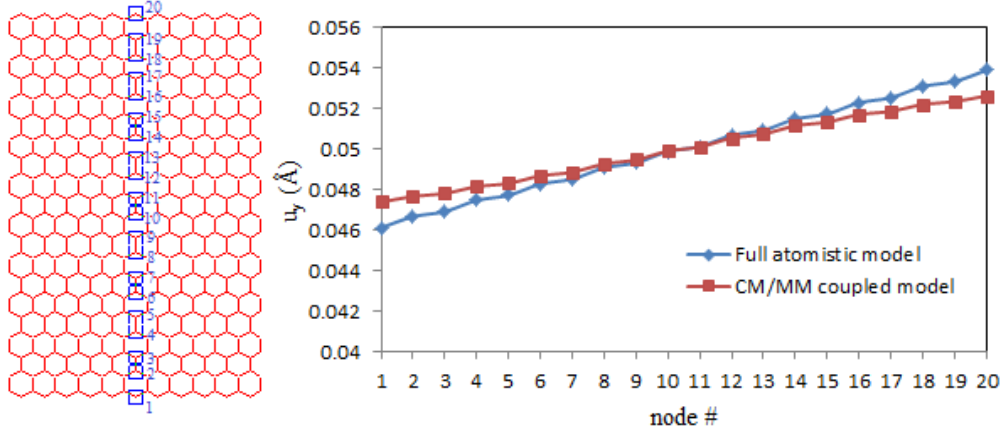


Figure 5.7: Displacement components u_y of the full atomistic and CM/MM coupled models in mid vertical nodes in the MM domain.

It is observed in Figures 5.5 to 5.7 that the largest displacement errors occur at boundary nodes and the displacement error goes to zero around the middle region of the atomistic domain that is expected due to least squares projections of atomistic and continuum displacement fields. Because the coupling strategy is based on least squares fit over the boundaries of the atomistic domain Γ^A . As a result, it is suggested in studying the defected graphene layers that the topological defects should be located in the middle region of the atomistic domain for the best accuracy in our approach. The relative error of solutions is in the range of 0.41% to 2.29% in comparison with full atomistic solutions depending on the element size of the CM domain, that is acceptable.

It is noteworthy that the plane stress CM element satisfies the FE patch test and can generate the constant strain displacement fields having any orientation. The CM/MM coupled formulation satisfies the patch test, since it depends on the least squares fit of the fine and course scale solutions.

5.2.2 Fracture analyses of defected SLGSs

In the first example on fracture mechanics, fracture analyses of defected SLGSs are completed by considering the CM/MM coupled model where the modified Morse potential and the CM model having the dimensions of $962.4 \text{ \AA} \times 1340.0 \text{ \AA}$ and 576

FE nodes are used. Mostly studied GS defects in literature are incomplete bonding defects such as vacancies and topological defects (i.e., the Stone-Wales (SW) transformation) [67]. Vacancy defects originate from missing atoms in the GSs and may occur due to an electron irradiation or oxidative purification. A non-reconstructed defected zigzag SLGSs is used in our study, and corresponding C-C bonds and carbon atoms are removed in the defect-free SLGSs (e.g. see Figure 5.8).

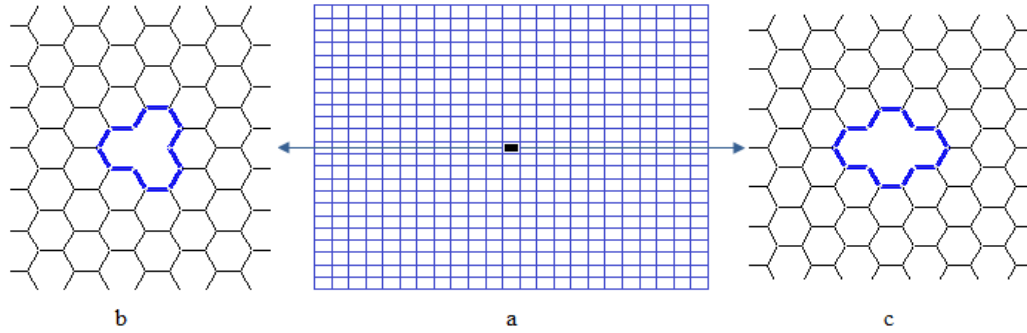


Figure 5.8: (a) The CM/MM coupled SLGS model, (b) one-atom vacancy defect, and (c) two-atoms vacancy defect.

Although metastable, the non-reconstructed configurations can be present at low temperatures and low dose irradiation [132, 133] and non-reconstructed defected SWCNTs are used in some works in literature [72, 85, 132]. Described by the modified Morse potential, the non-linear behavior of bonds is represented by using EB beam elements and an incremental loading procedure is followed similar to [85]. Initial Young's modulus of beam elements is obtained through the stress-strain curve of the C-C bond according to the modified Morse potential and the stress-strain curve of the C-C bond is shown in Figure 5.9.

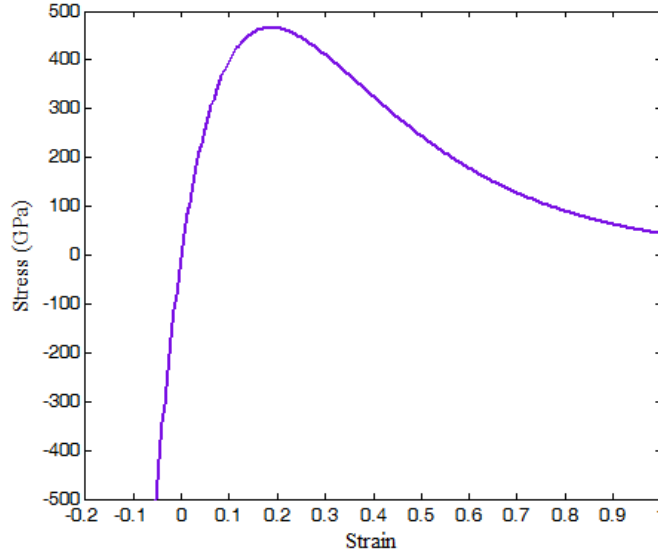


Figure 5.9: Stress-strain curve of the C-C bond.

In the analyses, all the nodes at one end of the graphene sheet are constrained, while the nodes at the other end are subjected to an incremental displacement. The Young's modulus of each element in the original SLGS structure is updated at each load step and it is set to $F/(A\varepsilon)$, where A is the cross sectional area of the element, ε axial strain of the element, and F the interatomic force calculated by Equation (4.14). Hence, by updating the elasticity parameters of the CM domain by using the MM solutions, nonlinear effects are considered. When the axial strain of a bond reaches the critical fracture strain, then its stiffness matrix is multiplied by a very small number to simulate the bond break. Values of the parameters in the modified Morse potential functions used in our study are the same as those in [72] where it is reported that the bond angle-bending potential does not contribute to the stretching energy and it has little effect on fracture in CNTs. Belytschko et al. [72] studied the fracture of CNTs by using the MM simulations and reported that the fracture is almost independent of the dissociation energy and depends primarily on the inflection point of the interatomic potential. After the inflection point, the shape of the potential function is not important since material damage occurs. A cut-off distance (r_{cf}) based on bond-breaking criterion is very often used in atomistic simulations, and the value of $r_{cf} = 0.169$ nm is employed which corresponds to the inflection point at approximate strain value of 19 % (i.e., the maximum of the interatomic force curve). The strain in SLGSs is calculated by $\varepsilon = (L - L_0)/L_0$ where L_0 and L are the initial (equilibrium) and current lengths of the sheet material, respectively. The stress is calculated by $\sigma = F_g/bt$ where F_g is the corresponding applied tensile force

computed by summation of the longitudinal reaction forces of the constrained nodes, and b and t are respectively the width and thickness of the sheet.

Table 5.3 summarizes the results obtained by the full atomistic and CM/MM coupled models. The fracture strain and stress values of coupled models are slightly larger than those of the full atomistic models. It is observed in Table 5.3 that fracture stresses of the SLGSs are reduced by 17.8 % and 20.7 % if one-atom and two-atoms vacancy defects exist in structures, respectively. This result also agrees with the MM calculations on CNTs reported in [72, 85].

Table 5.3: Results of the analysis of defected SLGSs.

Defect type	CM/MM stress (GPa)	CM/MM strain	Full atomistic stress (GPa)	Full atomistic strain
One-vacancy	77.1	0.087	78.6	0.085
Two-vacancies	76.1	0.086	75.8	0.084

In sum, the proposed approach is able to give the accurate prediction of fracture initiation and post failure behavior of SLGSs. The relative errors in fracture stress are less than 2% although relatively small number of atoms is selected in the MM model. However, the accuracy of predicting crack propagation in nanoscale is limited as the modified Morse potential function is not capable of describing the behavior of SLGSs after the C-C bonds are broken where the reconfiguration of bonds and structural transformations may occur. Note also that the same fracture initiation and crack propagation patterns are observed in both coupled and full atomistic simulations. Fig 5.10 shows the fracture initiation and crack propagation directions of the one-atom vacancy defected sheet models. As can be observed in Figure 5.10, the fracture initiated from the vertical bonds which is shown in dark colour in Figure 5.10a and propagated in the same row of bonds as expected. The same crack propagation characteristic is observed in studies on zigzag type CNTs in literature [72, 85] that justify the proposed CM/MM coupling approach.

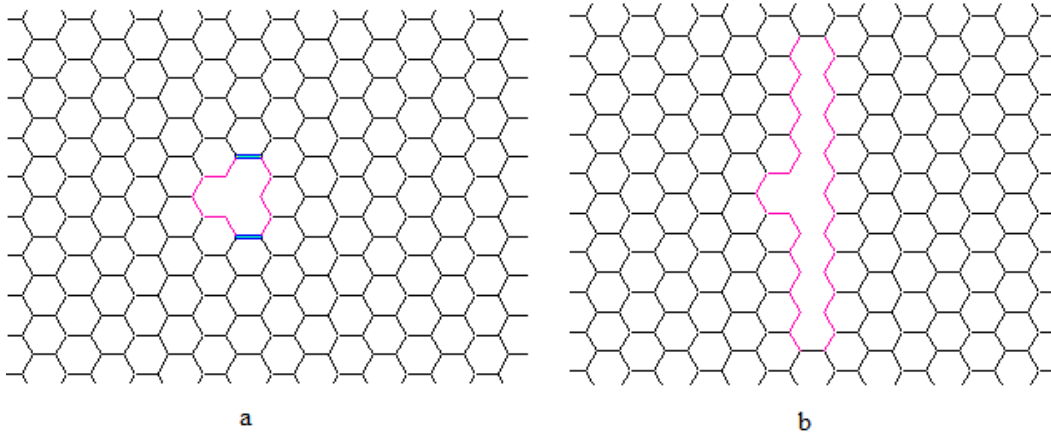


Figure 5.10: (a) Fracture initiation and (b) propagation directions of one-atom vacancy defected full atomistic and coupled models.

In the second example on fracture mechanics, a graphene layer with a central crack is considered; the MM/CM coupling scheme and elasticity formulas are used to determine the strain distribution along the crack direction in the layer. Figure 5.11 shows the atomistic sheet containing a crack in the center. The dimensions of the continuum and atomistic domains are $2262.75 \text{ \AA} \times 1136.00 \text{ \AA}$ and $310.11 \text{ \AA} \times 113.68 \text{ \AA}$, respectively. The atomistic domain is located in the middle of the CM domain and consists of 13662 atoms.

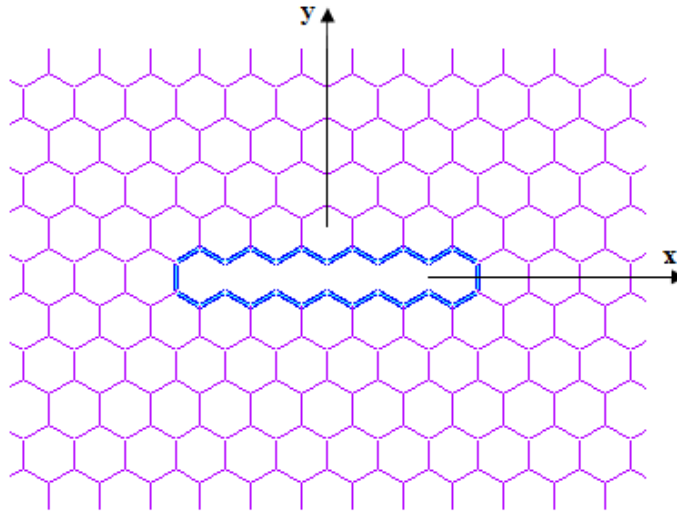


Figure 5.11: The atomistic sheet containing a crack in the center.

The crack is located in the middle of the MM domain, is perpendicular to vertical C-C bonds and the loading direction. The center crack is modeled by removing the C-C bonds to eliminate the interaction between atom pairs across the crack surface. The crack length of $2a=14.76 \text{ \AA}$ is considered in the simulations. The plane stress

loading is assumed for the CM domain. The atomistic displacement field is calculated from linear elastic fracture mechanics (LEFM) with initially specified stress intensity factor K_I . In fracture mechanics, the relative displacements between corresponding pairs of atoms separate symmetrically normal to the plane of the crack in the opening mode or mode 1. The linear elastic solution of the displacement fields in the vicinity of the crack tip in opening mode is given by [141]

$$u_x = \frac{K_I}{2\mu} \sqrt{\frac{r}{2\pi}} \cos \frac{\theta}{2} \left[(\kappa - 1) + 2 \sin^2 \frac{\theta}{2} \right] \quad (5.33)$$

$$u_y = \frac{K_I}{2\mu} \sqrt{\frac{r}{2\pi}} \sin \frac{\theta}{2} \left[(\kappa + 1) - 2 \cos^2 \frac{\theta}{2} \right] \quad (5.34)$$

where u_x and u_y are the displacements in the x and y directions, respectively, K_I is the stress intensity factor, μ is the shear modulus of the material, $\kappa = (3 - \nu)/(1 + \nu)$ for plane stress, r and θ are the cylindrical coordinates measured from crack tip and ν is the Poisson's ratio. The stress intensity parameter K_I for a finite width plate is given by [141]

$$K_I = \sigma \sqrt{\pi a} \left[\sec \frac{\pi a}{w} \right]^{1/2} \quad (5.35)$$

where σ is the gross stress, a is the half-length of crack and w is the width of plate. The strain distribution in front of the crack is calculated at the prescribed gross strain of $\varepsilon_{yy} = 1\%$. Fig 5.12 shows the deformed and undeformed configurations of atoms around the crack tip, where the solid and dashed lines refer to the deformed and undeformed configurations, respectively.

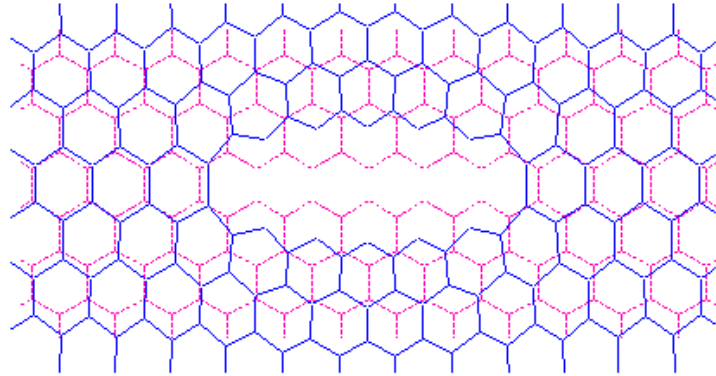


Figure 5.12: The deformed and undeformed configurations of atoms around the crack tip.

Figure 5.13 shows the strain results obtained by the elasticity solution and CM/MM coupled model. As can be seen in Figure 5.13, the CM/MM coupled model yields results that are consistent with linear elastic solution and also in agreement with the strain results of bridging domain method [106]. It is concluded that the proposed approach is able to predict the strain distribution near the crack tip accurately.

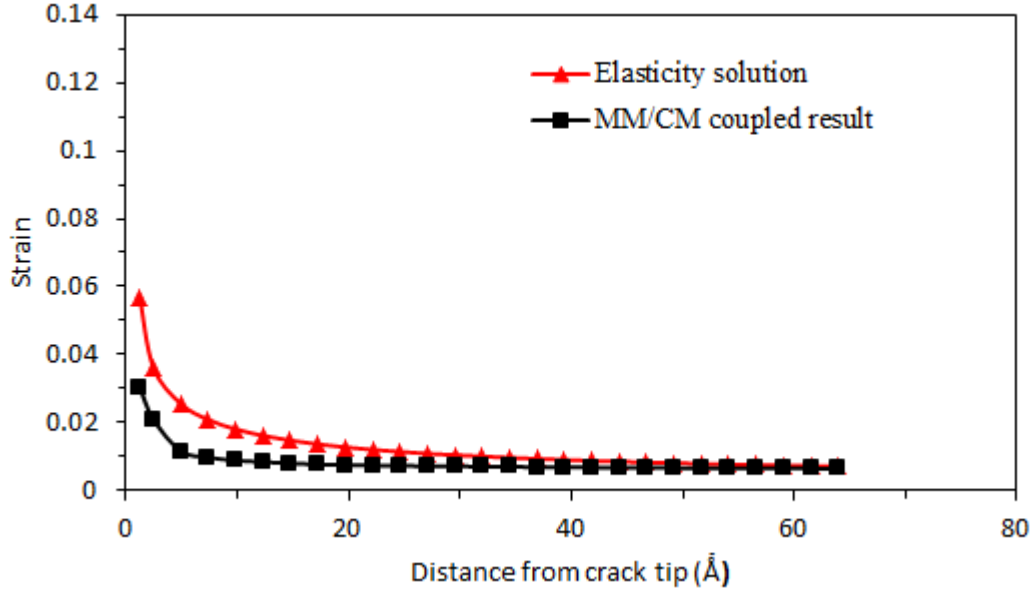


Figure 5.13: The strain results obtained by the elasticity solution and CM/MM coupled model.

In the third example on fracture mechanics, the effect of slit defects on the strength of SLGSs is examined. The MM/CM coupling scheme and Griffith's formula are used to determine fracture stresses of SLGSs with slit defects of various lengths. Cracks or slit defects are modeled by artificially removing a single row of bonds or elements in the MM model [77] (e.g., see Figure 5.11). To compare with the results of an infinite sheet, the model dimensions are selected as $962.4 \text{ Å} \times 1340 \text{ Å}$. The atomistic domain has the dimensions of $81.2 \text{ Å} \times 126.4 \text{ Å}$ and located in the center of the SLGSs. The Griffith's theory [142] can be used for brittle and linear elastic materials to predict a rigorous lower bound for the fracture stress as a function of crack length. According to the Griffith's theory, the critical stress for the propagation of a central crack in a thin and infinitely large sheet is given by [141]

$$\sigma_f = \sqrt{\frac{2E\gamma}{\pi a}} \quad (5.36)$$

where σ_f is the Griffith's formula for critical stress, E is the Young's modulus of sheet, γ is the surface energy density, and a is the half length of the slit. The surface energy density γ is chosen to be 4.2 J m^{-2} due to [143].

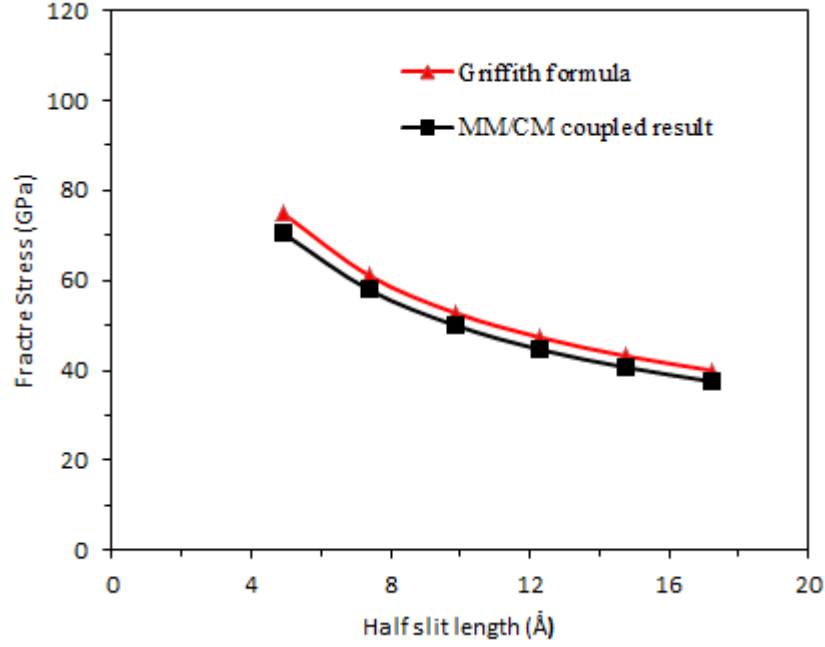


Figure 5.14: The fracture strength values obtained by the coupled MM/CM model and Griffith's formula for a graphene sheet having a slit defect.

To calculate the fracture stresses of SLGSs containing slit-like defects, an incremental displacement is applied to the edges of the coupled model in the direction perpendicular to the zigzag edge until the fracture of the sheet. Figure 5.14 shows the fracture strength of the coupled CM/MM model and results of the Griffith's formula for SLGSs containing slit-like defects. As can be seen in Figure 5.14, the results of the coupled MM/CM model agree well with the prediction of the Griffith's formula. In brief, results of the coupled model are approximately 6% smaller than those of the Griffith's formula and both show similar trend for cracks having different sizes that reduce approximately as the inverse of the square root of the crack length. Note that Khare et al. [77] also obtained similar results by using a QM/MM/CM coupled method, where fracture stresses for defective SLGSs are found to be in good agreement with the Griffith formula for defects as small as 10 Å . In addition, Mattoni et al. [144] found also good agreement between the MM calculations and Griffith's formula on SiC. Consequently, the good agreement

between the results of the proposed MM/CM coupled model and Griffith's formula imply that the Griffith's formula is applicable to nanoscale fracture problems.

6. VIBRATION AND ELASTIC BUCKLING ANALYSES OF CARBON NANOCONES (CNCs)

This section reports the result on elastic buckling and vibration behaviors of single-walled carbon nanocones (SWCNCs) having the potential usage in atomic force microscope (AFM) and scanning tunneling microscope (STM) tips. The modeling work employs the MM based FE approach in which Euler-Bernoulli beam element formulations are used with consistent mass matrix which is mentioned in Section 3. Equivalent density parameter for the beam elements in the MM model is obtained by using the equivalency of natural frequencies of continuum plane stress FE model of SLGSs and those of the MM model which mentioned in Section 4. Free-free, free-clamped and clamped-clamped boundary conditions are considered in vibration analysis of SWCNCs; on the other hand, axial compression and bending loading conditions are taken into account in elastic buckling behavior of SWCNCs. The effects of cone height and disclination or apex angles on the buckling force and natural frequencies of SWCNCs are investigated. In all analyses, the disclination angles of 120° , 180° and 240° are used while the cone height is varying.

6.1. Structures of SWCNCs

Figure 6.1 shows the cone sheet with the dislocation angle of 120° , 180° and 240° , and Figure 6.2 shows the corresponding to the cone with apex angle of 83.6° , 60° and 38.9° SWCNC with cone height of 15 \AA . The larger the apex angle of a SWCNC, the larger the bottom radii and number of atoms.

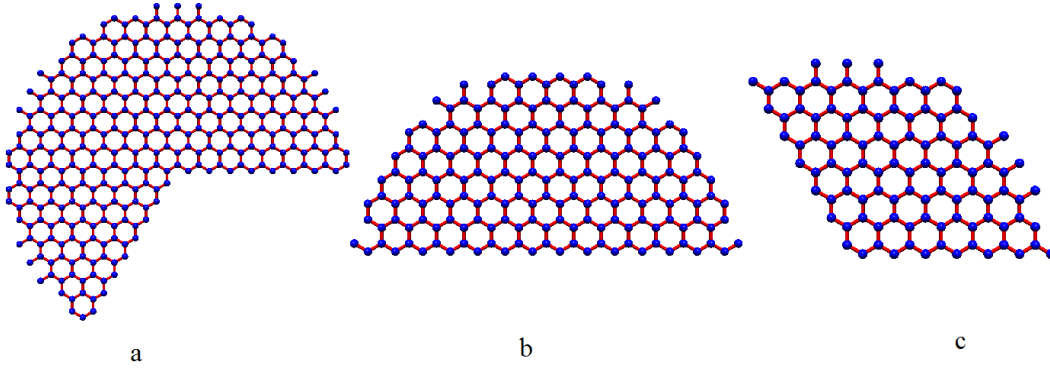


Figure 6.1: Cone sheets with cone heights of 15 Å with a) disclination angles of 120°, b) disclination angles of 180°, c) disclination angles of 240°.

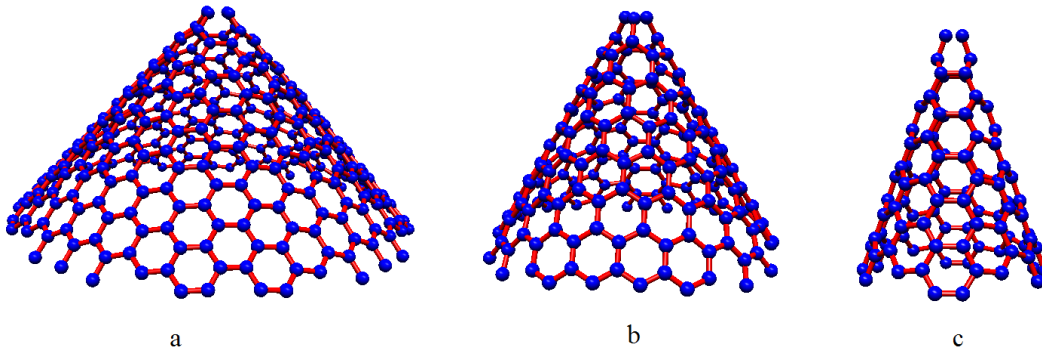


Figure 6.2: SWCNCs with cone heights of 15 Å with a) apex angle of 83.6°, b) apex angle of 60° c) apex angle of 38.9°.

6.3. Vibrational and Elastic Buckling Analyses of SWCNCs

In this thesis, SWCNCs with disclination angles of 120°, 180° and 240° are taken into account which satisfied the continuity condition at the folding of the cone sheet. The tip of the SWCNCs is not explicitly modeled in vibrational and buckling analysis due to geometric limitations (e.g., see Figure 6.2). The smallest model has 180 atoms and 258 bonds, while the largest model has 3592 atoms and 5312 bonds.

Figure 6.3 shows the boundary and loading conditions for vibrational and buckling analyses of the SWCNCs. All computations of the MM model are completed by using a computer code developed in MATLAB environment, no damping is considered in computational models and the results are verified by using Ansys ® software.

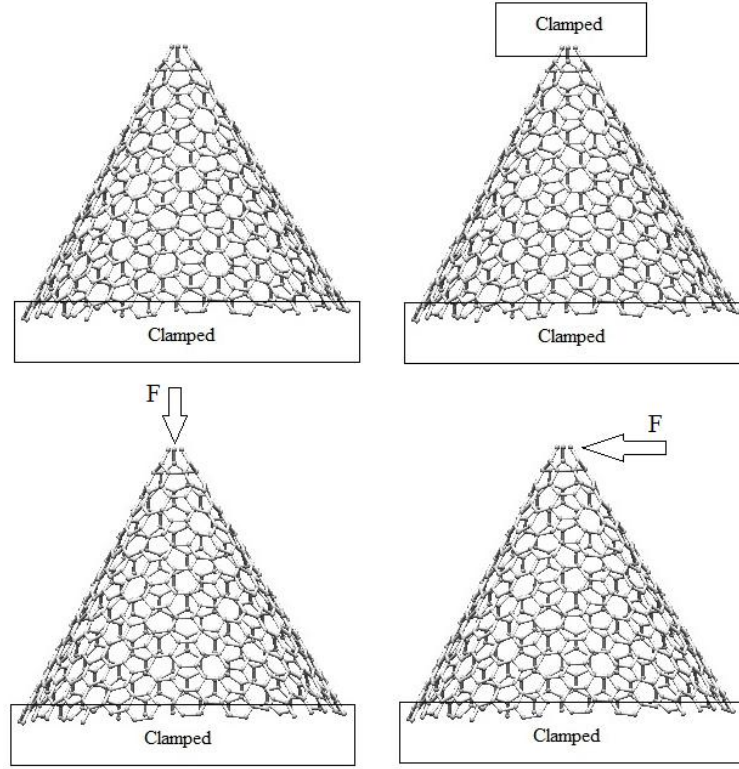


Figure 6.3: Free-clamped and clamped-clamped boundary conditions in vibrational analysis (upper) and axial compression and bending loading conditions in buckling analysis (below).

After assembling the element stiffness and consistent mass matrices, the natural frequencies and corresponding mode-shapes are obtained by solving the following eigenproblem

$$(\mathbf{K} - \omega_i^2 \mathbf{M})\mathbf{d} = \mathbf{0} \quad (6.1)$$

Similarly, critical buckling load and corresponding mode shapes are calculated by solving the following eigenproblem

$$(\mathbf{K}_0 - \lambda \bar{\mathbf{K}}_1)\boldsymbol{\psi} = \mathbf{0} \quad (6.2)$$

where \mathbf{K}_0 is the global stiffness matrix, $\bar{\mathbf{K}}_1$ is the geometric stiffness matrix and $\boldsymbol{\psi}$ is the buckling-mode shape vector. The factor λ at which buckling occurs is designated as λ_{cr} , and $P_{cr} = \lambda_{cr}P$ [130].

Table 6.1: Properties of the beam elements.

	Present work	Lee and Lee [43]
Mass matrix type	Consistent	Lumped
Beam type	Euler-Bernoulli	Shear Beam
Cross-sectional area, A	1.687 \AA^2	1.687 \AA^2
Density [22]	$5.5 \times 10^{-27} \text{ kg/ \AA}^3$	$2.3 \times 10^{-27} \text{ kg/ \AA}^3$
Elastic modulus, E	$5.488 \times 10^{-8} \text{ N/\AA}^2$	$5.488 \times 10^{-8} \text{ N/\AA}^2$
Shear modulus, G	$8.711 \times 10^{-9} \text{ N/\AA}^2$	$8.711 \times 10^{-9} \text{ N/\AA}^2$
Poisson's ratio, ν	Not needed	0.3
Bond thickness, d	1.47 \AA	1.47 \AA

The effects of cone height and disclination angles on the natural frequencies of SWCNCs are examined in vibration analysis where natural frequencies and corresponding mode shapes are obtained. Figures 6.4, 6.5 and 6.6 show the variations of the first fundamental frequencies of SWCNCs versus cone height for free-free, free-clamped and clamped-clamped boundary conditions, respectively. As can be seen in these figures, the first natural frequency decreases with increasing cone height in all types of SWCNCs, whereas it increases as the disclination angle increases except for the SWCNCs having the disclination angle of 240° and height of 20 \AA . In addition, the SWCNCs with disclination angles of 240° are more sensitive to variations in height and boundary conditions than the other SWCNCs in vibrational analysis due its small apex angle. When free-clamped and clamped-clamped boundary conditions are considered, the first fundamental frequencies of SWCNCs, are found to be in the range of $0.36\text{--}2.52 \text{ THz}$.

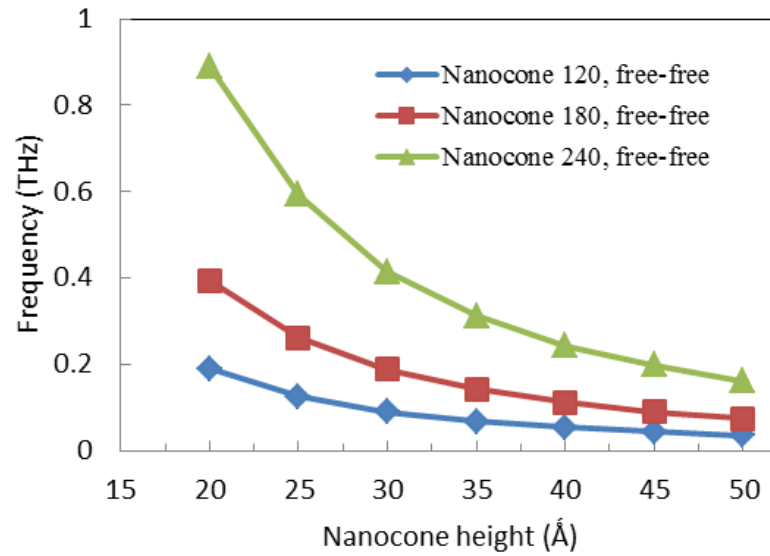


Figure 6.4: Variation of the first natural frequency of SWCNCs having the disclination angles of 120° , 180° and 240° as the cone height changes for the free-clamped boundary condition.

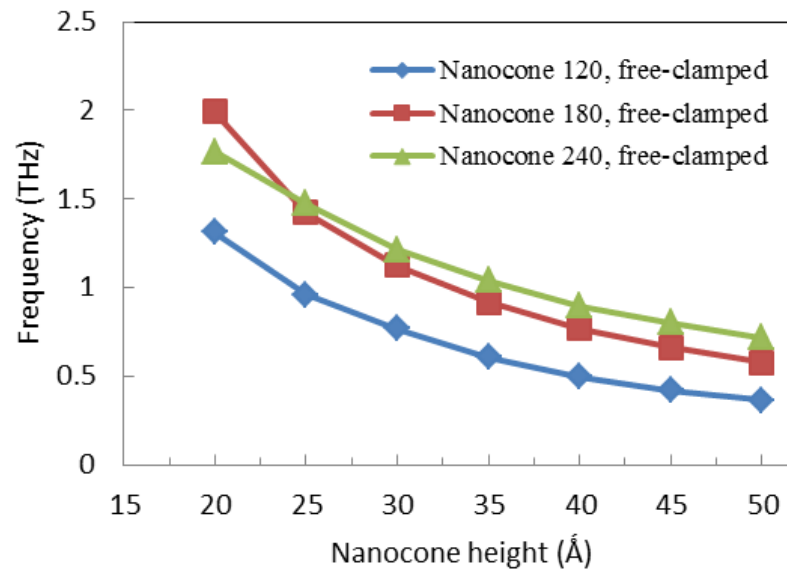


Figure 6.5: Variation of the first natural frequency of SWCNCs having the disclination angles of 120° , 180° and 240° as the cone height changes for the free-clamped boundary condition.

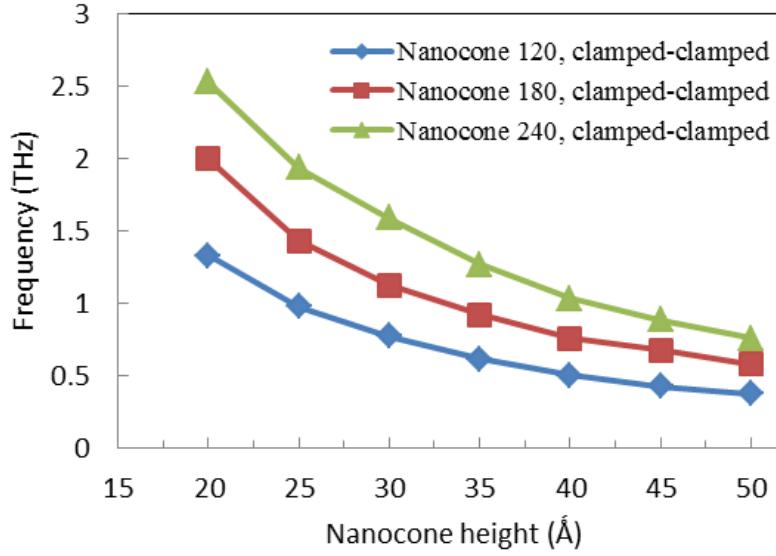


Figure 6.6: Variation of the first natural frequency of SWCNCs having the disclination angles of 120° , 180° and 240° as the cone height changes for the clamped-clamped boundary condition

Lee and Lee [43] used Timoshenko beam element formulations which include shear deformation effects but they employed Euler-Bernoulli beam element constants (i.e., see Table 6.1) [37]; this assumption affects the natural frequencies of SWCNCs that are found to be lower than those of Euler-Bernoulli beam elements. In addition, density of beam elements is selected to be the density of SWCNCs (i.e. 2300 kg/m^3) in the MM model. Hence, natural frequencies of SWCNCs are found to be less than 100GHz in all calculations for the same type of SWCNCs having the height of 20 \AA and with free-clamped and clamped-clamped boundary conditions. These frequency ranges are comparable with those of CNTs and SLGSs (i.e., 10 GHz – 1.5 THz for SWCNTs and 2.4 GHz – 3.5 THz for SLGSs) which are reported in literature [36, 39].

Figures 6.7 and 6.8 show respectively the variations in the first ten natural frequencies for the free-free and clamped-clamped SWCNCs having the height of 50 \AA and disclination angles of 120° , 180° and 240° . It is noteworthy that variations in the first ten natural frequencies for the free-clamped SWCNCs which are not presented here for limited space are very close to those of clamped-clamped boundary conditions since relatively small radius of the cone tips has little effect on the vibrational behavior of the SWCNCs for these two boundary conditions.

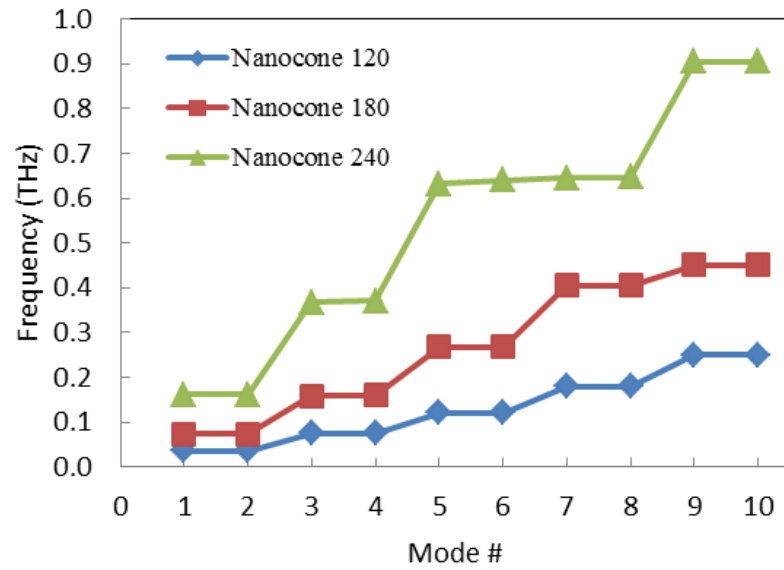


Figure 6.7: First ten natural frequencies of SWCNTs having the height of 50 Å and disclination angles of 120°, 180° and 240° for free-free boundary condition.

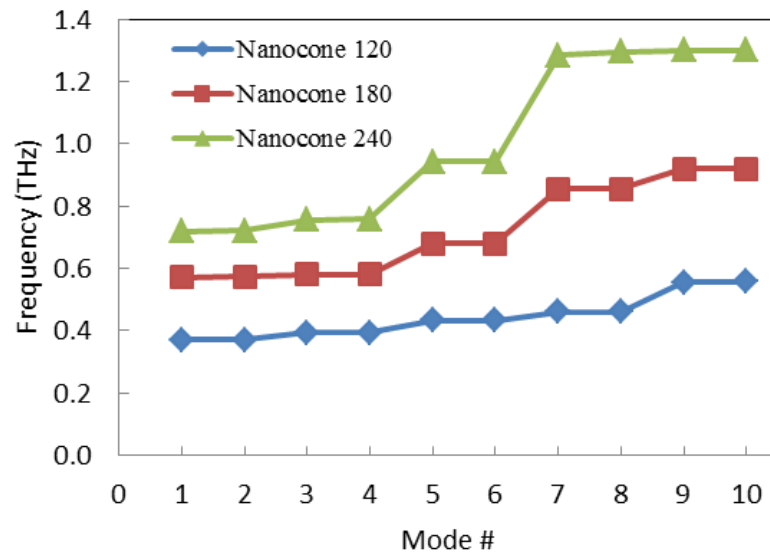


Figure 6.8: First ten natural frequencies of SWCNTs having the height of 50 Å and disclination angles of 120°, 180° and 240° for clamped-clamped boundary condition.

Figures 6.9 and 6.10 show respectively the first five vibration modes of SWCNCs having the disclination angle of 120° and height of 30 \AA for the free-free and free-clamped boundary conditions. The mode shapes of clamped-clamped SWCNCs are also similar to those of free-clamped SWCNCs, that are not presented here for limited space. In addition, the second mode shape is very similar to the first mode shape in both figures, that are not presented for limited space as well.

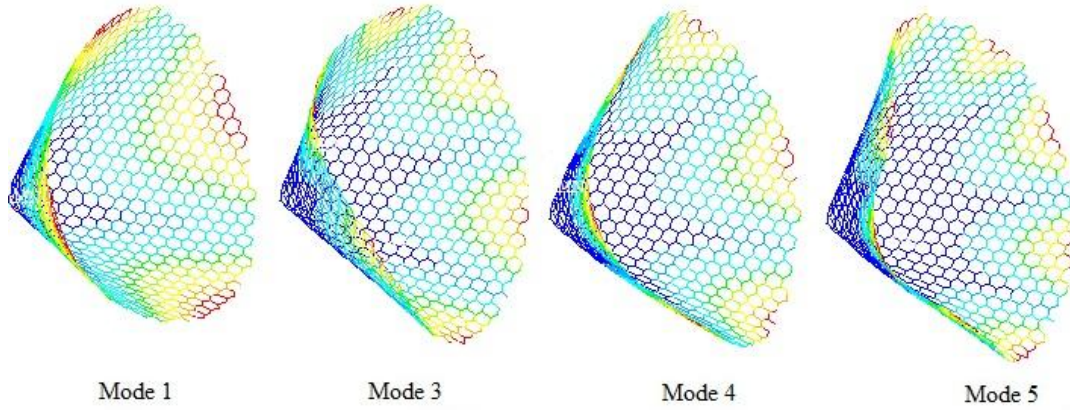


Figure 6.9: Vibrational modes of SWCNC having the disclination angle of 120° , height of 30 \AA for free-free boundary condition.

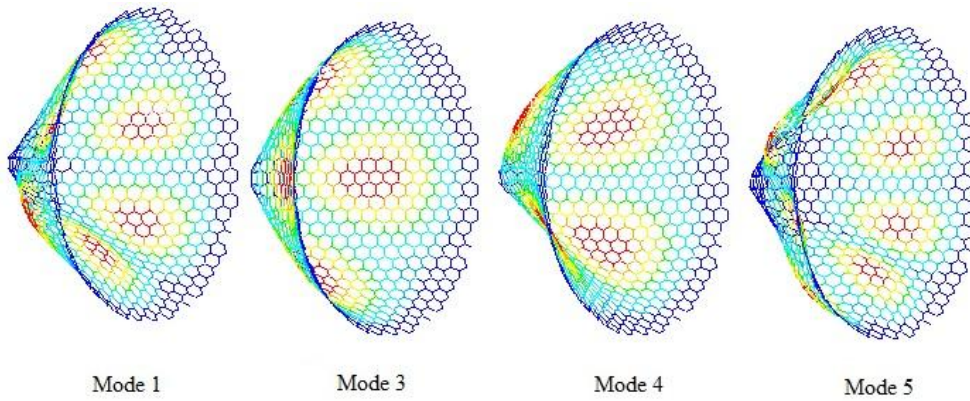


Figure 6.10: Vibrational modes of SWCNC SWCNC having the disclination angle of 120° , height of 30 \AA for free-clamped boundary condition.

Similar to vibration analysis, effects of cone height and disclination angles on the critical buckling load and associated buckling modes of SWCNCs are studied by completing elastic buckling analysis. Figures 6.11 and 6.12 show respectively the variations of the first critical buckling load of SWCNCs as the cone height changes for the axial and bending loading conditions. Buckling analysis results indicate that

as the disclination angle increases, the critical buckling load increases in axial compression loading and decreases in bending loading. The buckling load in axial compression is larger than bending load for SWCNCs having the disclination angles of 180° and 240° , and it is smaller than that of bending load for SWCNCs having the disclination angle of 120° . Hence, it is concluded that bending loading is more critical than axial compression loading for buckling behavior of SWCNCs as the disclination angle increases. In addition, the cone height affects the bending buckling forces more than the axial compression buckling forces. The axial and bending buckling forces are found to be in the range of 42 – 79 nN and 27 – 64 nN, respectively. These ranges are comparable with those of CNTs (i.e., ~0.1– 39 nN) which are reported in literature [59].

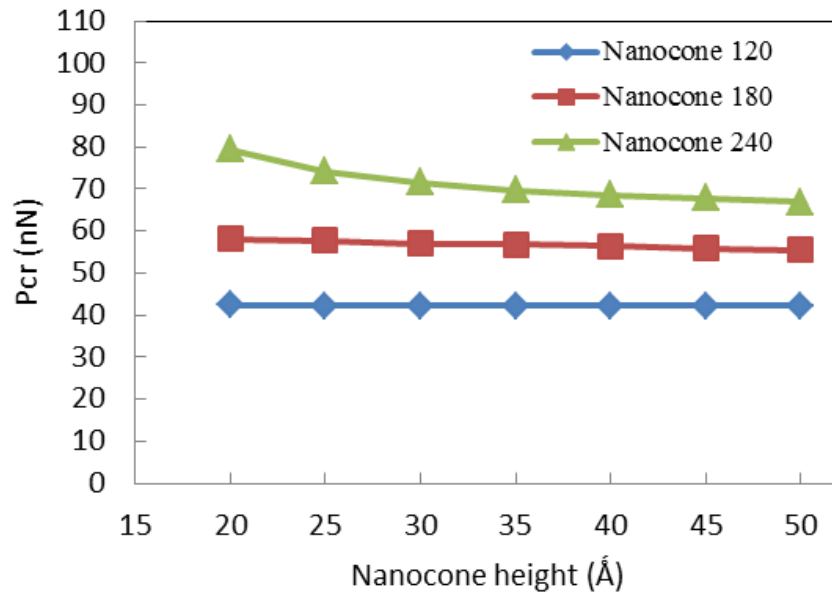


Figure 6.11: Variation of the first critical buckling load for the SWCNCs having the disclination angles of 120° , 180° and 240° as the cone height changes under axial compression loading condition.

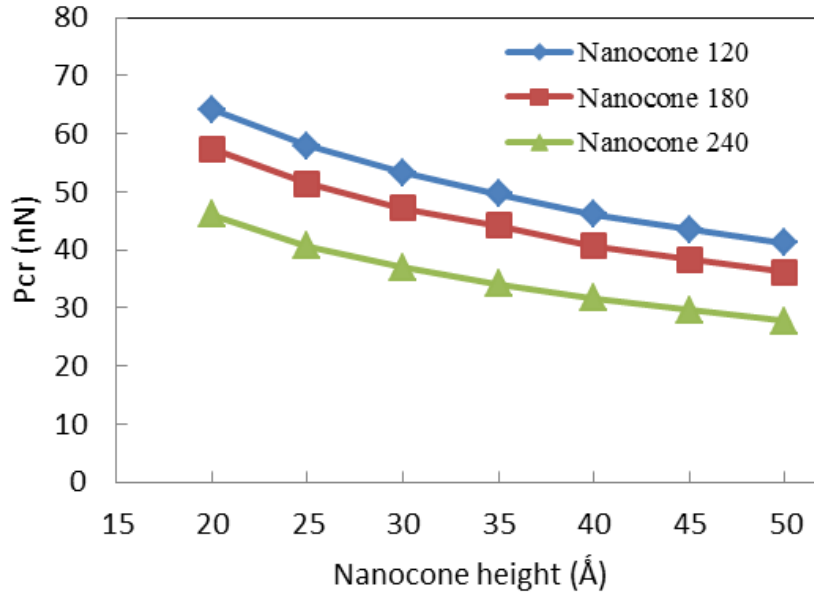


Figure 6.12: Variation of the first critical buckling load for the SWCNCs having the disclination angles of 120° , 180° and 240° as the cone height changes under bending loading condition.

Figures 6.13 and 6.14 show the first ten buckling loads for the SWCNCs having the height of 50 \AA . As can be seen the figures, the elastic buckling modes of the SWCNCs have similar pattern except for the SWCNC with the disclination angle of 240° under axial compression loading.

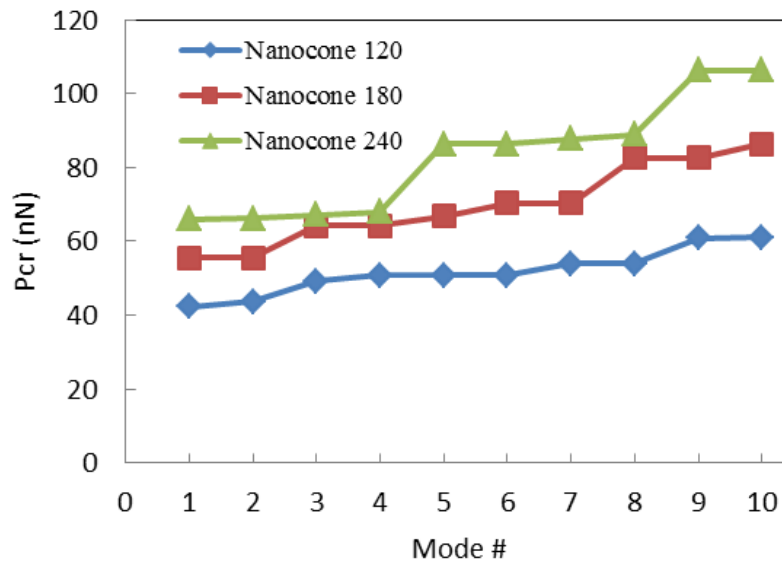


Figure 6.13: First ten buckling mode of SWCNCs having the disclination angles of 120° , 180° and 240° , and height of 50 \AA for the axial loading .

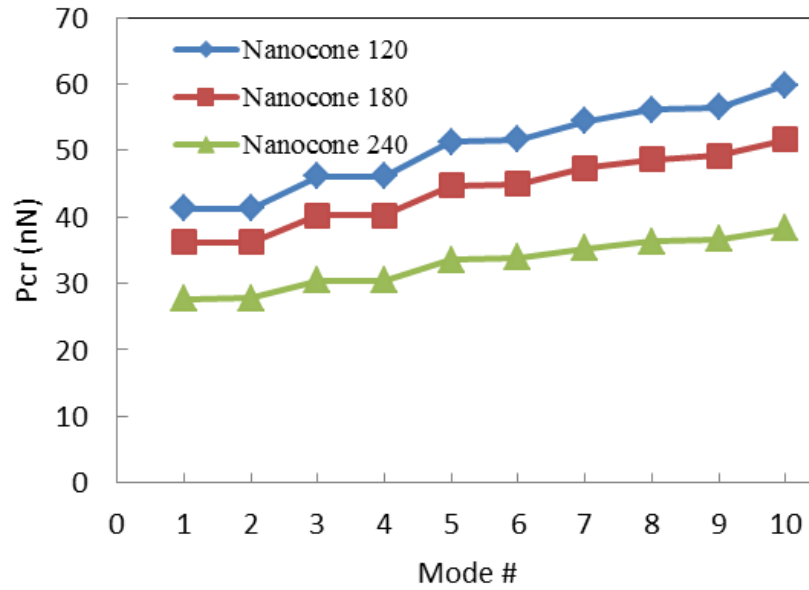


Figure 6.14: First ten buckling mode of SWCNTs having the disclination angles of 120°, 180° and 240, and height of 50 Å for the bending loading.

Figures 6.15 and 6.16 show respectively the first six buckling modes of the SWCNTs with the disclination angle of 240° and height of 50 Å under the axial compression and bending loading conditions. Since the second and fifth buckling modes are respectively very similar to the first and sixth buckling modes, they are not presented here for limited space.

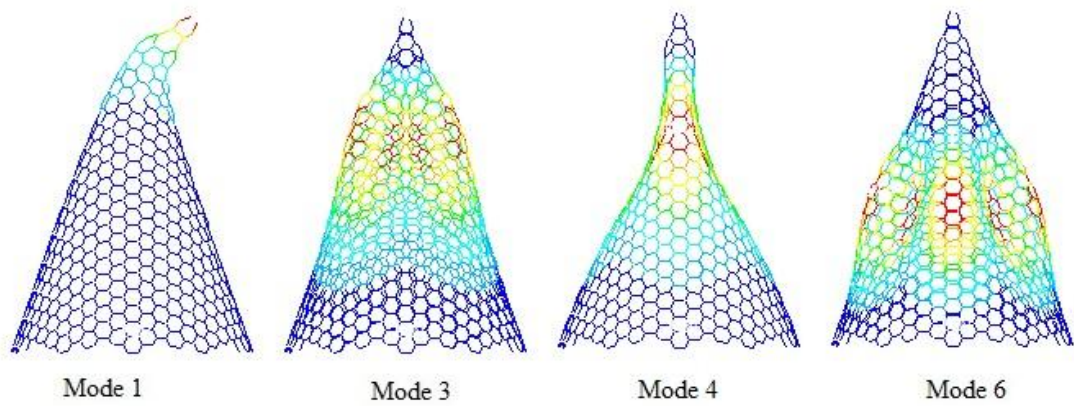


Figure 6.15: The first six buckling modes of the SWCNT having the disclination angle of 240° under the axial compression loading.

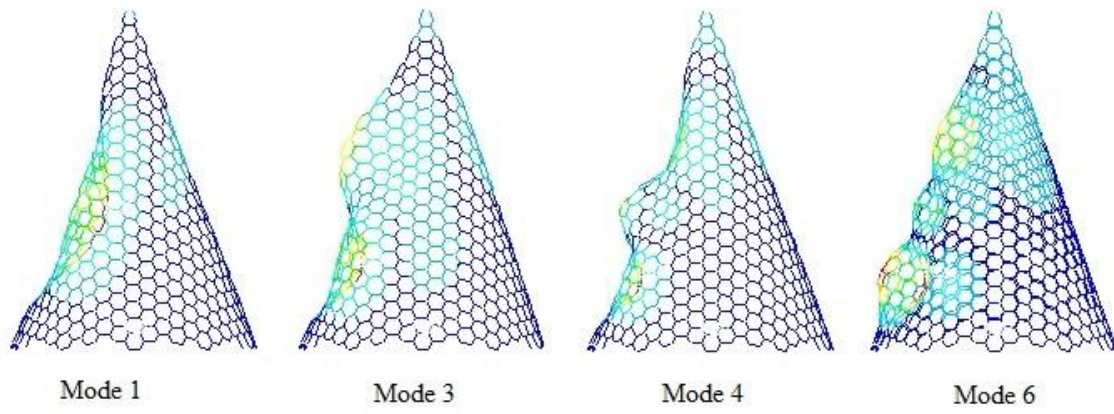


Figure 6.16: The first six buckling modes of the SWCNC having the disclination angle of 240° under the bending loading.

7. CHARACTERIZATION AND FRACTURE ANALYSIS OF CARBON NANOTUBES (CNTs)

This section reports the results on mechanical properties of SWCNTs such as axial Young's modulus, Poisson's ratio, shear modulus, elastic buckling loads and natural frequencies. The modeling work employs the MM based FE approach which is mentioned in Sections 3 and 4. Table 6.1 summarizes the geometric and material properties of the beam element which are the inputs of the FE models in this section. Armchair and zigzag SWCNTs are considered in analyses. All computations of the MM model are completed by using a computer code developed in MATLAB environment.

7.1. Axial Young's Modulus of SWCNTs

To calculate the Young's modulus E , symmetry boundary conditions are applied to all the nodes on one edge and the nodes on the opposite edge are uniformly loaded. Figure 7.1 shows the SWCNTs along with the applied boundary conditions.

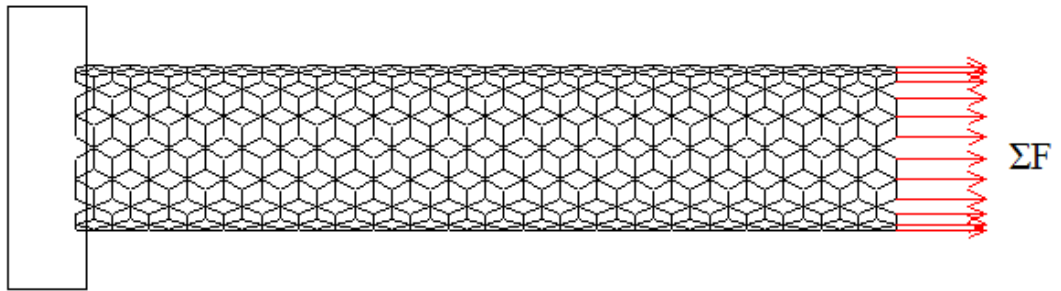


Figure 7.1: SWCNTs (8,8) along with the applied boundary conditions.

All load vector calculations are based on consistent load formulations and equivalent nanotube Young's modulus is evaluated with the following equation

$$E = \frac{\sigma}{\varepsilon} = \frac{FL_0}{A_0 \Delta L} \quad (7.1)$$

where F is the total applied force on the atoms at one end of the graphene sheet, A_0 is the cross-sectional area which is equal to πDt (where D and t are the mean diameter and thickness of the nanotube, respectively), L_0 is the initial nanotube length, ΔL is changes in the length of the SWCNTs. In Young's modulus calculations, the nominal thicknesses of 0.34 nm and 0.147 nm are considered for the SWCNTs. Figure 7.2 shows the variation of Young's modulus of armchair and zigzag SWCNTs with tube diameter. The calculated Young's modulus ranges from about 1.033 TPa to 1.038 TPa for the armchair type and ranges from about 1.004 TPa to 1.042 TPa for the zigzag type with the thickness of 3.4 Å. Tube lengths are equal to 41.2 Å and nominal thicknesses of the both SWCNTs are considered as 3.4 Å in Figure 7.2. As can be seen in Figure 7.2, the axial Young's modulus of both armchair and zigzag SLCANTs increase with an increasing in diameter and attain a stable value with increasing diameter for the SWCNTs.

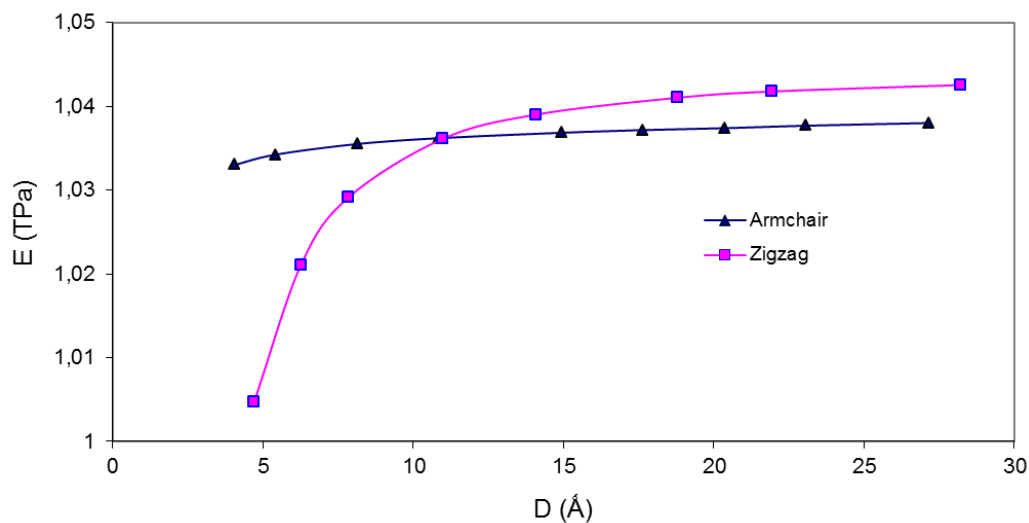


Figure 7.2: Variation of Young's modulus of armchair and zigzag SWCNTs with tube diameter. The nominal thicknesses of the both SWCNTs are 3.4 Å.

Figure 7.3 shows the variation of Young's modulus of armchair and zigzag SWCNTs with tube diameter. Tube lengths are equal to 41.2 Å and nominal thicknesses of the SWCNTs are considered as 1.47 Å and 3.4 Å in Figure 8.3. As can be seen in Figure 7.3, nominal or wall thickness of SWCNTs significantly affects the Young's modulus of SWCNTs. The smaller the thickness is, the larger the calculated Young's modulus is.

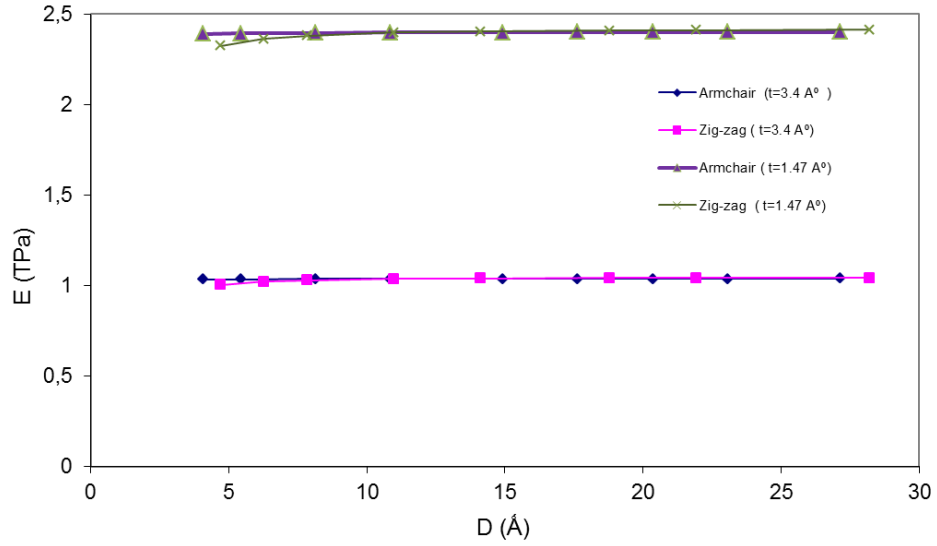


Figure 7.3: Variation of the Young's modulus of armchair and zigzag SWCNTs with tube diameter and nominal thickness.

7.2. Shear Modulus of SWCNTs

To calculate the shear modulus G , one end of the SWCNTs is subjected to a torsional moment and the nodes on the opposite edge are constrained. Figure 7.4 shows the SWCNTs along with the applied boundary conditions. Equivalent nanotube Young's modulus is evaluated with the following equation

$$G = \frac{TL_0}{\theta J_0} \quad (7.2)$$

where T is the torque acting at the end of SWCNTs (i.e., see Figure 7.4), L_0 is the initial nanotube length, θ is the torsional angle and J_0 is the cross-sectional polar inertia of SWCNTs. For calculating J_0 , SWCNTs are considered as a hollow tube with the diameter D and thickness t . In this case, cross-sectional polar inertia of SWCNTs can be calculated as follows

$$J_0 = \left(\frac{\pi}{32} \right) \left[(D+t)^4 - (D-t)^4 \right] \quad (7.3)$$

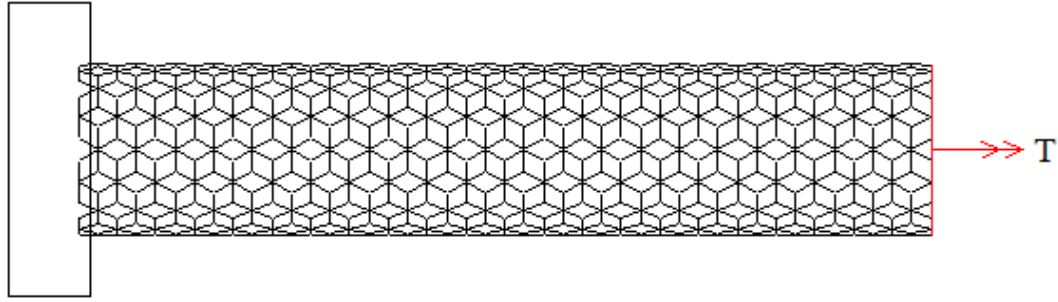


Figure 7.4: SWCNTs (8,8) along with the applied boundary conditions.

Figure 7.5 shows the variation of shear modulus of armchair and zigzag SWCNTs with tube diameter. Tube lengths are equal to 41.2 \AA and nominal thicknesses of the SWCNTs are considered as 1.47 \AA and 3.4 \AA in Figure 7.5. As can be seen in Figure 7.5, the nominal or wall thickness of SWCNTs significantly affects the shear modulus of SWCNTs. The smaller the thickness is, the larger the calculated shear modulus is. The calculated shear modulus ranges from about 0.267 TPa to 0.484 TPa for the armchair type and ranges from about 0.327 TPa to 0.481 TPa for the zigzag type with the thickness of 3.4 \AA . As can be seen in Figure 7.5, the shear modulus of both armchair and zigzag SWCNTs increase with an increasing diameter and attain a stable value with increasing diameter for the SWCNTs.

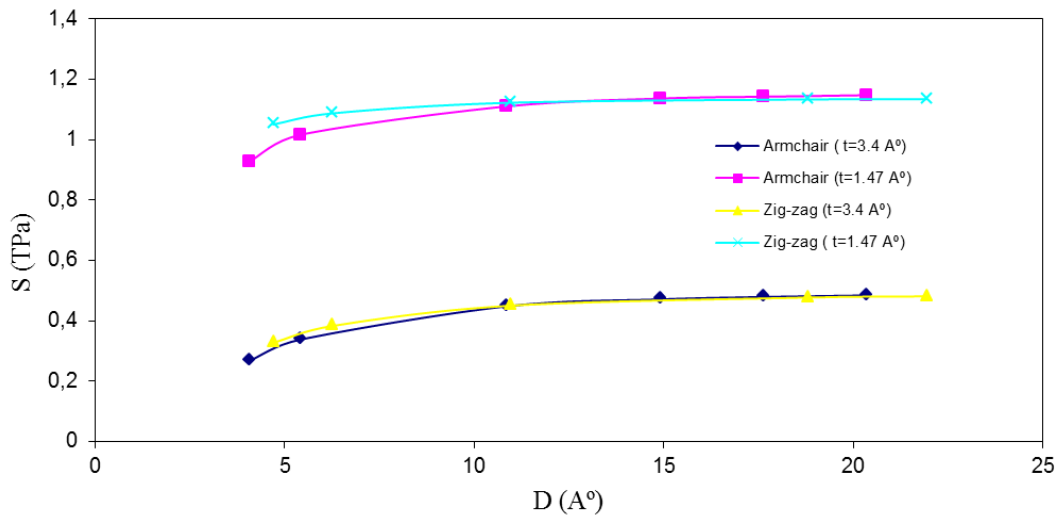


Figure 7.5: Variation of shear modulus of armchair and zigzag SWCNTs with tube diameter and nominal thickness.

7.3. Vibration Analysis of SWCNTs

For determining the natural frequencies of SWCNTs, we consider its equivalent space frame like structures under the free-free, clamped-free and clamped-clamped boundary conditions. The modeling work employs the MM based FE approach in which Euler-Bernoulli beam element formulations are used with consistent mass matrix which is mentioned in Section 3. Equivalent density parameter for the beam elements in the MM model is obtained by using the equivalency of natural frequencies of continuum plane stress FE model of SLGSs and those of the MM model which mentioned in Section 4. Figure 7.6 shows the boundary and loading conditions for vibrational analyses of the SWCNTs. All computations of the MM model are completed by using a computer code developed in MATLAB environment, no damping is considered in computational models and the results are verified by using Ansys ® software.

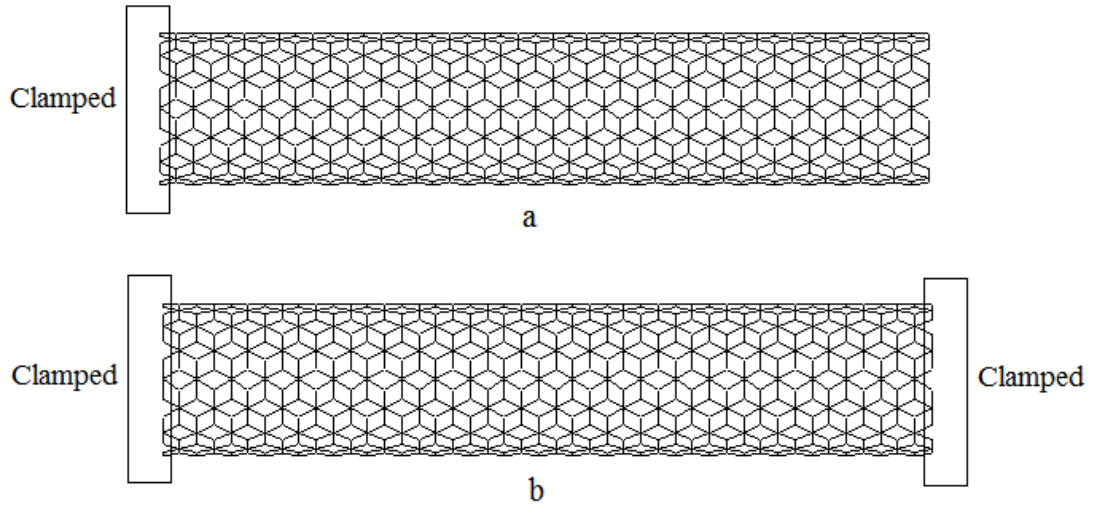


Figure 7.6: Boundary conditions in vibrational analysis of SWCNTs a) Free-clamped and b) clamped-clamped.

After assembling the element stiffness and consistent mass matrices, the natural frequencies and corresponding mode-shapes are obtained by solving the following eigenproblem

$$(K - \omega_i^2 M)d = 0 \quad (7.4)$$

The results are compared with analytical solutions based on the assumption that the SWCNTs are equivalent to cylindrical shells. According to theory of vibration, natural frequencies of the beam model can be calculated as follows

$$f_t = \frac{\beta_n^2}{8\pi L^2} \sqrt{\frac{E(d_o^2 - d_i^2)}{\rho}} \quad (7.5)$$

where E is the Young's modulus of nanotube, L is the length of the nanotube, d_o and d_i are respectively the outer and inner diameters of nanotube, ρ is the density of nanotube and β_n is the specific constant of the n th mode. For free-free vibration of SWCNTs, $\beta_1=4.73$ and for free-clamped vibration of SWCNTs $\beta_1=1.87$ [42].

The natural frequencies of SWCNTs depend on the nanotube diameter and height as well as boundary conditions on the nanotube ends. Tables 7.1- 7.3 show the first six free-free, free-clamped and clamped-clamped natural frequency values of the SWCNTs (8, 8) with different heights. The first six free-free modes of the SWCNTs are the rigid body modes and equal to zero.

Table 7.1: The first six free-free natural frequency values of SWCNTs (8, 8) with different heights (in GHz).

<i>Mode</i>	L=29.53 Å° (400 atoms)	L= 60.3 Å° (800 atoms)	L=79.9 Å° (1056 atoms)	L=159.98 Å° (2096 atoms)	L=199.36 Å° (2608 atoms)
1	995	683	414	112	72
2	995	683	414	112	72
3	1027	1000	907	293	194
4	1027	1000	980	293	194
5	1550	1005	980	455	363
6	1550	1005	1001	538	363

Table 7.2: The first six free-clamped natural frequency values of the SWCNTs (8, 8) with different heights (in GHz)

<i>Mode</i>	L=29.53 Å° (400 atoms)	L= 60.3 Å° (800 atoms)	L=79.9 Å° (1056 atoms)	L=159.98 Å° (2096 atoms)	L=199.36 Å° (2608 atoms)
1	446	121	70	18	11
2	446	121	70	18	11
3	1020	606	385	108	71
4	1020	616	385	108	71
5	1240	895	456	228	183
6	1456	1002	675	287	191

Table 7.3: The first six clamped-clamped natural frequency values of the SWCNTs (8, 8) with different heights (in GHz)

<i>Mode</i>	L=29.53 Å° (400 atoms)	L= 60.3 Å° (800 atoms)	L=79.9 Å° (1056 atoms)	L=159.98 Å° (2096 atoms)	L=199.36 Å° (2608 atoms)
1	1396	595	377	109	71
2	1396	595	377	109	71
3	1589	1062	874	281	188
4	1589	1062	874	281	188
5	2338	1223	919	458	350
6	2338	1262	1033	511	350

In the works [35, 36, 39-43, 55, 57] studying the vibrations of GSs and CNTs, the global mass matrix is derived based on the assumption that the carbon nuclei masses (e.g., 1.9926×10^{-26} kg) are concentrated at the joints of the frame structure. Due to the negligible radius of carbon atomic nucleus (e.g., $r_c = 2.75 \times 10^{-5}$ Å), torsional and flexural rotation coefficients of mass matrices are assumed to be zero and a lumped mass matrix for the beam elements is used. Figure 7.7 shows the equivalent lumped mass MM model of the SWCNT. Tables 7.4- 7.6 show the first six free-free, free-

clamped and clamped-clamped natural frequency values of the lumped mass MM models with different heights.

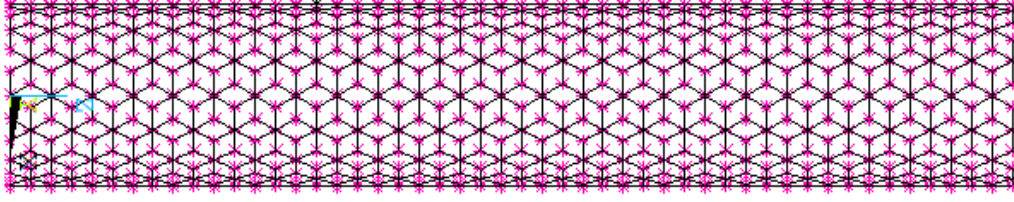


Figure 7.7. Lumped mass MM model of SWCNT.

Table 7.4: The first six free-free natural frequency values of the lumped mass MM models with different heights (in GHz).

<i>Mode</i>	L=29.53 Å° (400 atoms)	L= 60.3 Å° (800 atoms)	L=79.9 Å° (1056 atoms)	L=159.98 Å° (2096 atoms)	L=199.36 Å° (2608 atoms)
1	1124	668	407	111	72
2	1124	668	407	111	72
3	1170	1130	907	291	193
4	1170	1130	964	291	193
5	1665	1138	964	457	361
6	1665	1138	1132	534	361

Table 7.5: The first six free-clamped natural frequency values of the lumped mass MM models with different heights (in GHz).

<i>Mode</i>	L=29.53 Å° (400 atoms)	L= 60.3 Å° (800 atoms)	L=79.9 Å° (1056 atoms)	L=159.98 Å° (2096 atoms)	L=199.36 Å° (2608 atoms)
1	436	120	70	18	12
2	436	120	70	18	12
3	1153	608	382	108	71
4	1153	608	382	108	71
5	1235	610	459	230	184
6	1575	888	671	286	191

Table 7.6: The first six clamped-clamped natural frequency values of the lumped mass MM models with different heights (in GHz).

<i>Mode</i>	L=29.53 Å° (400 atoms)	L= 60.3 Å° (800 atoms)	L=79.9 Å° (1056 atoms)	L=159.98 Å° (2096 atoms)	L=199.36 Å° (2608 atoms)
1	1511	595	378	109	72
2	1511	595	378	109	72
3	1592	1192	875	281	189
4	1592	1192	875	281	189
5	2458	1235	928	462	350
6	2458	1305	1164	511	350

As can be seen in Tables 7.1 – 7.6, the consistent mass and lumped mass MM models have very close natural frequencies. It is noteworthy that transient dynamics analyses can be performed by using Newmark method due to advantages of the consistent mass matrix which does not yield singularity in numerical integrations. Lee and Lee [43] use Timoshenko beam element formulations which include shear deformation effects but they employed Euler-Bernoulli beam element constants (i.e., see Table 7.1) [37]; this assumption affects the natural frequencies of SWCNT that are found to be lower than those of Euler-Bernoulli beam elements. As can be seen in Tables 7.1-7.6, SWCNTs have very high natural frequencies. As a result, ultrahigh frequency nanomechanical resonators can be achieved by using SWCNTs.

Figures 7.8- 7.10 show the first six free-free, free-clamped and clamped-clamped mode shapes of consistent MM model of SWCNTs (8, 8) with height of 60.3 Å°. In addition, lumped mass MM model of the SWCNTs have similar mode shapes.

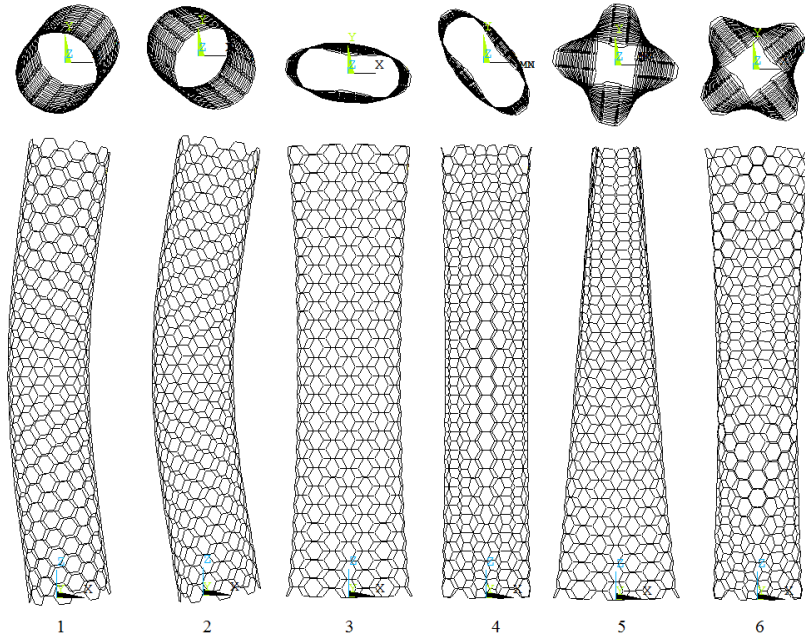


Figure 7.8: The first six free-free mode shapes of consistent MM model of SWCNTs (8, 8) with height of 60.3 Å.

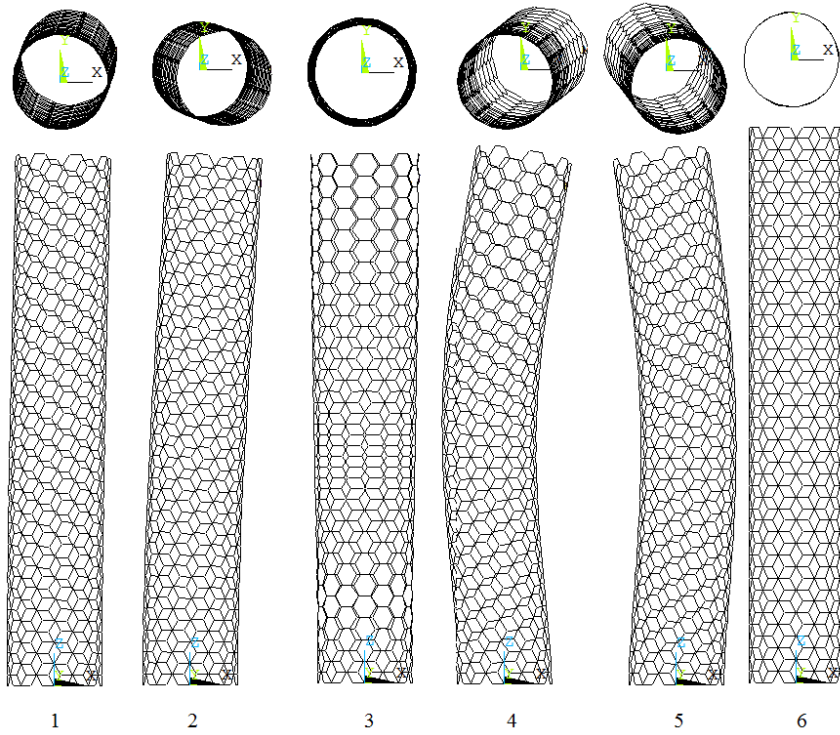


Figure 7.9: The first six free-clamped mode shapes of consistent MM model of SWCNTs (8, 8) with height of 60.3 Å.

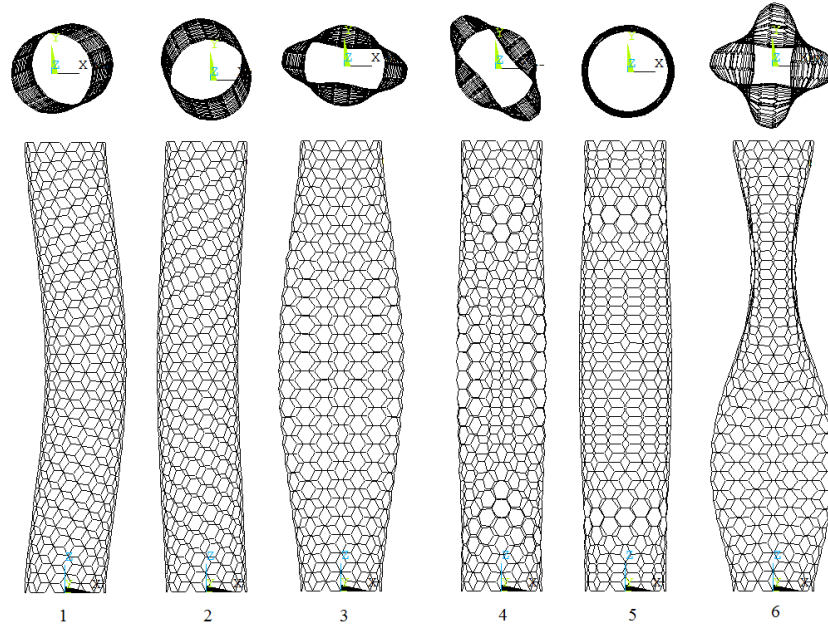


Figure 7.10: The first six clamped-clamped mode shapes of consistent MM model of SWCNTs (8, 8) with height of 60.3 Å.

The numerical solutions of the fundamental mode frequencies of free-free, free-clamped and clamped-clamped SWCNTs (8,8) as well as the analytical solutions of free-free, free-clamped equivalent cylindrical shells models versus aspect ratio L/D is plotted in Figure 7.11. There is a large gap between the present results and those obtained from the equivalent cylindrical shells models, where all the present results are larger than the theoretical values. This is originating from the fact that out-of-plane bending rigidity of the 3-D CM shell model is in error that is already reported by other researchers [33, 40]; hence, corrections for the thickness value of the 3-D CM shell model are suggested in literature. Studies on this issue have been continuing. It is concluded that the proposed approach can compute the natural frequencies of SLGSs in high accuracy and employment of consistent mass matrix in FE model improves accuracy.

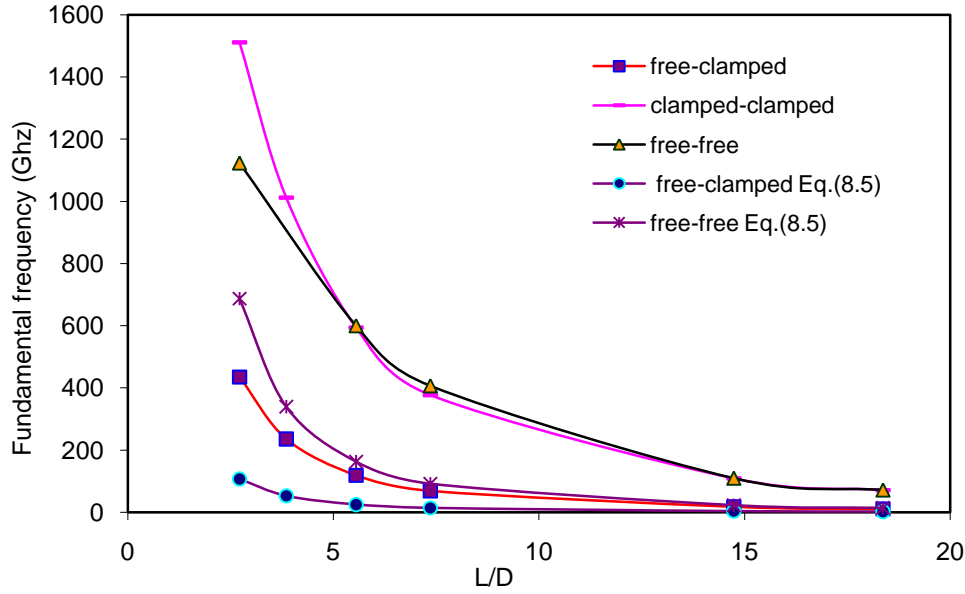


Figure 7.11: The numerical and analytical solutions of the fundamental mode frequencies of free-free, free-clamped and clamped- clamped SWCNTs (8,8) versus aspect ratio L/D .

7.4. Elastic Buckling Analysis of SWCNTs

Similar to vibration analysis, we investigate the critical buckling load and associated buckling modes of SWCNTs are studied by completing elastic buckling analysis. Figure 7.12 shows the boundary and loading conditions for elastic buckling analysis of the SWCNTs.

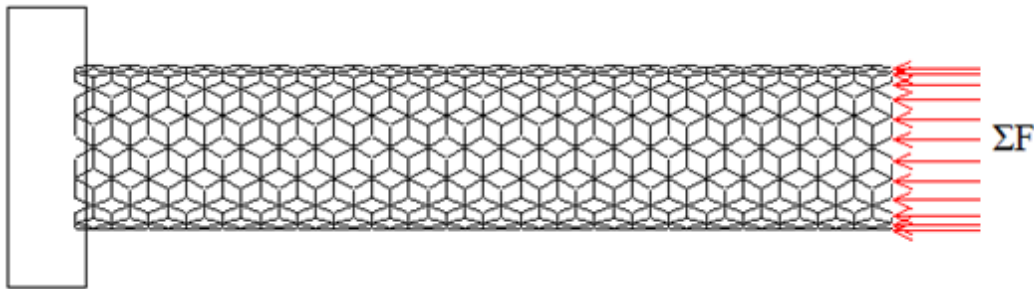


Figure 7.12: SWCNTs (8,8) along with the applied boundary conditions.

The results are compared with analytical solutions based on the assumption that the SWCNTs are equivalent to cylindrical shells. According to theory of structural stability, the critical elastic buckling load P_{cr} for a general cantilevered column can be calculated as an Euler equation as follows

$$P_{cr} = \frac{\pi^2 EI}{4L^2} \quad (7.6)$$

where E is the Young's modulus of nanotube, L is the length of the nanotube and I is the moment of inertia.

Numerical solutions of the critical buckling load of SWCNTs (8,8) as well as analytical solutions of equivalent cylindrical shells models versus aspect ratio L/D are plotted in Figure 7.13. As can be seen in Figure 7.13, the critical axial buckling load for both armchair and zigzag types decreases as the tube height increases. The trend is comparable with that of the analytical results based on Euler formulation with thickness of 3.4 Å.

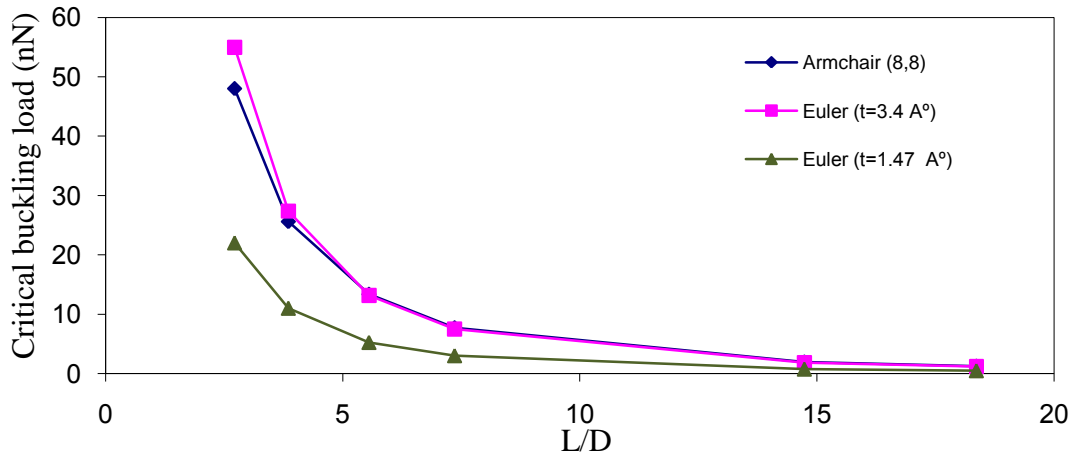


Figure 7.13: The numerical and analytical solutions of the critical buckling loads of SWCNTs (8,8) versus aspect ratio L/D .

The critical buckling loads of both armchair and zigzag types of the SWCNTs with the height of 41.8 Å as a function of nanotubes diameter are shown in Figure 4.14. As can be seen in Figure 7.14 the critical axial buckling load for both the armchair and zigzag types increases as the tube diameter increases. The trend is comparable with that of analytical results based on Euler formulation with thickness of 3.4 Å.

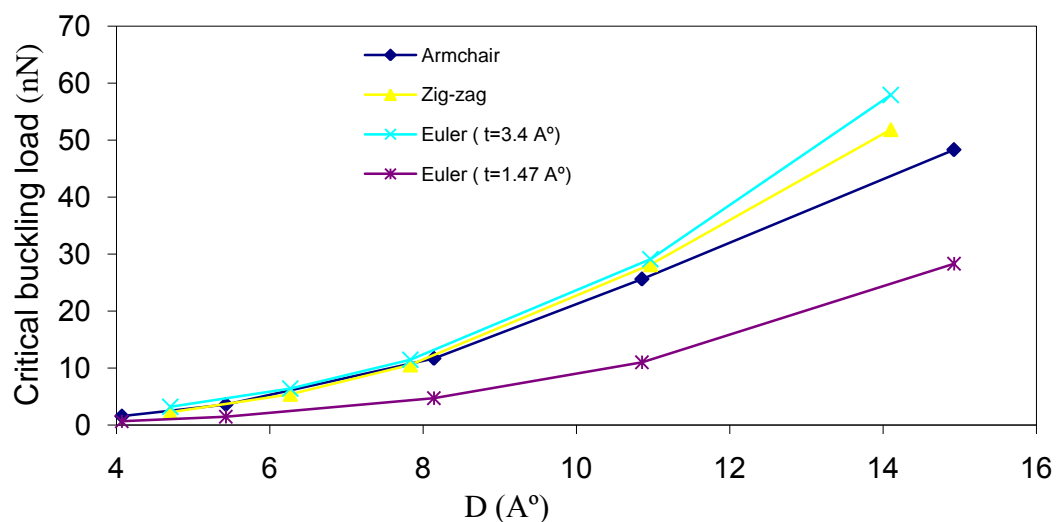


Figure 7.14: Critical buckling loads of SWCNTs as a function of nanotube diameter.

Figure 7.15 shows the first six buckling mode shapes of SWCNTs (8,8) with the height of 60.3 Å. In addition, several local buckling mode occurs at higher frequencies.

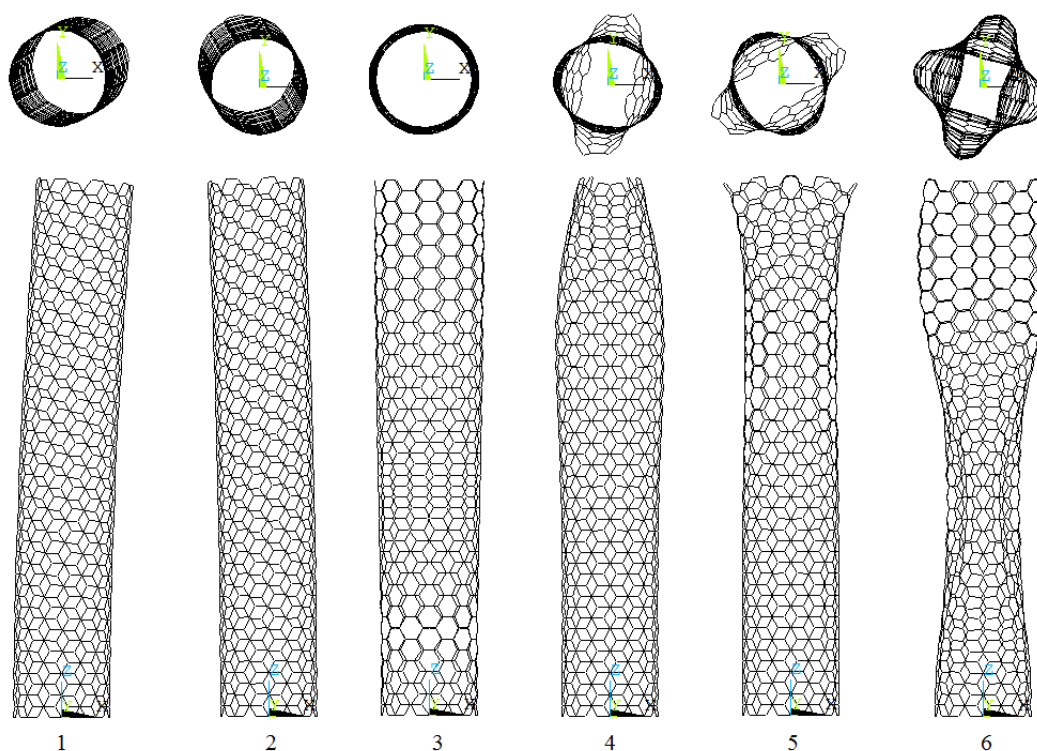


Figure 7.15: The first six buckling mode shapes of SWCNTs (8,8) with the height of 60.3 Å

7.5. Prediction of Failure Behavior of CNTs

In this thesis, an equivalent nonlinear fracture model for SWCNTs is developed by using an MM based FE approach where the C-C bonds between carbon atoms are represented by Euler-Bernoulli beam elements. In the analyses, the modified Morse potential along with an iterative solution procedure is utilized to update the stiffness of elements. Although progressive fracture of SLGSs and SWCNTs are studied earlier, they are obtained without consideration of geometric nonlinear effects and used non-reconstructed defected zigzag and armchair SWCNTs. In this paper, the proposed approach is applied to pristine and reconstructed one- and two-atom vacancy defected zigzag and armchair SWCNTs. The initial reconstructed nanotube models are obtained by using MD simulations whose results are compared with the results of non-reconstructed ones. Effects of large deformation and geometric nonlinearities on fracture behavior of defected nanotubes are also studied by updating the nodal coordinates of each element of the original nanotube structure at each load step.

7.5.1 Fracture model of SWCNTs

Four different types of SWCNTs are considered in the simulations, and the geometric properties and total number of atoms of pristine SWCNTs are listed in Table 7.7.

Table 7.7: The geometric properties and total number of atoms SWCNTs.

SWCNT	Diameter, d (Å)	Total number of atoms
(5,5)	6.785	350
(12,12)	16.283	840
(10,0)	7.834	400
(20,0)	15.669	800

As already mentioned, production of mass-quantities of defect-free GSs or CNTs may prove challenging and different types of defects may emerge in practice. The possible and mostly studied CNT defects are incomplete bonding defects such as vacancies [66, 145-147]. Vacancy defects originate from missing atoms in the CNTs and may occur due to an electron irradiation or oxidative purification. These defects cause a reduction in the strength of SWCNTs and significantly affect the mechanical performance of nanocomposite materials.

Sammalkorpi et al. [71] investigated the effect of reconstructed and non-reconstructed vacancy defects on the tensile behavior of CNTs and found that the reduction in the strength of CNTs caused by reconstructed case is smaller than that caused by the non-reconstructed case. Note that Sammalkorpi et al. [71] used an annealing step beginning the MD simulations at a high temperature for reconstruction. However, reconstruction does not occur in our simulations since the distance between the potential reaction atoms exceeds the interaction cut-off distance. To this end, we used an extra annealing step at a high temperature (i.e.,

K) by using MD simulations to obtain reconstructed geometry of the defected SWCNTs. On the other hand, although metastable, the non-reconstructed SWCNT configurations can be present at low temperatures and low dose irradiation [132, 133], non-reconstructed defected SWCNTs are used in several works in literature [85, 132, 134]. In brief, one carbon atom and corresponding three C-C bonds are removed in the defect-free non-reconstructed SWCNT models and reconstructed models are obtained by using MD simulations with annealing at a high temperature (i.e., see Figure 7.16 for the pristine, reconstructed one- and two-atom vacancy defected SWCNT models).

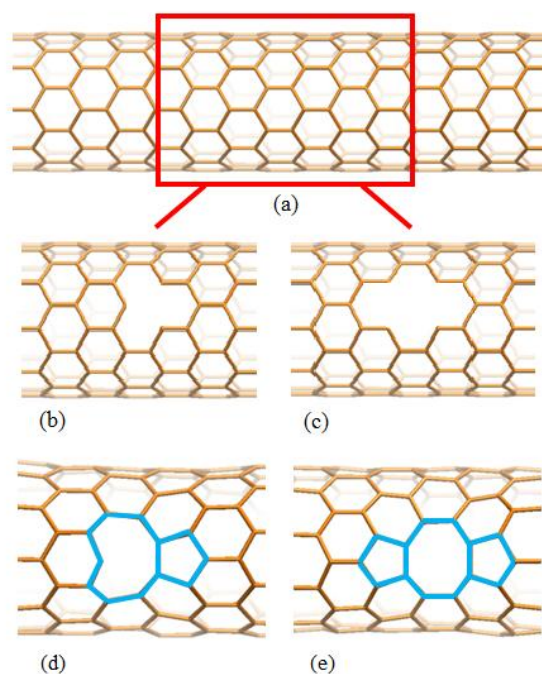


Figure 7.16: Zigzag (10,0) nanotube models; (a) pristine, (b) non-reconstructed one-atom vacancy defect (c) non-reconstructed two-atom vacancy defect, (d) reconstructed one-atom vacancy defect (e) reconstructed two-atom vacancy defect.

The MD simulations utilized to find the global minimum configurations of non-reconstructed vacancies are performed using the widely-used LAMMPS (Large-scale Atomistic/Molecular Massively Parallel Simulator) code [148]. As the inter-atomic potential, adaptive intermolecular reactive empirical bond order (AI-REBO) potential [149] is employed to model interactions between carbon atoms. Using Nosé-Hoover thermostat, CNT models with one/two vacancies are thermally equilibrated at a high temperature (i.e., 3000 K) in the canonical ensemble (NVT) and kept at the same temperature for 40 picoseconds (ps). Then, the temperature of the system is gradually decreased with the rate of 10 K/ps under the same thermostat.

7.5.2. Computational results

The strain in SWCNTs is calculated by $\varepsilon_L = (L_s - L_{s0}) / L_{s0}$ where L_{s0} is the initial (equilibrium) length and L_s is the current length of the tube. The stress is calculated by $\sigma = F_g / (\pi d t)$ where F_g is the corresponding applied tensile force computed by summation of the longitudinal reaction forces of the constrained nodes, d is the diameter of tube and t is the thickness of tube. In all calculations, the thickness of 0.34 nm is used for the SWCNTs. Since the accuracy of the results depends on the number of load steps, an acceptable strain increment is determined on a trial and error base to guarantee the convergence of numerical results. All fracture computations of the MM model are completed by using a computer code developed in Matlab environment. Table 7.8 shows the calculated tensile strength and fracture strain values of the pristine SWCNTs along with the results reported in literature.

Table 7.8: Predicted values of critical strain (ϵ_{cr}) and stress (σ_{cr}) for pristine SWCNTs. (M)TB, PM3 and DFT represent the (Modified) Tersoff-Brenner potential, semi-empirical quantum and density functional theory calculation, respectively.

Study	Method	Chirality	ϵ_{cr} (%)	σ_{cr} (GPa)
Present work	Modified Morse	5,5	21.1	122.8
Present work	Modified Morse	12,12	20.7	122.5
Present work	Modified Morse	10,0	16.0	94.8
Present work	Modified Morse	20,0	15.9	94.7
Mielke et al. [78]	MTB, PM3, DFT	5,5	30,30,30	105,135, 110
Mielke et al. [78]	MTB, PM3, DFT	10,0	18, 20, 20	88, 124, 105
Sammalkorpi et al. [71]	TB	5,5	26	240
Jeng et al. [150]	TB	10,0	19	92.5
Belytschko et al. [72]	Modified Morse	12,12	18.7	112
Belytschko et al. [72]	Modified Morse	20,0	16.0	93.5
Tserpes and Papanikos [86]	Modified Morse	5,5	19.6	122.5
Tserpes and Papanikos [86]	Modified Morse	12,12	19.6	121.9
Tserpes and Papanikos [86]	Modified Morse	20,0	15.8	97.7
Meo and Rossi [92, 94]	Modified Morse	5,5	19.9	117.3
Meo and Rossi [92, 94]	Modified Morse	12,12	20.0	117.9
Meo and Rossi [92, 94]	Modified Morse	10,0	18.4	94.7
Meo and Rossi [92, 94]	Modified Morse	20,0	18.0	94.5
Xiao et al. [90]	Modified Morse	12,12	23.1	126.2
Xiao et al. [90]	Modified Morse	20,0	15.6	94.5
Duan et al. [151]	Modified Morse	10,0	33.3	105.4
Duan et al. [151]	REBO	10,0	27.3	99.9

It is observed in Table 7.8 that calculated critical strain and stress values lie in the same range with the results reported in literature. By making comparisons among our results and those of [72, 78, 86, 90, 92, 94] employing the modified Morse potential function in Table 7.8, it is concluded that they are in good agreement although underlying formulations are different. In addition, the tensile strength and failure strain values in armchair tubes are higher than those in zigzag tubes, which also agrees with the studies in literature. Moreover, the results indicate that the diameters of nanotubes have a little effect on the critical stress and strain values. In the meantime, it should be noted that Yu et al. [29] experimentally measured the tensile strength and failure strain of MLCNTs and found 11–63 GPa for the strengths and 10–13% for the failure strains. These strain and stress values are significantly smaller

than the results in Table 3; these differences can be explained by the presence of defects and some slippage at the attachments which may occur at high-strain cases [76]. Figures. 17 and 18 respectively show the comparison of the stress-strain curves for pristine armchair (12,12) and zigzag (20,0) SWCNTs. It is clear in fracture stress-strain curves that our computational results are in good agreement with the results reported in literature as well. As can be seen in Figures. 17 and 18, the resulting stress exhibits a sudden drop to zero when the stress reaches to the fracture stress. Therefore, it is concluded that the fracture of all types of SWCNTs are brittle which are also reported in several other studies in literature [72, 86, 90].

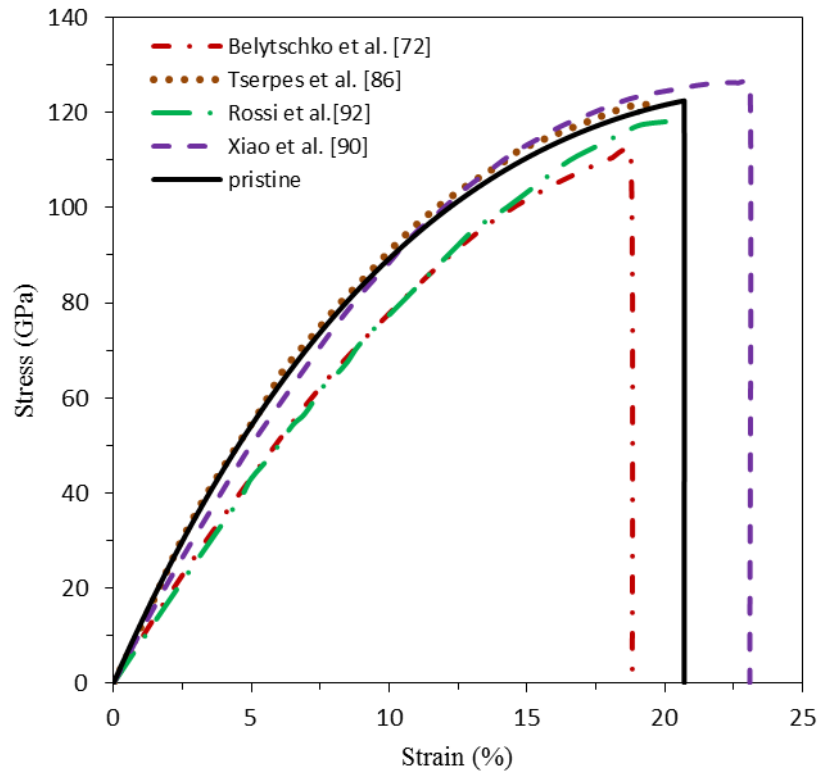


Figure 7.17: Stress-strain curves for pristine nanotube armchair (12,12) under uniaxial load.

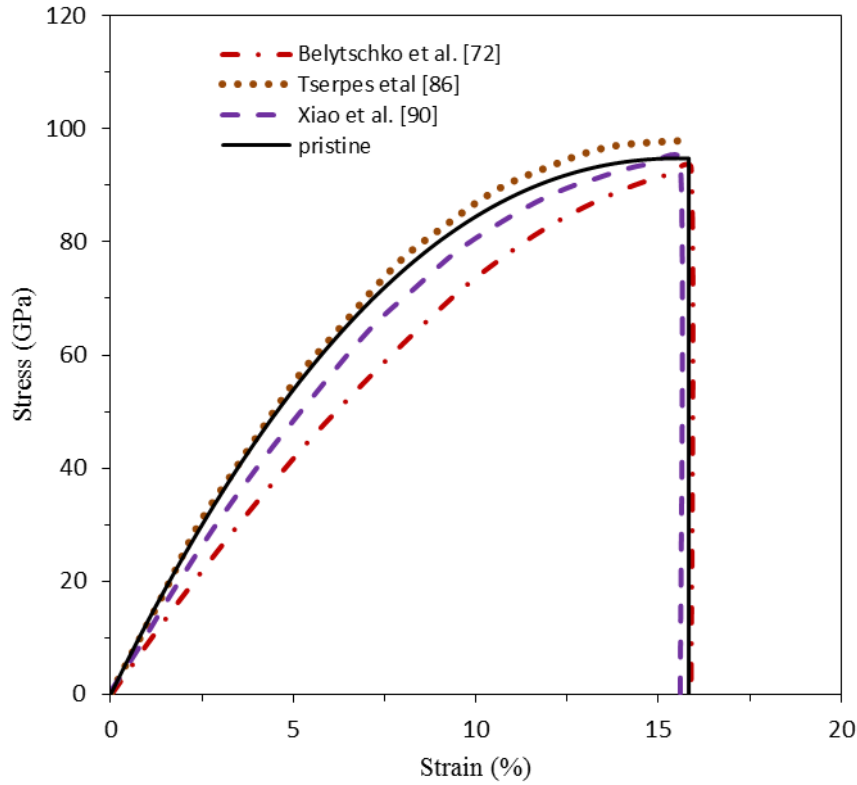


Figure 7.18: Stress-strain curves for pristine nanotube zigzag (20,0) under uniaxial load.

Table 7.9 compiles strain and stress ratios for reconstructed vacancy defected nanotubes versus pristine nanotubes. It can be seen that one- and two-atom vacancy defected nanotubes have similar fracture stress and strain values. In addition, it is observed in Table 7.9 that calculated relative critical strain and stress values lie in the same range with the results in literature.

Figure 7.19 shows the stress-strain curves for one-atom vacancy defected armchair (5,5) and zigzag (10,0) nanotubes versus pristine nanotubes. Meanwhile, we also examined a one-atom non-reconstructed vacancy defected (5,5) nanotube. In sum, the one-atom non-reconstructed vacancy defected nanotube (5,5) has similar fracture stress and strain values (i.e., $\epsilon=10.2\%$ and $\sigma=89.0$ GPa) with the reconstructed one (i.e., $\epsilon=10.3\%$ and $\sigma=89.1$ GPa). In parallel, Sammalkorpi et al. [71] and Meo and Rossi [94] also observed that reconstructed and non-reconstructed one-atom vacancy defected nanotubes (5,5) have similar mechanical properties as well. Meo and Rossi [94] also reported fracture stress and strain of one-atom vacancy defected nanotubes as $\epsilon=12.3\%$ and $\sigma=89.8$ GPa, respectively. In brief, it is observed that fracture stress

and strain values of pristine armchair CNTs are respectively 30% and 32% larger than those of pristine zigzag CNTs, and predicted failure stress and strain values of vacancy defected SWCNTs are respectively 27% and 52 % smaller than those of pristine ones.

Table 7.9: Relative critical strain ($\varepsilon/\varepsilon_{cr}$) and stress (σ/σ_{cr}) ratios for defected SWCNTs where the defects are reconstructed (R) and symmetrically (sym) oriented. MTB stands for the modified Tersoff-Brenner potential and PM3 stands for semi-empirical quantum calculations. The defect key indicates the number of vacant atoms.

Study	Method	Chirality	Defect	ε (%)	σ (GPa)	$\varepsilon / \varepsilon_{cr}$	σ / σ_{cr}
Present work	Modified Morse	5,5	1R sym	10.3	89.1	0.49	0.73
Present work	Modified Morse	10,0	1R sym	7.74	69.6	0.48	0.74
Present work	Modified Morse	5,5	2R sym	10.4	90.2	0.49	0.73
Present work	Modified Morse	10,0	2R sym	7.68	69.1	0.48	0.73
Zhang et al. [76]	MTB	10,0	1R sym	8.7	65	0.48	0.74
Zhang et al. [76]	MTB	5,5	2R sym	11.7	71.3	0.39	0.68
Zhang et al. [76]	MTB	10,0	2R sym	9.6	64.4	0.53	0.73
Mielke et al. [78]	PM3	5,5	1R	15.3	100	0.51	0.74
Mielke et al. [78]	PM3	5,5	2R sym	17.2	105	0.57	0.78
Mielke et al. [78]	PM3	10,0	2R sym	14.2	107	0.71	0.86
Meo and Rossi [94]	Modified Morse	5,5	1R	12.3	89.8	0.62	0.77

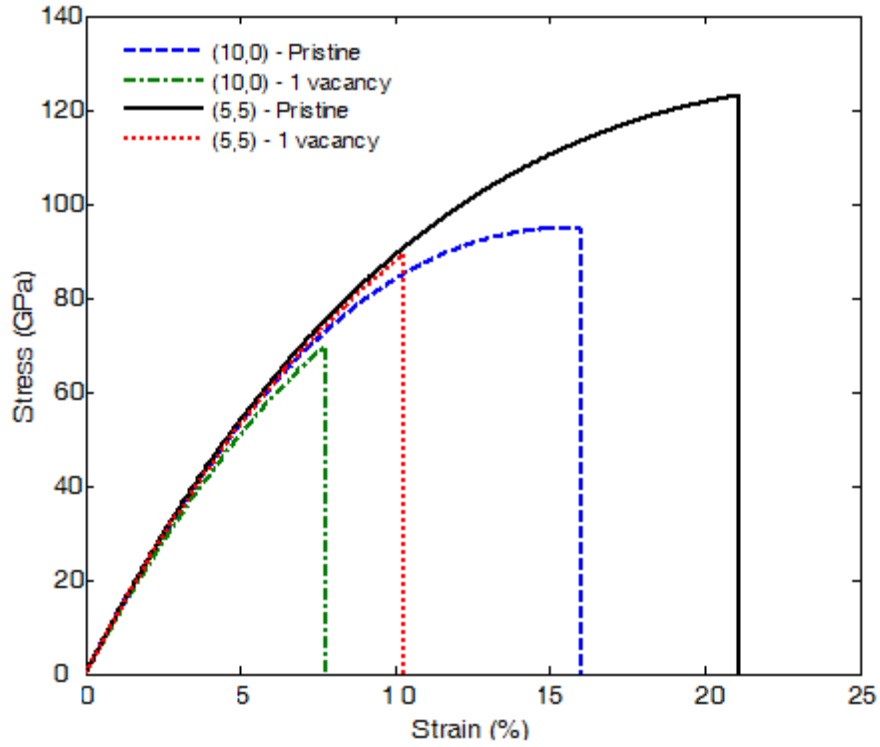


Figure 7.19: Stress-strain curves of pristine nanotubes (10,0) and (5,5) and one-atom vacancy defected nanotubes (10,0) and (5,5) under uniaxial load.

Another issue is that the fracture in nanotubes occurs at relatively large strain values; therefore, we also investigated the effects of large deformation and geometric nonlinearities on fracture behavior of defected nanotubes. In the analyses of defected SWCNTs, nodal coordinates of each element in the original SWCNT structure is updated at each load step and deformation of the original nanotube structure around the nucleation site is taken into account. Table 7.10 shows the effect of geometric nonlinearity on fracture behavior of reconstructed one-atom vacancy defected (5,5) and (10,0) nanotubes. It can be seen in Table 7.10 that by including large deformation and geometric nonlinearity effects, failure stress and strain values of zigzag nanotubes are reduced more than those of armchair ones. In this regard, Figure 7.20 shows the failure stress-strain curves of one-atom vacancy defected nanotubes with non-linear geometric effect. It is concluded that large deformation and nonlinear geometric effects are important on fracture behavior of nanotubes and cause a reduction in calculated fracture strain values of vacancy defected SWCNTs by approximately 10% and 7%, respectively.

Table 7.10: Effect of geometric nonlinearity on fracture behavior of reconstructed one-atom vacancy defected SWCNTs.

Chiralit y	Defect	ϵ_{nlgeom} (%)	σ_{nlgeom} (GPa)	$\epsilon_{nlgeom}/\epsilon$	σ_{nlgeom}/σ
5,5	1R sym	10.2	82.3	0.99	0.92
10,0	1R sym	7.17	62.9	0.93	0.90
5,5	2R sym	10.3	82.5	0.99	0.92
10,0	2R sym	7.11	62.0	0.93	0.90

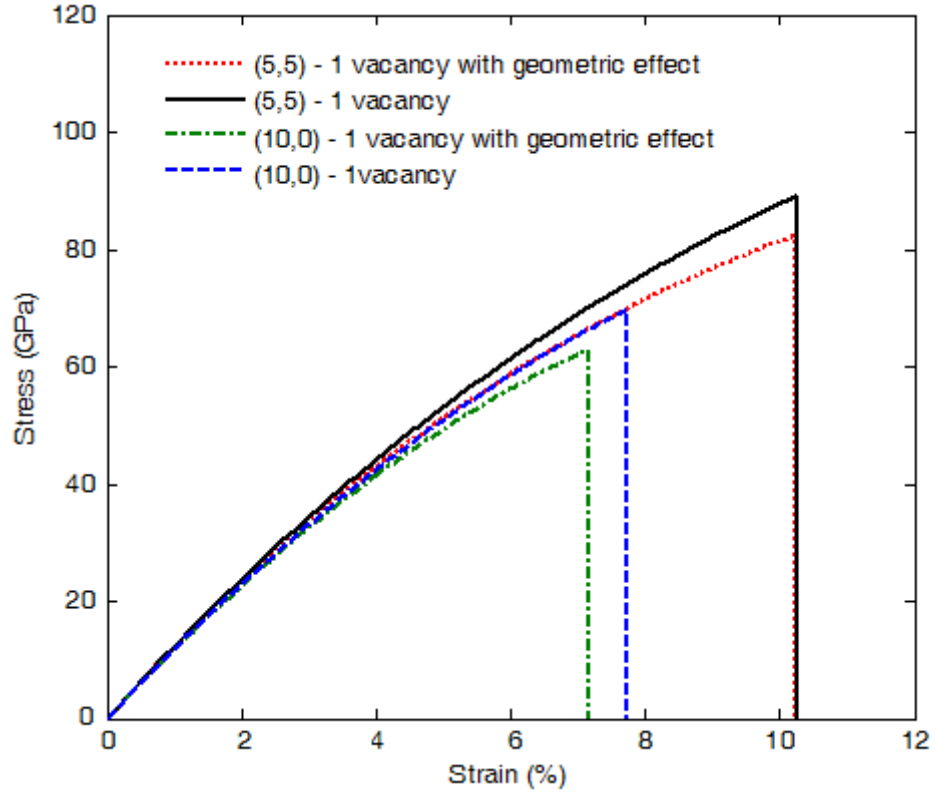


Figure 7.20: Stress-strain curves of one-atom vacancy defected nanotubes with non-linear geometric effect.

8. CONCLUSION

In this thesis, equivalent models of single-layer graphene sheets (SLGSs), single layer carbon nanotubes (SWCNTs) and single layer carbon nanocones (SWCNCs) are developed by using molecular mechanics (MM) based FE approach. Then, elastic, vibrational and buckling characteristics of SWCNTs; vibrational and elastic buckling characteristics of SWCNCs, and elastic and vibrational characteristics of SLGSs are investigated. In addition, an equivalent dynamic model is developed for SLGSs and 2-D and 3-D transient behavior of SLGSs are investigated; a nonlinear fracture model of SLGSs are developed and fracture behavior of defected and non-defected SLGSs are studied, and multiscale models of SLGSs are developed for coupling of atomistic and continuum domains.

Equivalent dynamic models for the SLGSs are developed by using atomistic FE approach. 2-D and 3-D transient and modal characteristics of the SLGSs are examined. Comparisons are made among the results of the MM based model, CM based model and relevant works in literature. An equivalent density parameter is derived which is obtained by the equivalency of natural frequencies of the MM and CM models. The response to initial displacements are computed for the 2-D and 3-D FE models where initial displacements are applied incrementally on SLGSs and nodal coordinates of the original SLGS structure are updated at each displacement increment; hence, large deformation effects and uniform initial displacement conditions are considered in analyses. It is shown that the proposed MM model can compute 2-D and 3-D dynamic characteristics of the SLGS structures in high accuracy. It is observed that power spectral density properties of transient analyses are in good agreement with modal features of the SLGSs.

The MM and plane-stress CM models have very close natural frequencies and static transient in-plane displacement in numerical experiments. Whereas, it is noteworthy that bending rigidity of the 3-D CM shell models is in error with that of the

corresponding MM model and associated transient out-of-plane displacement solutions and natural frequencies do not agree with those of the MM models, that is also reported by some researchers in literature. In the future, this discrepancy will be investigated to improve accuracy of shell models. In addition, the Morse potential can easily be adapted to include nonlinear effects in future studies. Moreover, multiscale formulations for wave propagation problems can be adapted to dynamic models along with model order reduction algorithms.

In this thesis, an atomistic based FE model for the prediction of nonlinear fracture behavior of SLGSs is also developed. Euler-Bernoulli beam elements are used to represent covalent bonds and non-linear characteristic of the beam elements are obtained by using the modified Morse potential. The proposed approach includes large deformation and nonlinear geometric effects. Namely, elasticity modulus of each EB beam element and nodal coordinates of the original SLGS structures are updated at each load step. Formulation underlying the proposed approach is applied to zigzag and armchair SLGSs. It is shown that large deformation and nonlinear geometric effects are important in fracture behavior of SLGSs. It is observed that SLGS exhibits an orthotropic fracture behavior. Namely, it is stiffer in the armchair direction than in the zigzag direction. Effects of various defects on fracture behavior of SLGSs are also examined. The results show that these defects significantly affect the mechanical performance of the SLGSs. In addition, fracture initiation and crack propagation direction are studied. It is observed that the fractures of all types of SLGSs are brittle. The numerical results are compared with the results in literature and our results show good agreement with the results reported in literature.

A coupling method for the MM and CM models is also derived based on an augmented formulation of atomistic and continuum displacement fields in a moving least square sense, which originates from an unconstrained optimization problem to be solved. In order to solve the augmented problem, the Lagrange multiplier method is used which allows multiscale analyses of multiple numbers of MM domains in a single CM domain. The CM domain covers the entire domain and the MM domain is patched on the element(s) of the CM domain. In contrast to alternative approaches existing in literature, there is no need for an overlapping domain in the proposed approach and the MM domain(s) can be placed arbitrarily in the CM domain; hence,

one can focus on any desired subdomain where we need to obtain atomistic solution. In addition, there is no need for a constraint on the meshes of the MM and CM domains. Efficiency of the proposed approach is illustrated by using defect-free and defected monolayer graphene layers. In the atomistic models, harmonic potentials and modified Morse potentials are employed. In the CM domain, it is assumed that deformations are elastic and plane stress conditions exist, for which elasticity modulus and Poisson's ratio values of the CM domain are obtained by the use of full MM models, and compared with the results presented in literature. Equivalent continuum elasticity modulus, Poisson's ratio and shear modulus of monolayer graphene are obtained in the range of 1.032-1.047 TPa, 0.061-0.069 and 0.482-0.493 TPa, respectively.

It is shown that proposed formulation can compute the deformations of monolayer graphenes in high accuracy, enables to obtain the MM solution(s) in any part of the CM domain and can be applied to other nano structured materials. Main advantage of the proposed formulation is that it can be used to connect the MM domain(s) to any subdomain of the CM domain by proper choice of projection matrices without changing the mesh. Therefore, it enables fast reanalysis of any subdomain of the CM domain at fine scales. In addition, appropriate stiffness matrices of the MM and CM domains which are exported as superelements can be embedded into the formulations that enables linking by commercial softwares. By updating the elasticity parameters of the CM domain based on the MM solutions, nonlinear effects are easily considered in iterative solutions of large deformation problems that provide more accurate nonlinear solutions.

The elastic buckling and vibration behaviors of SWCNCs are investigated. The MM based FE approach is used to achieve this goal. The axial compression and bending loading conditions are considered in elastic buckling behavior of SWCNCs while free-free, free-clamped and clamped-clamped boundary conditions are considered in vibration analysis of SWCNCs. The effects of cone height and apex angles on the buckling force and natural frequencies of SWCNCs are also studied. Vibration analysis results indicate that the natural frequency decreases with increasing cone height in all types of SWCNCs, whereas it increases as the disclination angle increases. Buckling analysis results indicate that as the disclination angle increases,

the critical buckling load increases in axial compression loading and decreases in bending loading. In addition, it is observed that bending loading is more critical than axial compression loading for buckling behavior of SWCNCs if the disclination angle increases. When free-clamped and clamped-clamped boundary conditions are considered, fundamental frequencies of the SWCNCs are found to be in the range of 0.36 – 2.52 THz. The axial and bending buckling forces are found to be in the range of 42 – 79 nN and 27 – 64 nN, respectively. These results are comparable with the results for CNTs and SLGSs in literature in most cases and it can be used in designing atomic force microscope (AFM) and scanning tunneling microscope (STM) tips. In the future, fracture and transient dynamics analyses can be performed in order to evaluate the damage and dynamic behavior of SWCNCs. Moreover, Morse potential can be employed in the MM model for large deformation problems.

An MM based FE model of SWCNTs is developed for fracture analysis as well. In this regard, Euler-Bernoulli beam elements are used to represent the covalent bonds and non-linear characteristics of the beam elements are obtained by using the modified Morse potential. The proposed approach is applied to pristine and reconstructed one- and two-atom vacancy defected zigzag and armchair SWCNTs. The initial reconstructed nanotube models are obtained by using MD simulations whose results are compared with the results of non-reconstructed ones. As a result of analyses, it is concluded that fractures of all types of SWCNTs are brittle, armchair SWCNTs are stiffer than zigzag SWCNTs, there is no significant difference between fracture strengths of reconstructed and non-reconstructed SWCNTs and vacancy defects significantly affect the mechanical behavior of SWCNTs. In brief, fracture stress and strain values of pristine armchair CNTs are respectively 30% and 32% larger than those of pristine zigzag CNTs, and predicted failure stress and strain values of vacancy defected SWCNTs are respectively 27% and 51 % smaller than those of pristine ones. It is shown that large deformation and nonlinear geometric effects are important on fracture behavior of nanotubes and cause a reduction in calculated fracture strain values of vacancy defected SWCNTs by approximately 10% and 7%, respectively. Comparisons are made with the failure stress and strain results reported in literature that show good agreement with our results.

REFERENCES

- [1] **Iijima, S.**,1991. Helical microtubules of graphitic carbon, *Nature*, **354**, 56-58.
- [2] **Popov, V.N.**, 2004. Carbon nanotubes: properties and application, *Mater. Sci. Eng.*, **43**, 61–102.
- [3] **Lier, G.V., Alsenoy, C.V., Doren, V.V., Geerlings, P.**, 2000. Ab initio study of the elastic properties of single-walled carbon nanotubes and graphene, *Chemical Physics Letters*, **326**, 181-185.
- [4] **Castro Neto, A.H., Guinea, F., Peres, N.M.R., Novoselov, K.S. and Geim, A.K.**, 2009. The electronic properties of graphene *Reviews of Modern Physics*, **81**, 109-162.
- [5] **Stankovich, S., Dikin, D.A., Dommett, G.H.B., Kohlhaas, K.M., Zimney, E.J., Stach, E.A., Piner, R.D., Nguyen, S.T. and Ruoff, R.S.**, 2006. Graphene-based composite materials, *Nature*, **442**, 282-286.
- [6] **Frank, I.W., Tanenbaum, D.M., van der Zande, A.M. and McEuen, P.L.**, 2007. Mechanical properties of suspended graphene sheets, *Journal of Vacuum Science & Technology B*, **25**, 2558-2561.
- [7] **Geim, A.K.**, 2009. Graphene: Status and Prospects, *Science*, **324**, 1530-1534.
- [8] **Katsnelson, M.I.**, 2007. Graphene: carbon in two dimensions, *Materials Today*, **10**, 20-27.
- [9] **Jordan, S.P. and Crespi, V.H.**, 2004. Theory of carbon nanocones: mechanical chiral inversion of a micron-scale three-dimensional object, *Physical Review Letters*, **93**, 255504.
- [10] **Lammert, P.E. and Crespi, V.H.**, 2004. Graphene cones: Classification by fictitious flux and electronic properties, *Physical Review B*, **69**, 035406.
- [11] **Berber, S., Kwon, Y.K. and Tomanek, D.**, 2000. Electronic and structural properties of carbon nanohorns, *Physical Review B*, **62**, 2291-2294.
- [12] **Yang, N., Zhang, G. and Li, B.**, 2008. Carbon nanocone: A promising thermal rectifier, *Applied Physics Letters*, **93**, 243111.
- [13] **Kumar, D., Verma, V., Bhatti, H.S., Dharamvir, K.**, 2011. Elastic moduli of carbon nanohorns, *Journal of Nanomaterials*, **2011**, 127952.
- [14] **Wei, J.X., Liew, K.M. and He, X.Q.**, 2007. Mechanical properties of carbon nanocones, *Applied Physics Letters*, **91**, 261906.
- [15] **Ge, M. and Sattler, K.**, 1994. Observation of fullerene cones, *Chemical Physics Letters*, **220**, 192-196.

- [16] **Krishnan, A., Dujardin, E., Treacy, M.M.J., Hugdahl, J., Lynum, S. and Ebbesen, T.W.**, 1997. Graphitic cones and the nucleation of curved carbon surface, *Nature*, **388**, 451-454.
- [17] **Sripirom, J., Noor, S., Köhler, U. and Schulte, A.**, 2011. Easy made and handled carbon nanocones for scanning tunneling microscopy and electroanalysis, *Carbon*, **49**, 2402-2412.
- [18] **Chen, C., Chen, L.H., Ye, X.R., Daraio, C., Jin, S., Orme, C.A., Quist, A. and Lal, R.**, 2006. Extreme sharp carbon nanocone probe for atomic force microscopy imaging, *Applied Physics Letters*, **88**, 153102.
- [19] **Hsieh, J.Y., Chen, C., Chen, J.L., Chen, C.I. and Hwang, C.C.**, 2009. The nanoindentation of a copper substrate by single-walled carbon nanocone tips: A molecular dynamics study, *Nanotechnology*, **20**, 095709.
- [20] **Yu, S.S. and Zheng, W.T.**, 2010. Effect of N/B doping on the electronic and field emission properties for carbon nanotubes, carbon nanocones, and graphene nanoribbons, *Nanoscale*, **2**, 1069.
- [21] **Lee, C., Wei, X., Kysar, W., and Hone, J.**, 2008. Measurement of the elastic properties and intrinsic strength of monolayer graphene, *Science*, **321**, 5887, 385-388.
- [22] **Treacy, M.M.J., Ebbesen, T.W., Gibson, J.M.**, 1996. Exceptionally high Young's modulus observed for individual carbon nanotubes, *Nature*, **38**, 678-680.
- [23] **Wong, E.W., Sheehan, P.E., Lieber, C.M.**, 1997. Nanobeam mechanics: elasticity, strength, and toughness of nanorods and nanotubes, *Science*, **277**, 1971-1975.
- [24] **Krishnan, A., Dujardin, E., Ebbesen, T.W., Yianilos, P.N., Treacy, M.M.J.**, 1998. Young's modulus of single-walled nanotubes, *Phys. Rev. B*, **58**, 14013-14019.
- [25] **Lourie, O., Wagner, H.D.**, 1998. Evaluation of Young's modulus of carbon nanotubes by micro-Raman spectroscopy, *Journal of Material Research*, **13**, 2418-2422.
- [26] **Salvetat, J.P., Briggs, G.A.D., Bonard, J.-M., Bacsá, R.R., Kulik, A.J., Stöckli, T., Burnham, N.A., Forró, L.**, 1999. Elastic and shear moduli of single-walled carbon nanotube ropes, *Phys. Rev. Lett.*, **82**, 944-947.
- [27] **Tomblé, T.W., Zhou, C., Alexseyev, L., Kong, J., Dai, H., Liu, L., Jayanthi, C.S., Tang, M., Wu, S.-Y.**, 2000. Reversible electromechanical characteristics of carbon nanotubes under local-probe manipulation, *Nature*, **405**, 769-772.
- [28] **Yu, M.F., Files, B.S., Arepalli, S., Ruoff, R.S.**, 2000. Tensile loading of ropes of single wall carbon nanotubes and their mechanical properties, *Phys. Rev. Lett.*, **84**, 5552-5555.
- [29] **Yu, M.F., Lourie, O., Dyer, M.J., Moloni, K., Kelly, T.F., Ruoff, R.S.**, 2000. Strength and breaking mechanism of multiwalled carbon nanotubes under tensile load, *Science*, **287**, 637-640.

- [30] **Fish, J.**, 2009. *Multiscale methods bridging the scales in science and engineering*, Oxford University Press, Oxford.
- [31] **Qian, D, Wagner, G.J. and Liu, W.K.**, 2004. A multiscale projection method for the analysis of carbon nanotubes, *Comput Method Appl Mech Eng*, **193**,1603–1632.
- [32] **Gates, T.S., Odegard, G.M., Frankland, S.J.V. and Clancy, T.C.**, 2005. Computational materials: multi-scale modeling and simulation of nanostructured materials, *Composite Science and Technology*, **65**, 2416–2434.
- [33] **Odegard, G.M., Gates, T.S., Nicholso, L.M. and Wise, K.E.**, 2002. Equivalent-continuum modeling of nano-structured materials, *Composite Science and Technology*. **62**,1869–1880.
- [34] **Li, C. and Chou, T.W.**, 2003. A structural mechanics approach for the analysis of carbon nanotubes, *International Journal Solids Structures*, **40**, 2487–2499.
- [35] **Li, C. and Chou, T.W.**, 2004. Vibrational behaviors of multiwalled-carbon-nanotube-based nanomechanical resonators, *Applied Physics Letters*, **84**, 121.
- [36] **Li, C. and Chou, T.W.**, 2003. Single-walled carbon nanotubes as ultrahigh frequency nanomechanical resonators, *Physical Review B*, **68**, 073405.
- [37] **Tserpes, K.I. and Papanikos, P.**, 2005. Finite element modeling of single-walled carbon nanotubes, *Composites Part B*, **36**, 468–477.
- [38] **Sakhaee-Pour, A.**, 2009. Elastic properties of single-layered graphene sheet *Solid State Communications*, **149**, 91-95.
- [39] **Sakhaee-Pour, A., Ahmadian, M.T. and Naghdabadi, R.**, 2008. Vibrational analysis of single-layered graphene sheets, *Nanotechnology*, **19**, 085702.
- [40] **Hashemnia, K., Farid, M. and Vatankhah, R.**, 2009. Vibrational analysis of carbon nanotubes and single-layered graphene sheets using molecular structural mechanics approach, *Computational Materials Science*, **47**, 79-85.
- [41] **Fan, C.W., Liu, Y.Y. and Hwu, C.**, 2009. Finite element simulation for estimating the mechanical properties of multi-walled carbon nanotubes, *Applied Physics A*, **95**, 819-831.
- [42] **Cheng, H.C., Liu, Y.L., Hsu, Y.C. and Chen, W.H.**, 2009. Atomistic-continuum modeling for mechanical properties of single-walled carbon nanotubes, *International Journal of Solids and Structures*, **46**, 1695-1704.
- [43] **Lee, J.H. and Lee, B.S.**, 2012. Modal analysis of carbon nanotubes and nanocones using FEM, *Computational Materials Science*, **51**, 30-42.
- [44] **Sadeghi, M. and Naghdabadi, R.**, 2010. Nonlinear vibration analysis of single-layer graphene sheets, *Nanotechnology*, **21**, 105705.

- [45] **Wang, J., He, X., Kitipornchai, S. and Zhang, H.,** 2011. Geometrical nonlinear free vibration of multi-layered graphene sheets, *Journal of Physics D: Applied Physics*, **44**, 135401.
- [46] **Kitipornchai, S., He, X.Q. and Liew, K.M.,** 2005. Continuum model for vibration of multilayered graphene sheets, *Physical Review B*, **72**, 075443.
- [47] **He, X.Q., Kitipornchai, S. and Liew, K.M.,** 2005. Resonance analysis of multi-layered graphene sheets used as nanoscale resonators, *Nanotechnology*, **16**, 2086–91.
- [48] **Atalaya, J., Isacsson, A. and Kinaret, J.M.,** 2008. Continuum elastic modeling of graphene resonators, *Nano Letters*, **8**, 4196–4200.
- [49] **Scarpa, F., Adhikari, S. and Phani, A.S.,** 2009. Effective elastic mechanical properties of single layer graphene sheets, *Nanotechnology*, **20**, 065709.
- [50] **Scarpa, F., Ruzzene, M., Adhikari, S. and Chowdhury, R.,** 2010. Wave propagation and structural dynamics in graphene nanoribbons, *Nanoscale Research Letters*, **6**, 430.
- [51] **Chowdhury, R., Adhikari, S., Scarpa, F. and Friswell, M.I.,** 2011. Transverse vibration of single-layer graphene sheets, *Journal of Physics D: Applied Physics*, **44**, 205401.
- [52] **Gupta, S.S. and Batra, R.C.,** 2010. Elastic properties and frequencies of free vibrations of single-layer graphene sheets, *Journal of Computational and Theoretical Nanoscience*, **7**, 1-14.
- [53] **Mianroodi, J.R., Niaki, S.A., Naghdabadi, R. and Asghari, M.,** 2011. Nonlinear membrane model for large amplitude vibration of single layer graphene sheets, *Nanotechnology*, **22**, 305703.
- [54] **Ansari, R., Sahmani, S. and Arash, B.,** 2010. Nonlocal plate model for free vibrations of single-layered graphene sheets, *Physics Letters A*, **375**(1), 53–62.
- [55] **Arash, B. and Wang, Q.,** 2011. Vibration of single- and double- layered graphene sheets, *Journal of Nanotechnology in Engineering and Medicine*, **2**, 011012.
- [56] **Chandra, Y., Chowdhury, R., Scarpa, F. and Adhikaricor, S.,** 2011. Vibration characteristics of bilayer graphene sheets, *Thin Solid Films*, **519**, 6026-6032
- [57] **Avila, A.F., Eduardo, A.C. and Neto, A.S.,** 2011. Vibrational analysis of graphene based nanostructures, *Computer and Structures*, **89**, 878-892.
- [58] **Gibson, R.F., Ayorinde, E.O. and Wen, Y.F.,** 2007. Vibrations of carbon nanotubes and their composites: A review, *Composites Science and Technology*, **67**, 1–28.
- [59] **Li, C. and Chou, T.W.,** 2004. Modeling of elastic buckling of carbon nanotubes by molecular structural mechanics approach, *Mechanics of Materials*, **36**, 1047-1055.

- [60] **Sakhaee-Pour, A.**, 2009. Elastic buckling of single-layered graphene sheet *Computational Material Science*, **45**, 266-270.
- [61] **Mir, M., Hosseini, A. and Majzoobi, G.H.**, 2008. A numerical study of vibrational properties of single-walled carbon nanotubes, *Computational Materials Science*, **43**, 540-548.
- [62] **Tsai, P.C. and Fang, T.H.**, 2007. A molecular dynamics study of the nucleation, thermal stability and nanomechanics of carbon nanocones, *Nanotechnology*, **18**, 105702.
- [63] **Liew, K.M., Wei, J.X. and He, X.Q.**, 2007. Carbon nanocones under compression: Buckling and post-buckling behaviors, *Physical Review B*, **75**, 195435.
- [64] **Liao, M.L., Cheng, C.H. and Lin, Y.P.**, 2011. Tensile and compressive behaviors of open-tip carbon nanocones under axial strains, *Journal of Materials Research*, **26**, 1577-1584.
- [65] **Abadi, R.D.F., Fotouhi, M.M. and Haddadpour, H.**, 2011. Free vibration analysis of nanocones using nanlocal continuum model, *Physics Letters A*, **375**, 3593-3598.
- [66] **Ebbesen, T.W., Takada, T.**, 1995. Topological and SP3 defect structures in nanotubes, *Carbon*, **33**, 973-978.
- [67] **Banhart, F., Kotakoski, J. and Krasheninnikov, A.V.**, 2010. Structural Defects in Graphene, *ACS Nano*, **5** (1), 26-41.
- [68] **Nardelli, M.B., Yakobson, B.I. and Bernholc, J.**, 1998. Mechanism of strain release in carbon nanotubes, *Physical Review B*, **57**, R4277-R4280.
- [69] **Zhao, Q., Nardelli, M.B. and Bernholc, J.**, 2002. Ultimate strength of carbon nanotubes: a theoretical study, *Physical Review B*, **65**, 144105.
- [70] **Nardelli, M.B., Yakobson, B.I. and Bernholc, J.**, 1998. Brittle and Ductile Behavior in Carbon Nanotubes *Physical Review Letters*, **81**, 4656-4659.
- [71] **Sammalkorpi, M., Krasheninnikov, A., Kuronen, A., Nordlund, K., Kaski, K.**, 2004. Mechanical properties of carbon nanotubes with vacancies and related defects, *Physical Review B*, **70**, 245416.
- [72] **Belytschko, T., Xiao, S.P., Schatz, G.C., and Ruoff, R.S.**, 2002. Atomistic simulations of nanotube fracture, *Physical Review B*, **65**, 235430.
- [73] **Ansari, A., Motevalli, B., Montazeri, A., and Ajori, S.**, 2011. Fracture analysis of monolayer graphene sheets with double vacancy defects via MD simulation, *Solid State Communications*, **151**, 1141-1145.
- [74] **Lu, Q. and Bhattacharya, B.**, 2005. Fracture resistance of zigzag single walled carbon nanotubes, *Nanotechnology*, **16**, 555–66.
- [75] **Lu, Q. and Bhattacharya, B.**, 2005. The role of atomistic simulations in probing the small scale aspects of fracture – a case study on a single-walled carbon nanotube, *Eng. Fract. Mech.*, **72**, 2037–2071.

- [76] **Zhang, S., Mielke, S.L., Khare, R., et al.,** 2005. Mechanics of defects in carbon nanotubes: Atomistic and multiscale simulations, *Physical Review B*, **71**, 115403.
- [77] **Khare, R., Mielke, S.L., Paci, J.T., et al.,** 2007. Coupled quantum mechanical/molecular mechanical modeling of the fracture of defective carbon nanotubes and graphene sheets, *Physical Review B*, **75**, 075412.
- [78] **Mielke, S.L., Troya, D., Zhang, S., Li, J-L., Xiao, S., Car, R., et al.,** 2004. The role of vacancy defects and holes in the fracture of carbon nanotubes, *Chem. Phys. Lett.*, **390**, 413-420.
- [79] **Troya, D., Mielke, S.L. and Schatz, G.C.,** 2003. Carbon nanotube fracture – differences between quantum mechanical mechanisms and those of empirical potentials, *Chem. Phys. Lett.*, **382**, 133-141.
- [80] **Xu, Z.,** 2009. Graphene Nano-ribbons under tension, *Journal of Computational and Theoretical Nanoscience*, **6**, 1-3.
- [81] **Liu, F., Ming, P. and Li, J.,** 2007. Ab initio calculation of ideal strength and phonon instability of graphene under tension, *Physical Review B*, **76**, 064120.
- [82] **Zhao, H., Min, K., Aluru, N.R.,** 2009. Size and Chirality Dependent Elastic-Properties of Graphene Nanoribbons under Uniaxial Tension, *Nano Lett.*, **9**, 3012–3015.
- [83] **Wang, M.C., Yan, C., Ma, L., Hu, N. and Chen, M.W.,** 2012. Effect of defects on fracture strength of graphene sheets, *Computational Materials Science*, **54**, 236-239.
- [84] **Yanovsky, Y.G., Nikitina, E.A., Karnet, Y.N., Nikitin, S.M.,** 2009. Quantum mechanics study of the mechanism of deformation and fracture of graphene, *Physical Mesomechanics*, **12**, 254–262.
- [85] **Tserpes, K.I., Papanikos, P. and Tsirkas, S.A.,** 2006. A progressive fracture model for carbon nanotubes, *Composite Part B*, **373**, 662-669.
- [86] **Tserpes, K.I. and Papanikos, P.,** 2007. The effect of Stone-Wales defect on the tensile behavior and fracture of single-walled carbon nanotubes, *Composite Structures*, **79**, 581-589.
- [87] **Mohammadpour, E. and Awang, M.,** 2011. Predicting the nonlinear tensile behavior of carbon nanotubes using finite element simulation, *Applied Physics A*, **104**, 609-614.
- [88] **Wernik, J.M. and Meguid, S.A.,** 2010. Atomistic-based continuum modeling of the nonlinear behaviour of carbon nanotubes, *Acta Mechanica*, **212**, 167-179.
- [89] **Xiao, J.R., Staniszewski, J. and Gillespie, J.W.,** 2009. Fracture and progressive failure of defective graphene sheets and carbon nanotubes. *Composite Structures*, **88**, 602-609.
- [90] **Xiao, J.R., Gama, B.A. and Gillespie, J.W.,** 2005. An analytical molecular structural mechanics model for the mechanical properties of carbon nanotubes, *Int. J. Solids Struct.*, **42**, 3075–92.

- [91] **Xiao, J.R., Staniszewski, J. and Gillespie, J.W.**, 2010. Tensile behaviors of graphene sheets and carbon nanotubes with multiple Stone-Wales defects, *Materials Science and Engineering A*, **527**, 715-723.
- [92] **Rossi, M. and Meo, M.**, 2009. On the estimation of mechanical properties of single-walled carbon nanotubes by using a molecular-mechanics based FE approach, *Composite Science and Technology*, **69**, 1394-1398.
- [93] **Meo, M. and Rossi, M.**, 2006. Tensile failure prediction of single wall carbon nanotube, *Eng. Fract. Mech.*, **73**, 2589–2599.
- [94] **Meo, M. and Rossi, M.**, 2007. A molecular-mechanics based finite element model for strength prediction of single wall carbon nanotubes, *Materials Science and Engineering A*, **454-455**, 170-177.
- [95] **Georgantzinos, S.K., Katsareas, D.E. and Anifantis, N.K.**, 2011. Graphene characterization: A fully non-linear spring-based finite element prediction, *Physica E*, **43**, 1833-1839.
- [96] **Sun, X. and Zhao, W.**, 2005. Prediction of stiffness and strength of single-walled carbon nanotubes by molecular-mechanics based finite element approach, *Materials Science and Engineering A*, **390**, 366–71.
- [97] **Masud, A., and Kannan, R.**, 2009. A multiscale framework for computational nanomechanics: Application to the modeling of carbon nanotubes, *International Journal for Numerical Methods in Engineering*, **78**, 863-882.
- [98] **Khare, R., Mielke, L.S., Schatz, C.G. and Belytschko T.**, 2008. Multiscale coupling schemes spanning the quantum mechanical, atomistic forcefield, and continuum regimes, *Computer Methods In Applied Mechanics And Engineering*, **197**, 3190-3202.
- [99] **Zeng, X., Wang, X., Lee, J.D., and Lei, Y.**, 2011. Multiscale modeling of nano/micro systems by a multiscale continuum field theory, *Comput. Mech.*, **47**, 205-216
- [100] **Park, H.S., Karpov, E.G. and Liu, W.K.**, 2005. Non-reflecting boundary conditions for atomistic, continuum and coupled atomistic/continuum simulations, *International Journal for Numerical Methods in Engineering*, **64(2)**, 237–259
- [101] **Wagner, G.J. and Liu, W.K.**, 2003, Coupling of atomistic and continuum simulations using a bridging scale decomposition, *Journal of Computational Physics*, **190(1)**, 249–274.
- [102] **Dhia, H.B., Rateau, G.**, 2005. The Arlequin method as a flexible engineering desing tool, *International Journal for Numerical Methods in Engineering*, **62**, 1442–1462.
- [103] **Dhia, H.B.**, 2006. Global local approaches: the Arlequin framework, *European Journal of Computational Mechanics*, **15(1–3)**, 67–80.
- [104] **Xiao, S.P. and Belytschko, T.**, 2004. A bridging domain method for coupling continua with molecular dynamics, *Computer Methods in Applied Mechanics and Engineering*, **193**, 1645–1669.

- [105] **Belytschko, T. and Xiao, S.P.**, 2003, Coupling methods for continuum model with molecular model, *International Journal for Multiscale Computational Engineering*, **1**(1), 115–126.
- [106] **Zhang, S., Khare, R., Lu, Q. and Belytschko T.**, 2007. A bridging domain and strain computation method for coupled atomistic-continuum modeling of solid, *International Journal for Numerical Methods in Engineering*, **70**, 913-933.
- [107] **Guidault, P.-A., and Belytschko T.**, 2007. On the L2 and the H1 couplings for an overlapping domain decomposition method using Lagrange multipliers, *International Journal for Numerical Methods in Engineering*, **70**, 322–350.
- [108] **Rudd, R.E. and Broughton, J.Q.**, 2000. Concurrent coupling of length scales in solid state systems, *Physica Status Solidi B*, **217**, 251–291.
- [109] **Abraham, F.F., Broughton, J.Q., Bernstein, N. and Kaxiras, E.**, 1998. Spanning the length scales in dynamic simulation, *Computational Physics*, **12**(6), 538–546.
- [110] **Broughton, J.Q., Abraham, F.F., Bernstein, N., Kaxiras, E.**, 1999. Concurrent coupling of length scales: methodology and application, *Physical Review B*, **60**(4), 2391–2403.
- [111] **Chen, W., Fish, J.**, 2006. A generalized space-time mathematical homogenization theory for bridging atomistic and continuum scales, *International Journal for Numerical Methods in Engineering*, **67**(2), 253-271.
- [112] **Liu, W.K., Karpov, E.G., Zhang, S. and Park, H.S.**, 2004. An introduction to computational nanomechanics and materials, *Computer Methods in Applied Mechanics and Engineering* **193**(17–20), 1529–1732
- [113] **Curtin, W.A., Miller and R.E.**, 2003. Atomistic/continuum coupling in computational materials science, *Modelling and Simulation in Materials Science and Engineering*, **11**(3), R33–R68.
- [114] **Xu, M., Gracie, R., and Belytschko T.**, Multiscale modeling with extended bridging domain method, Chapter in *Bridging the Scales in Science and Engineering*, Oxford: Oxford Press. 1-32.
- [115] **Url-1** <<http://www.sciencedaily.com/releases/2010/10/101005085507.htm>>, date retrieved 29.06.2011
- [116] **Lijima, S.**, 2002. Carbon nanotubes: past, present, and future, *Physica B: Condensed Matters*, **323**, 1-5.
- [117] **Jannik C. Meyer, A.K. Geim, M.I. Katsnelson, K.S. Novoselov, T.J. Booth and S. Roth**, 2007. The structure of suspended graphene sheets, *Nature*, **446**, 60-63.
- [118] **Naess, S.N., Elgsaeter, A., Helgesen, G. and Knudsen, K.D.**, 2009. Carbon nocones: wall structure and morphology, *Science and Technology of advanced materials*, **10**, 065002.

- [119] **Kalamkarov, A.L., Georgiades, A.V., Rokkam, S.K., Veedu, V.P., Ghasemi Nejhad M.N.**, 2006. Analytical and numerical techniques to predict carbon nanotubes properties, *International Journal of Solids and Structures*, **43**, 6832–6854.
- [120] **Hierold, C.**, 2008. *Carbon nanotube devices; Properties, modeling, integration and applications*, Advanced Micro & Nanosystems, Volume 8, Weinheim: Wiley.
- [121] **Brinkmann, G. and Cleemput, N.V.**, 2011. Classification and generation of nanocones, *Discrete Applied Mathematics*, **159**, 1528-1539.
- [122] **Ekşioğlu, B. and Nadarajah, A.**, 2006. Structural analysis of conical carbon nanofibers, *Carbon*, **44**, 360-373.
- [123] **Harris, P.J.K.**, 1999. *Carbon nanotubes and related structures*, Cambridge: Cambridge University Press.
- [124] **Bhatti, M.A.**, 2005. *Fundamental finite element analysis and applications with Mathematica® and Matlab® computations*, New Jersey: John Wiley & Sons, Inc,
- [125] **Battezzatti L, Pisani C, Ricca F.**, 1975. Equilibrium conformation and surface motion of hydrocarbon molecules physisorbed on graphite. *J Chem Soc*, **71**, 1629–39.
- [126] **Tersoff, J.**, 1988. New empirical-approach for the structure and energy of covalent systems, *Phys. Rev. B*, **37 (12)**, 6991–7000.
- [127] **Brenner, D.W.**, 1990. Empirical potential for hydrocarbons for use in simulating the chemical vapor-deposition of diamond films, *Phys.Rev. B* **42 (15)**, 9458–9471.
- [128] **Baykasoglu, C. and Mugan, A.** 2012. Dynamic analysis of single-layer graphene sheets, *Computational Material Science*, **55**, 228-236.
- [129] **Baykasoglu, C. and Mugan, A.** 2012. Nonlinear fracture analysis of single-layer graphene sheets, *Engineering Fracture Mechanics* (in press).
- [130] **Hughes, T.J.R.**, 2000. *The finite element method, linear static and dynamic finite element analysis*, New Jersey: Prentice-Hall.
- [131] **Stone, A.J. and Wales, D.J.**, 1986. Theoretical studies of icosahedral C₆₀ and some related species, *Chem. Phys. Lett.*, **128(5–6)**, 501–3.
- [132] **Scarpa, F., Adhikari, S. and Wang, C.Y.**, 2009. Mechanical properties of non-reconstructed defective single-wall carbon nanotubes, *Journal of Physics D: Applied Physics*, **42**, 142002.
- [133] **Krashenninnikov, A.V., Nordlund, K., Sirviö, M., Salonen, E. and Keinonen, J.**, 2001. Formation of ion-irradiation-induced atomic-scale defects on walls of carbon nanotubes, *Phys. Rev. B*, **63**, 245405.
- [134] **Yang, M., Koutsos, V. and Zaiser, V.**, 2007. Size effect in the tensile fracture of single-walled carbon nanotubes with defects, *Nanotechnology*, **18**, 155708.
- [135] **Zhang, P., Lammert, P.E. and Crespi, V.H.**, 1998. Plastic deformations of carbon nanotubes, *Physical Review B*, **81**, 5346–5349.

- [136] **Xiao, S. and Hou, W.**, 2006. Fracture of vacancy-defected carbon nanotubes and their embedded nanocomposites, *Physical Review B*, **73**, 115406.
- [137] **Baykasoglu, C. and Mugan, A.**, 2012. Coupled molecular/continuum mechanical modeling of graphene sheets, *Physica E*, **45**, 151-161.
- [138] **Liu, G.R. and Quek, S.S.**, 2003. *The finite element method*, A practical course, Oxford:Butterworth-Heinemann.
- [139] **Min, K. and Aluru, N.R.**, 2011. Mechanical properties of graphene under shear deformation, *Applied Physics Letters*, **98**, 013113.
- [140] **Tsai, J., Land Tu, J.F.**, 2010. Characterizing mechanical properties of graphite using molecular dynamics simulation, *Materials & Design*, **31**, 194-199.
- [141] **Anderson, T.L.**, 1991. *Fracture Mechanics: Fundamental and Applications* CRC Press, Boca Raton
- [142] **Griffith, A.A.**, 1920. The phenomena of rupture and flow in solids, *Philos. Trans. R. Soc. London Ser. A*, **211**, 163.
- [143] **Demczyk, B.G., et al.**, 2002. Direct mechanical measurement of the tensile strength and elastic modulus of multiwalled carbon nanotubes *Materials Science and Engineering A*, **334**, 173-178.
- [144] **Mattoni, A., Colombo, L. and Cleri, F.**, 2005. Atomistic scale origin of crack resistance in brittle fracture, *Physical Review Letters*, **95**, 115501.
- [145] **Charlier, J.C.**, 2002. Defects in Carbon Nanotubes *Accounts Of Chemical Research*, **35**, 1063-1069.
- [146] **Krasheninnikov, A.V.**, 2001. Predicted scanning tunneling microscopy images of carbon nanotubes with atomic vacancies, *Solid State Commun.*, **118**, 361–365.
- [147] **Yuan, J. and Liew, K.M.**, 2009, Effects of vacancy defect reconstruction on the elastic properties of carbon nanotubes, *Carbon*, **47**, 1526-1533.
- [148] **Plimpton, S.**, 1995. Fast parallel algorithms for short-range molecular dynamics, *J Comput. Phys.*, **117**, 1–19.
- [149] **Brenner, D.W., Shenderova, O.A., Harrison, J.A., Stuart, S.J., Ni, B. and Sinnott, S.B.**, 2002. A second-generation reactive empirical bond order (REBO) potential energy expression for hydrocarbons, *Physical Review B*, **14**, 783–802.
- [150] **Jeng, Y.R., Tsai, P.C., Fang, T.H.**, 2004. Effects of temperature and vacancy defects on tensile deformation of single-walled carbon nanotubes *Journal of Physics and Chemistry of Solids*, **65 (11)**, 1849-1856.
- [151] **Duan, W.H., Wang, Q., Liew, K.M. and He, X.Q.**, 2007. Molecular mechanics modeling of carbon nanotube fracture, *Carbon*, **45**, 1769-1776.

APPENDICES

APPENDIX A.1 : Matlab algorithm for small and large deformation problems

APPENDIX A.2 : Matlab algorithm for coupled MM/CM models

APPENDIX A.1: Matlab algorithm for small and large deformation problems

Step #1 Create atomic coordinates and bonds of carbon- based nanostructures;

Step #2 Select the interatomic potentials (see Section 3.3);

- Harmonic (Universal) potential for small deformation problems,
- Modified Morse potential for large deformation problems,
- Tersoff- Brenner potential for large deformation problems,
- Lennard Jones potential for MLGSs, MWCNTs and MWCNCs,

Step #3 Use Euler-Bernoulli beam elements to represent C-C bond (see Section 3.1);

Step #4 Use consistent or lumped element mass matrices for dynamics analyses (see Section 3.1);

Step #5 Enter Euler-Bernoulli beam elements and/or mass matrices constants (see Section 3.3);

Step #6 Create 2D and 3D element stiffness and mass matrices by using atomic coordinates and element properties (see Section 3.1);

Step #7 Create topology matrices for assembly process (see Section 3.1);

Step #8 Calculate global stiffness and/or mass matrices (see Section 3.1);

Step #9 Apply boundary and loading conditions (see Section 3.2);

Step #10 Solve the equation systems (see Sections 3.2, 4.1, 4.2, 6.2, 7.1-7.4);

- Obtain atomistic displacements,
- Obtain natural frequencies and mode shapes,
- Obtain elastic properties,

Step #11 Update atomic coordinates and return Step #2 for large deformation problems (see Sections 4.3, 7.5);

Step # 12 Solve final system for large deformation problems (see Sections 4.3, 7.5);

- Obtain atomistic displacements,
- Obtain fracture stresses and strains.

APPENDIX A.2 : Matlab algorithm for coupled MM/CM models

Step #1 Create atomic coordinates and bonds of carbon- based nanostructures;

Step #2 Select the interatomic potentials (see Section 3.3);

- Harmonic (Universal) potential for small deformation problems,
- Modified Morse potential for large deformation problems,

Step #3 Use Euler-Bernoulli beam elements to represent C-C bond (see Section 3.1);

Step #4 Enter Euler-Bernoulli beam elements constants (see Section 3.3);

Step #5 Create 2D element stiffness matrices by using atomic coordinates and element properties (see Section 3.1);

Step #6 Create topology matrices for assembly process (see Section 3.1);

Step #7 Calculate global stiffness matrix (see Section 3.1);

Step #8 The element and global stiffness matrices of plane stress CM models are obtained by using the mechanical properties of SLGSs (see Section 5.1);

Step #9 Obtain the augmented equation system (see Section 5.1);

Step #10 Apply boundary and loading conditions to the coupled MM/CM model(see Section 5.2);

Step #11 Solve the equation systems (see Section 5.2);

- Obtain atomistic displacements,
- Obtain continuum displacements,

Step #12 Update atomic coordinates and return Step #2 for large deformation problems (see Section 5.2);

Step # 13 Solve final system for large deformation problems (see Section 5.2);

- Obtain atomistic displacements,
- Obtain fracture stresses and strains.

CURRICULUM VITAE

Name Surname: Cengiz BAYKASOĞLU

Place and Date of Birth: Çaykara - 1980

E-Mail: cbaykasoglu@gmail.com, baykasoglu@itu.edu.tr

B.Sc.: Dokuz Eylul University

M.Sc.: Gazi University

List of Publications:

- **Baykasoglu, C.**, Sünbuloğlu, E., Bozdağ, E., Aruk, F., Toprak, T., Mugan, A., 2012 Crash and structural analyses of an aluminum railroad passenger car, *International Journal of Crashworthiness*, 17-5, 519-528.
- Arat S., Bilhan H., Bozdağ E., Sunbuloglu E., **Baykasoglu C.**, Kutay O., 2012 The Influence of the Attachment Type and Implant Number Supporting Mandibular Overdentures on Stress Distribution: An in vitro Study - Part I, *Implant Denstry* (in press)
- **Baykasoğlu, C.**, Sünbuloğlu, E., Bozdağ, E., Aruk F., Toprak, T., Muğan, A., 2012. Numerical static and dynamic stress analysis on railway passenger and freight car models. *International Iron & Steel Symposium*, 579-586, 2-4 April, Karabuk, Turkey.
- Bozdağ, E., Sünbuloğlu, E., **Baykasoğlu, C.**, Toprak, T., Muğan, A., 2012 Experimental static and dynamic stress analysis on railway passenger and freight car models International, *International Iron & Steel Symposium*, 470-483, 2-4 April, Karabuk. Karabuk, Turkey. (In Turkish)
- Arat, S., Bozdağ, E., Sunbuloglu, E., Bilhan, H., Kutay, O., **Baykasoglu, C.**, Mugan, A. 2011. In Vitro Assessment of Mandibular Stress Distribution around Different Implant Overdenture Attachments, *EPA 2011*, 22 September – 1 October, Bern, Switzerland.
- **Baykasoğlu, C.**, Sünbuloğlu, E., Bozdağ, E., Aruk, F., Toprak, T., Muğan, A., 2011. Railroad passenger car collision analysis and modifications for improved crashworthiness, *International Journal of Crashworthiness*, 16-3, 319-329
- Erdin, M. E., Tuç, B., **Baykasoğlu, C.**, 2010. Effect of profile modification on tooth stresses in spur gears using finite element method, *National Design, Manufacturing and Analysis Congress*, 11-12 November , 497-504, Balıkesir.

- **Baykasoğlu, C.**, Aruk F., Sünbuloğlu, E., Bozdağ, E., Toprak, T., Muğan, A., 2010. Impact analysis of railroad passenger car, *National Design, Manufacturing and Analysis Congress*, 11-12 November, 505-513, Balıkesir.
- **Baykasoğlu, C.**, Sünbuloğlu, E., Bozdağ, E., Aruk F., Toprak, T., Muğan, A., 2010. Vibration and crash analyses of an aluminum railroad passenger car, *VIII. Abaqus Users' Meeting*, 4-5 November, Istanbul, 157-164.
- Baykasoğlu, A., Yurdakul, M., **Baykasoğlu, C.**, 2006. Application of activity based cost in a SME, “*National Manufacturing Researches Symposium*”, 22-23 September, 3–11, Istanbul.

PUBLICATIONS/PRESENTATIONS ON THE THESIS

- **Baykasoglu, C.** and Mugan, A., 2012. Dynamic analysis of single-layer graphene sheets, *Computational Material Science*, 55, 228-236.
- **Baykasoğlu, C.**, Muğan, A., 2011. Fracture behavior of single-layer graphene sheet, *I. National Nanotechnology Congress*, 17-18 June, 148-155, Istanbul.
- **Baykasoglu, C.** and Mugan, A., 2012. Coupled molecular/continuum mechanical modeling of graphene sheets, *Physica E: Low-dimensional Systems and Nanostructures*, 45, 151-161.
- **Baykasoglu, C.** and Mugan, A., 2012 Nonlinear fracture analysis of single-layer graphene sheets, *Engineering Fracture Mechanics* (in press).
- **Baykasoglu C.**, Kirca M ve Mugan A 2012 Fracture analysis of reconstructed vacancy defeted carbon nanotubes, *II. National Nanotechnology Congress*, 27-28 September, 48-54. Istanbul.